KAUNAS UNIVERSITY OF TECHNOLOGY

ROKAS ŠAKALYS

A STUDY OF THE INFLUENCE OF HIGH-FREQUENCY EXCITATION ON THE QUALITY OF MICROSTRUCTURES REPLICATED BY THERMAL IMPRINT TECHNOLOGIES

Doctoral Dissertation

Technological Sciences, Mechanical Engineering (09T)

Kaunas, 2017

The dissertation was prepared at Kaunas University of Technology, Faculty of Mechanical Engineering and Design in 2012 – 2017. Research was supported by Research Council of Lithuania.

Scientific supervisor:

Prof. Dr. Habil. Arvydas PALEVIČIUS (Kaunas University of Technology, Technological Sciences, Mechanical Engineering – 09T).

Editor:

Dovilė Dumbrauskaitė (Publishing House “Technologija”)

© R. Šakalys, 2017

ISBN 978-609-02-1306-3

The bibliographical information of this issue is available at Martynas Mazvydas National Library of Lithuania National Bibliographic Database (NBD)

KAUNO TECHNOLOGIJOS UNIVERSITETAS

ROKAS ŠAKALYS

AUKŠTADAŽNIŲ VIRPESIŲ ĮTAKOS MIKROSTRUKTŪRŲ, ANTRINAMŲ TERMINIO SPAUDIMO METODAIS, KOKYBEI TYRIMAS

Daktaro disertacija
Technologiniai mokslai, mechanikos inžinerija (09T)

2017, Kaunas

Disertacija rengta 2012 – 2017 metais Kauno technologijos universiteto Mechanikos inžinerijos ir dizaino fakultete. Mokslinius tyrimus rėmė Lietuvos mokslo taryba.

Mokslinis vadovas:

Prof. habil. dr. Arvydas PALEVIČIUS (Kauno technologijos universitetas, technologiniai mokslai, mechanikos inžinerija – 09T).

Interneto svetainės, kurioje skelbiama disertacija, adresas: http://ktu.edu

Redagavo:

Dovilė Dumbrauskaitė (Leidykla „Technologija“)

© R. Šakalys, 2017

ISBN 978-609-02-1306-3

Leidinio bibliografinė informacija pateikiama Lietuvos nacionalinės Martyno Mažvydo bibliotekos Nacionalinės bibliografijos duomenų banke (NBDB)

CONTENT

INTRODUCTION 8
1. A REVIEW OF THE MOST MODERN TECHNOLOGY IN MICROSTRUCTURE DESIGN, REALIZATION AND FABRICATION 12
1.1. CGH for designing topologically complex microstructures 12
1.2. Methods for physically implementing a 3D image 13
1.2.1. The process of reactive ion etching 13
1.2.2. The process of electron beam lithography 14
1.3. Microstructure replication methods 16
1.3.1. Ultrasonic hot embossing technology 16
1.3.2. Microinjection moulding 18
1.3.3. Thermal imprint 19
1.3.4. A comparison of the processes 22
1.4. Polymer rheology in thermal imprint technologies 23
1.4.1. Viscoelastic behaviour of the polymer 23
1.4.2. Molecular orientation and relaxation 24
1.4.3. Rheological description of the polymer melt 24
1.4.4. Structural viscous behaviour of the polymer 24
1.4.5. Cooling of the molten polymer (p-V-T diagram) 25
1.4.6. Shrinkage 27
1.4.7. Polymer flow 27
1.4.8. Rheological characteristics and their dependence on vibrations 28
1.5. Quality assessment 28
1.5.1. Diffraction efficiency 28
1.5.2. Atomic Force Microscope 29
1.6. The aim and objectives of the dissertation 30
2. MATERIALS AND EQUIPMENT 32
2.1. The experimental equipment 32
2.2. Measurement equipment 33
2.3. Materials 37

2.4. The conclusions of the chapter 38
3. MICROSTRUCTURE DESIGN, REALIZATION AND REPLICATION 40
3.1. Generating a computer-generated hologram 40
3.2. The realization of a CGH by using Electron Beam Lithography 42
3.3. The investigation of a CGH 42
3.4. Results 43
3.5. The Ultrasonic Hot Embossing process 45
3.5.1. The fabrication of pre-structured foils 45
3.5.2. An analysis of the sets of appropriate process parameters 47
3.6. The development of VAPs for thermal imprint assisted by high-frequency vibrations 50
3.6.1. Finite Element model 53
3.6.2. Validation of the FE model 58
3.6.3. A study of pre-stressed devices 63
3.6.4. An investigation of lateral displacements 66
3.7. Conclusions of the chapter 67
4. EXPERIMENTS OF MICROSTRUCTURE REPLICATION 69
4.1. UHE of periodic microstructures 69
4.2. Experiments with thermal imprint 71
4.2.1. Results 72
4.3. Conclusions of the chapter 77
5. GENERAL CONCLUSIONS 78
LIST OF AUTHOR'S PUBLICATIONS 87
APPENDIXES 90

CONVENTIONS AND ABBREVIATIONS

AFM– atomic force microscope
CGH– computer- generated holography
DFT– discrete Fourier transform
DOE– diffractive optical elements
EBL– electron beam lithography
ESPI– electronic speckle pattern interferometry
FBMS– fixed beam moving stage
FE– finite element
FFT– fast Fourier transform
FT– Fourier transform
IFTA– iterative Fourier transformation algorithm
LDV– laser Doppler vibrometer
MEMS– micro electro mechanical systems
MOEMS–micro opto-electro mechanical system
ODS– operating deflection shape
P2P– plate-to-plate
PC– polycarbonate
PMMA– poly-methyl methacrylate
R2P– roll-to-plate
R2R– roll-to-roll
RDE– relative diffraction efficiency
RIE– reactive ion etching
UAT– ultrasonically-assisted tool
UHE– ultrasonic hot embossing
VAP– vibroactive pad

INTRODUCTION

The development of MEMS and MOEMS started with silicon etching and polymer processing (Finne and Klein 1967; Nathanson, Newell et al. 1967; Bartolini, Hannan et al. 1970). Nowadays, it is hard to imagine daily life without such systems; they are exploited in information processing, medicine, laser technologies, electronics, measurements, optics etc. In order to produce high-quality microsystems and improve the production process, it is necessary to enhance microstructure fabrication technologies. Sensitivity, reliability and high-definition are distinguished as the main quality requirements of advanced MEMS and MOEMS.

Classic microstructure fabrication technologies like etching, photolithography and electroplating today have become inefficient due to the long process and high expenses. Therefore, microstructure replication using thermal imprint is proposed as an alternative. However, the process presents some quality related issues, such as incompletely replicated microstructures and cracks. Previous studies have demonstrated that the application of high-frequency vibratory excitation during the process enhances the replicability of the microstructure (Narijauskaite, Palevicius et al. 2013). On the other hand, there are no established relationships between process parameters and the quality of the replicated microstructure, and there is no developed technology which ensures the uniform effect of high-frequency excitation throughout the replicated microstructure. Considering the importance and demand of precise microsystems as well as the results of previous studies, it is worth to implement further investigations regarding the improvement of high-frequency-assisted thermal imprint process, since it creates preconditions for efficient replication of high-quality microstructures.

The aim of the dissertation: to investigate the influence of high-frequency vibratory excitation on the quality of microstructures replicated with thermal imprint technologies.

The objectives:

1. To select the methods, equipment and materials enabling to design, fabricate and replicate microstructures by using high-frequency-assisted thermal imprint technologies.
2. To develop a master microstructure for the replication on polymer by using high-frequency-assisted thermal imprint technologies.
3. To develop the microstructure replication technology which operates on the basis of high-frequency vibrations and ensures high replicability and uniformity of the replicated microstructures.
4. To characterize microstructures replicated by applying imprint technologies with the assistance of high-frequency vibrations.

Research methods

Experimental and theoretic research methods are applied in the study. CGH is implemented by applying the *Matlab* software and practical EBL is implemented by using the Raith e-LiNEplus system. The PRISM System, which operates on the basis of holographic interferometry, and LDV Polytec are applied in the VAPs ODS frequency response analysis. Numerical frequency response of the VAPs is analysed with the *COMSOL Multiphysics* software. The thermal imprint device which was fabricated by the scientists from the Institute of Materials Science (KTU) and UHE equipment HiQ DIALOG 1200 made by the Herrmann Ultrasonics company are used to replicate the microstructures. The microstructures are modelled with the *GSolver* software. The quality of the replicated microstructures is evaluated by applying the AFM NANOTOP-206 and a laser diffractometer.

The research was carried out at the Institute of Materials Science, Institute of Mechatronics and the Department of Mechanical Engineering at KTU and at KEMikro institute of RWTH Aachen University, Germany.

Defended statements

1. The topologically complex master microstructure developed using the CGH technology is effectively applicable in the process of microstructure replication.
2. The technology developed for microstructure replication increases microstructure replicability under lower temperature than polymer glass transition.
3. The technology developed for microstructure replication results in increased microstructure replicability independently of changes in thermal imprint pressure.
4. The application of pre-structured foils in the process of UHE enables to minimize the process duration and imprint force parameters, and enhances the quality of the replicated microstructures.

Scientific novelty

1. The CGH technology which enables to create master microstructures in virtual reality has been developed.
2. A technology which operates on the principle of CGH enabling to fabricate master microstructures on the basis of EBL has been developed.
3. VAPs which enable to generate uniform amplitudes throughout the operating surface during the process of thermal imprint have been developed and investigated using mathematical modelling.
4. The technologic parameters for the thermal imprint process which ensure a qualitative process of microstructure replication throughout the replicated surface have been determined.
5. The influence of applying pre-structured foils on the UHE process duration, imprint force parameters and the quality of replicated microstructures has been established.

Practical significance

The practical significance of this dissertation relates to the fact that thermal imprint for the replication of precise microstructures has been improved as a method for microstructure replication by beneficially exploiting high-frequency vibrations. The enhancement offers significant benefits, since the method is cost and material-efficient, if compared to other polymer microfabrication techniques. Until now, the quality of microstructures replicated by applying this method was the most important problem; some deficiencies decreased replicability of the final product. The issues emerged due to exclusion or ineffective application of vibratory excitation.

The main focus of the dissertation was to improve the process results, i.e. the quality of fabricated microstructures, by rationally-defined exploitation of high-frequency vibrations during the process of thermal imprint. The VAPs were studied using frequency response analysis and applying numerical and experimental techniques, thus minimizing inaccuracies.

The results of the research reveal that the correct application of high-frequency vibratory excitation allows replicating microstructures with quality close to the theoretical ideal. This opens new opportunities to replicate microstructures with high precision by applying a low-cost and widely adopted fabrication method.

The UHE process is adapted for the replication of microstructures, thereby enabling to replicate microstructures and compare two different replication techniques.

Scope and the structure of the dissertation

The dissertation contains the introduction, 4 chapters, general conclusions, a list of literature including 129 references and the list of published scientific publications. The dissertation is composed of 96 pages, 78 figures and 20 tables.

The introduction presents the problem of the dissertation, as well as the aim and objectives of the work; moreover, the scientific novelty, the defended statements and practical significance of the dissertation are presented.

The first chapter presents the analysis of literature and introduces the current problems associated with microstructure replication, with regards to which the aim and objectives of the dissertation are established.

The second chapter presents the materials and equipment which are necessary to achieve the aim of the dissertation.

The third chapter explains the design of topologically complex microstructures by using the Gerchberg-Saxton algorithm with FT and fabrication by applying EBL. This chapter also describes the adaptation of UHE technology for microstructure replication through the exploitation of additional heat generation. Finally, the chapter outlines the use of thermal imprint technology with the assistance of high-frequency vibratory excitation, and presents the numerical and experimental frequency response analysis of the constructed VAPs.

Chapter four describes the microstructure replication experiments with UHE and thermal imprint with the assistance of high-frequency vibratory excitation. After performing the experiments, the quality of the microstructures has been analysed.

The final chapter provides general conclusions of the dissertation. Finally, the references and author's scientific publications are presented.

Approbation of the dissertation results

The doctoral research was performed in laboratories of:

- Institute of Material Science
- Institute of Mechatronics
- Department of Mechanical Engineering
- KEMikro Institute of RWTH Aachen University, Germany

The results of the dissertation are obtained in accordance with the project of scientific groups: "The development and research of the micromechanical periodical systems for human health diagnostic, the number of project: MIP-026/2014". The project is financially supported by the Research Council of Lithuania. Duration of the project 2014–2016.

The dissertation-related issues were presented at 4 scientific conferences:

International Conference VIBROENGINEERING 2014, October 13–15, 2014, Katowice, Poland;

The 19th international conference Mechanika-2014, April 24–25, 2014, Kaunas, Lithuania;

1st International Electronic Conference on Sensors and Applications;

International conference VIBROENGINEERING 2013, 18–20 September 2013, Druskininkai, Lithuania;

16 scientific publications related to the problems raised in the doctoral dissertation were published in scientific journals: 7 publications in ISI Web of Science database with impact factor, 3 in ISI Web of Science database and 6 publications in other international database journals.

1. A REVIEW OF THE MOST MODERN TECHNOLOGY IN MICROSTRUCTURE DESIGN, REALIZATION AND FABRICATION

This chapter introduces the methods of microstructure design, physical implementation and fabrication. The aim of this study is to reveal their advantages and disadvantages thus facilitating the selection of the most appropriate process flow.

Firstly, the chapter discusses CGH as a process to design MOEMS and analyses EBL and RIE technologies for master microstructure fabrication. Replication of microstructures requires technology which would guarantee high-precision of the replicated features, low cost and short cycle times. The most advanced replication technologies include thermal imprint, microinjection moulding (Herzig 1997; Giuseppe A. Cirino 2011; Jahns 1999) and UHE.

1.1. CGH for designing topologically complex microstructures

The fields of CGH application include:

- DOEs for storage of digital data and images (Wilson, Curtis et al. 2000),
- Interferometric measurements (Gren 2003),
- Recognition of patterns (Saari, Kaarli et al. 1993),
- Data encryption (Nishchal, Joseph et al. 2004) and
- 3D displays (Son, Javidi et al. 2006).

CGH is defined mathematically by computing the phase and amplitude data of the wave propagation generated by an object. Namely, it is the method of mathematically designing a hologram. The main difference between CGH and conventional optical holography is that in order to record CGH there is no need to have an existing physical object, i.e. it can be generated numerically (Jahns 1999; Giuseppe A. Cirino 2011).

DOEs which are designed by applying CGH technology are divided into phase-only, amplitude-only and complex. Phase-only DOE changes the phase of incoming light, whereas the amplitude remains the same. In contrast, amplitude-only DOEs media modifies the amplitude, while the phase remains invariable. Complex DOE modifies both the amplitude and the phase (Giuseppe A. Cirino 2011).

In its simplest form, the generation of a CGH is the calculation of complex transmittance. Phase variation required to reconstruct the needed image is obtained by altering the topology of the CGH. FT is the method applied for generating a two-dimensional CGH.

The calculation of CGH relates the calculation of interference fringes with the shape of the object. FFT is used to calculate the CGH of a planar object rapidly. Methods such as Fresnel integral, point filling etc. are exploited in calculations of CGH of planar objects. The Fresnel integral method is time-consuming and does not allow performing real time CGH calculations (Oikawa, Shimobaba et al. 2011).

The design of a CGH is divided into two steps: input/output and iterations. Iterations are based on the Gerchberg-Saxton algorithm (Fig. 1.1.) (Gerchberg 1972)

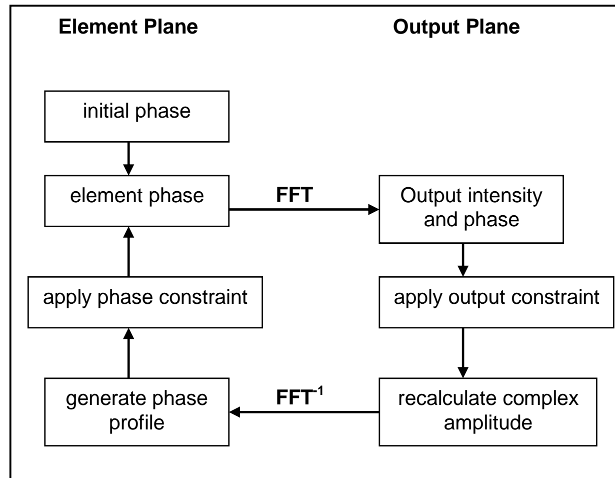

Fig. 1.1. An illustration of the Gerchberg-Saxton algorithm

This method applies two constraints: output and phase. The output constraint allows to achieve the required intensity by maintaining the same phase. The application of phase constraint alters the phase, while the amplitude is kept constant during the iterations; the phase is altered until the designed requirements are attained.

The disadvantage of the Gerchberg-Saxton algorithm is that it is determined by the initial phase estimate and stagnates as a result of the direct quantization of the phase profile (Thomson and Taghizadeh 2005).

1.2. Methods for physically implementing a 3D image

Well-defined, i.e. precise master microstructures are necessary in order to replicate the designed microstructures. Microstructures with features of several micrometres may not be fabricated by traditional machining technologies, such as milling etc., thus it is necessary to apply microfabrication technologies. RIE and EBL are discussed and compared methods for fabricating high aspect ratio master microstructure.

1.2.1. The process of reactive ion etching

RIE (Fig. 1.2.) is an anisotropic dry etching process. Anisotropy is a critical aspect when high precision is required. The technologies of isotropic wet chemical etching are not applicable in fabricating precise microstructures, since etching under the mask can occur (Fischer and Chou 1993).

The RIE technology applies chemically reactive plasma (generated by an electromagnetic field) which by deposition removes the material layer from the surface.

The RIE system contains the following elements: a cylindrical vacuum chamber and material which is electrically isolated from the environment. The processed material is on the bottom of the chamber. The type and amount of gas depend on the process and processed material (Wolf 1995).

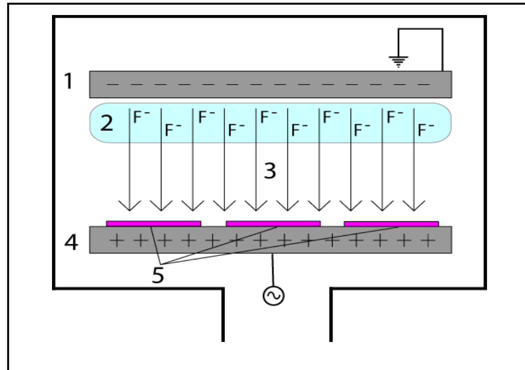

Fig. 1.2. The scheme of RIE setup: electrodes (1 and 4), ions (2), electric field (3) and mask (5) (Lagoski, Coutu et al. 2009)

Plasma is generated by applying electromagnetic field to the processed material and the electromagnetic field ionizes gas which are supplied to the chamber. A positive charge is generated on the processed surface, whereas the plasma is negatively charged. The pattern to be etched is covered with a mask; it secures the surface, exposing only the areas to be etched with the ion beam. Because of the difference between charges, negative ions sputter the surface of the positively ionized material which is not covered with mask, they react with the surface ions and chemical surface etching takes place. The rate of etching directly depends on the pressure of gas; lower pressure results in higher etching precision (Kvedaravičius 1989).

The main advantages of this technology are high-precision of the patterns and well-controlled process (Fischer and Chou 1993; Schwartz and Schaible 1979). The main disadvantage of the process is long preparation for etching which takes approximately 13–14 hours, since such time consuming processes as wafer preparation, spin coating, EBL, developing, mask deposition and lift off are necessary in order to develop the mask (Chou and Fischer 1990).

1.2.2. The process of electron beam lithography

EBL technology (Fig. 1.3.) allows fabricating microstructures with features of sub-10 nm dimensions. This method exploits an electron beam to change the solubility of the resist which covers the substrate, thereby facilitating the removal of resist during the following development stage (Mohammad, Muhammad et al. 2012).

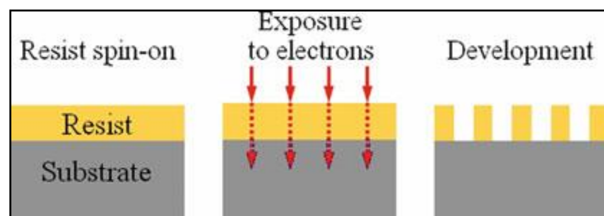

Fig. 1.3. A scheme of EBL process (Mohammad, Muhammad et al. 2012)

The preparation for EBL process requires spin coating the substrate with micro resist. Then, the EBL process starts. As the beam of electrons arrives and enters the resist, a sequence of energy collisions which alter the direction of the electrons initiate; this increases the size of the beam, as it moves deeper into the resist, i.e. towards the substrate. This forward scattering (Fig. 1.4.) is more obvious at lower electron energies (Mohammad, Muhammad et al. 2012; Lee, Browning et al. 1992; Yang, Fan et al. 2006).

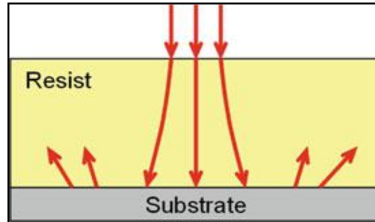

Fig. 1.4. Forward and back scattering during the process of EBL (Mohammad, Muhammad et al. 2012)

Backscattering is an additional considerable aspect which influences the electron transport during EBL process (Kyser and Viswanathan 1975). A large amount of electrons arrives at the substrate and enters it. Some of these electrons experience sufficient amount of collisions to leave the substrate and enter the resist for the second time at a different location than it entered the substrate. If the energy is sufficient for backscattering, the final structure may be larger when compared to the initially designed one (Kamp, Emmerling et al. 1999; Mohammad, Muhammad et al. 2012; Brewer 1980; Ballantyne 1980). The phenomenon when the fabricated microstructure is larger than the designed one is called proximity effect (Chang 1975; Lo, Rooks et al. 1995; L.K. Mun 2004).

Metal deposition (Fig. 1.5.) is necessary to replicate the microstructure by applying replication methods. After the metal deposition resist is separated from the wafer, the metalized master microstructure is obtained.

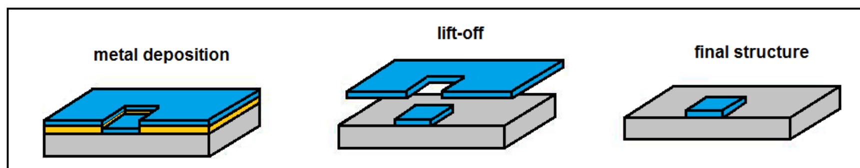

Fig. 1.5. Metallisation of the master microstructure

The advantages of EBL include high-resolution and the possibility to fabricate the master microstructure without applying the mask. The main disadvantage of the technology is long duration, especially when complex images are fabricated. However, the process can be hastened by exploiting several parallel beams (Mohammad, Muhammad et al. 2012).

The master fabrication technology is selected after estimating the main advantages and disadvantages of both analysed methods. EBL is chosen after considering the following aspects: capacity to accelerate the process by applying several electron beams and no necessity to fabricate the mask.

1.3. Microstructure replication methods

The following stage in the process flow is the replication of microstructures. Conventional MEMS technologies such as photolithography or etching are applicable for high aspect ratio microstructures with dimensions of several square millimetres. Most of the modern microstructures are of several square centimetres and larger. Thus, it is important to consider and apply novel replication methods, such as injection moulding, thermal imprint and UHE (Velten, Schuck et al. 2009).

1.3.1. Ultrasonic hot embossing technology

UHE (Fig. 1.6.) is a widely adopted process, during which the master microstructure is embossed into a polymer film by applying UAT (sonotrode). This replication method is low-cost, easy to automate and relatively rapid (P. Khuntontong 2008); the process duration is in the range of several seconds. The difference between UHE and thermal imprint is that heating in UHE is generated by ultrasound (Sackmann, Burlage et al. 2015).

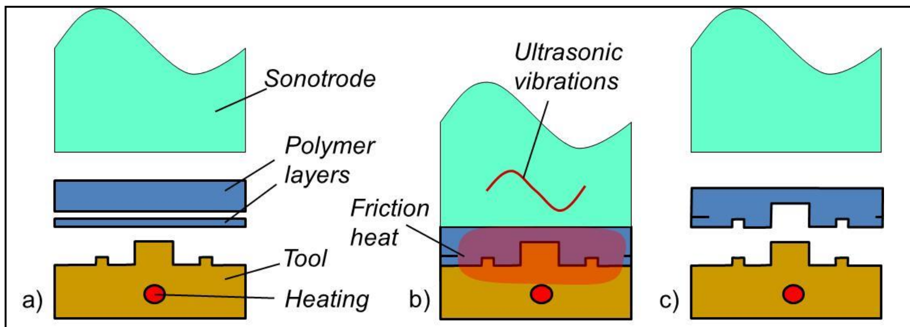

Fig. 1.6. UHE process: UAT moves towards the polymer (a), ultrasonic excitation is applied (b) and UAT is retracted (c) (Kosloh, Sackmann et al. 2016)

Initially, the polymer foil (or several foils) is placed on the protruding tool, the UAT of the UHE machine is driven down and initiates to press the polymer. Ultrasonic vibratory excitation of constant amplitude (Nonhof and Luiten 1996) is applied after the trigger pressure force is achieved. This excitation generates the friction heat at the contact of the tool and polymer (Liao, Gerhardy et al. 2014), i.e. ultrasonic vibratory excitation is converted to thermal energy (P. Khuntontong 2008). The heat melts the polymer and it adapts to the shape of the tool (Linfa, Yujun et al. 2014; Liu and Dung 2005). Subsequently, the ultrasound is turned off and solidification force is applied in order to harden the molten polymer. The final step is removing the replicated microstructure from the tool (Fig. 1.7.).

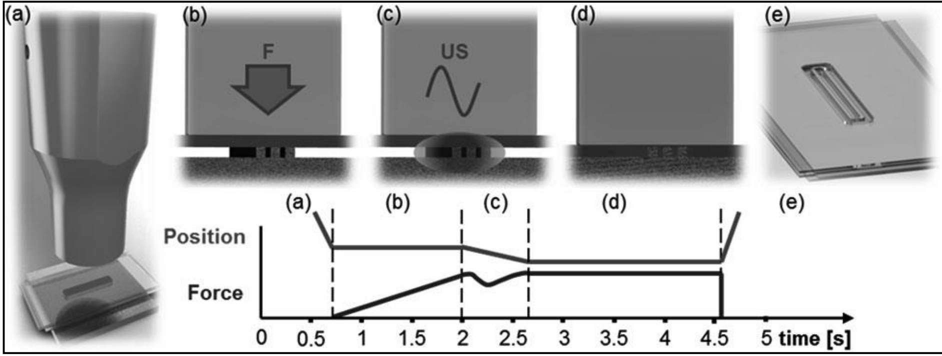

Fig. 1.7. UAT travel and imprinting force dependence throughout the process of UHE: UAT moves towards the work-piece (a), UAT touches the surface of the polymer, the force increases until the trigger force is attained (b), the trigger force is attained, ultrasound is applied (c), solidification (d) and UAT retraction (e) (Tollkötter, Sackmann et al. 2015)

Thermal energy is generated as a result of cyclic polymer deformations which are stimulated by UAT. The phase of the deformations does not coincide with vibrations of the UAT, i.e. energy dissipates and heat is produced.

A particular portion of ultrasonic energy is transferred to the polymer. However, the other part of the energy is reflected at the interface between the UAT and the polymer. The reflected energy is calculated by the reflection coefficient R_{ij} which specifies the amplitude of sound reflected from the interface of two materials:

$$R_{i,j} = \frac{Z_i - Z_j}{Z_i + Z_j} \quad , \tag{1}$$

$$Z = \rho c \, , \tag{2}$$

here: Z – acoustic impedance, c – sound velocity in material and ρ – density of material.

The difference between impedance of UAT and polymer should be minimum in order to obtain a larger transfer of energy but as the ultrasound arrives at the tool (which is placed under the polymer), higher reflection is necessary. This requires a larger difference in acoustic impedances. In case of several polymer foils, the greatest part of energy is transferred. However, the application of pre-structured foils allows obtaining energy reflection due to accumulated air between the layers. An increase in temperature leads to an increase of impedance and ultrasound absorption (Sinha and Buckley 2007; Kosloh, Sackmann et al. 2016).

The process frequency usually varies from 10 to 75 kHz. Lower frequency transfers higher force to the polymer and higher frequency minimizes the polymer damage and produces less noise (Khuntontong 2008).

Polymer foils with thickness ranging from 50 to 2000 μm are applied in the process. If the polymer plate is excessively thick, the ultrasonic energy is absorbed by

the material, therefore the surface which comes in contact with the protruding tool is not pre-heated. In case of embossing several polymer foils, the friction heat is generated between the polymer foils and its distribution between foils depends on the thickness of individual foils.

The depth of embossing depends on the force of the UHE machine. Typically, the maximum depth does not exceed several millimetres. However, the protruding features should be of adequate height in order to generate sufficient friction heat for melting the polymer.

Ultrasonic vibrations are applied for 150–500 ms, depending on the process conditions. The duration of applying ultrasound depends on the dimensions of the microstructure, specific thermal energy which is required to melt the polymer as well as heat conductivity of the material.

The duration of solidification depends on such parameters as heat capacity, heat conductivity of the polymer and the geometry of the tool. Typically, the duration ranges from 500 ms (for a stack of several foils) to several seconds (for foils, thicker than 1 mm) (Liao, Gerhardy et al. 2014; Yu, Lee et al. 2009; P. Khuntontong 2008).

1.3.2. Microinjection moulding

Microinjection moulding (Fig. 1.8.) is a variothermal replication technology for fabricating microstructures with medium to large outputs (Michaeli, Spennemann et al. 2002; Heckele and Schomburg 2004). The process begins by melting the polymer in a plasticization unit and the molten polymer is injected into a clamped micro-structured mould insert. Eventually, the molten polymer is cooled and the finished part is demoulded (Julien, Thierry et al. 2007).

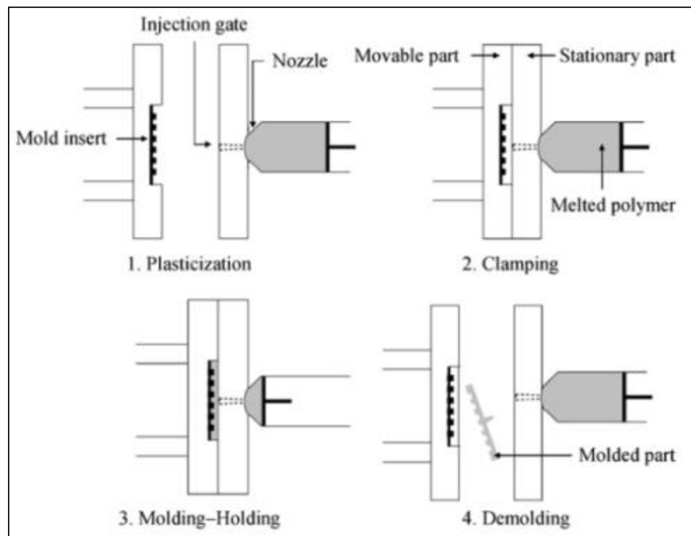

Fig. 1.8. A schematic drawing of the microinjection moulding process (Julien, Thierry et al. 2007)

The most significant process parameters are:

- The temperature of the mould
- The rate of injection
- The pressure of injection
- The duration of holding
- The pressure of holding (Zhao, Mayes et al. 2003; Zhao, Mayes et al. 2003; Whiteside, Martyn et al. 2005)

Microinjection moulding is a modification of the injection moulding technology. The application of injection moulding devices leads to large material consumption, as the mass of the microstructure corresponds to several percent of the plasticized mass. In addition, conventional machines are not precise enough for replicating micro parts, consequently servo-electric machines are required for microstructure applications (Kelly, Woodhead et al. 2005). As a solution for more precision, molten thermoplastic is injected by using a special injection cylinder which allows more precise dosage (Friedrich and Walter 2004).

The technology allows replicating parts with micro-features of 0,2 μm, thickness of 20 μm and mass of several milligrams (Memering 2014; Christian and Walter 2015). However, the risk of microstructure damage emerges when replicating thin parts with a relatively large surface area. The injection volume must be greater than 1 cm^3 per injection in order to minimize the likelihood of defects (Memering 2014).

The process duration is several minutes per one part (Ruprecht, Gietzelt et al. 2002; Whiteside, Martyn et al. 2003; Oberbach 2004; Julien, Thierry et al. 2007).

1.3.3. Thermal imprint

Thermal imprint (Fig. 1.9.) is a straightforward, low-cost (Juang, Lee et al. 2002; Eusner, Hale et al. 2010), well-developed, efficient and prospective method for replicating precise high aspect ratio microstructures (Heckele, Bacher et al. 1998; Yao 2011; Koç and Mahabunphachai 2011; Özel and Thepsonthi 2011). The process is divided into four stages:

1. Heating
2. Imprinting
3. Cooling
4. Demoulding (Worgull, Hétu et al. 2008; Kolew, Münch et al. 2010)

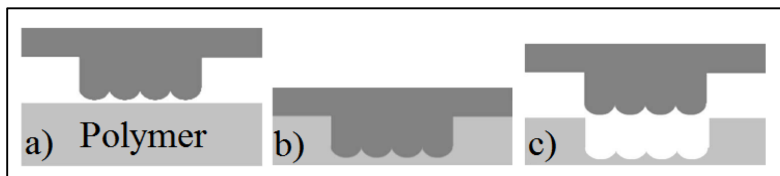

Fig. 1.9. Thermal imprint: heating of the master microstructure and polymer substrate (a), embossing (b), and demoulding (c) (Park, Kim et al. 2008)

The process initiates at ambient temperature. The master microstructure is pre-heated to the polymer melting temperature and imprinted into the polymer. The imprinting pressure is applied for a period of time which is necessary to form the microstructure on the polymer. Finally, the master microstructure and the polymer are cooled down and demoulded (Julien, Thierry et al. 2007; Eusner, Hale et al. 2010). The temporal scheme of the process is presented in Fig. 1. 10.

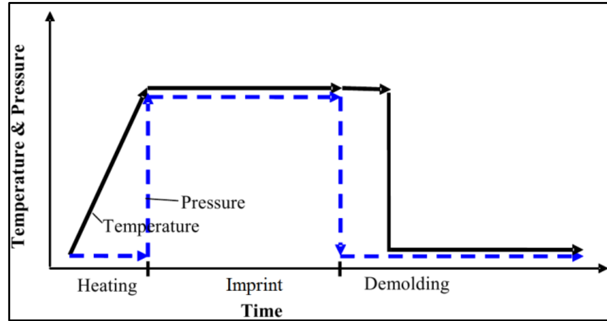

Fig. 1.10. The temporal diagram of thermal imprint

The depth of the replica is proportional to the temperature, imprint duration and pressure (Lee, Kang et al. 2010; Singh and Dupaix 2012; Lin, Yeh et al. 2013; Velten, Schuck et al. 2009; Linfa, Yujun et al. 2014).

The production outputs range from a single copy to several thousand of fabricated parts (Kolew, Münch et al. 2010; Heckele, Bacher et al. 1998). Microstructures can be replicated by employing different configurations of polymer and master microstructure, such as: R2R; P2P and R2P (Fig. 1.11.) (Farshchian, Park et al. 2012; Liedert, Amundsen et al. 2012; Vig, Mäkelä et al. 2011; Metwally, Robert et al. 2011).

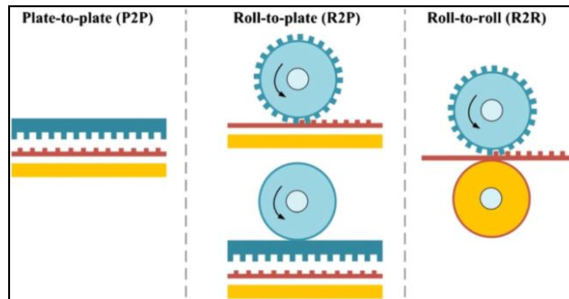

Fig. 1.11. Possible variations of the thermal imprint process (Linfa, Yujun et al. 2014)

The main disadvantage is the potential damage of the replicated microstructure. During the process of heating and embossing, the polymer is subjected to a combination of stress and strain. The stress is relaxed and deformations are recovered during the stages of cooling and demoulding (Liu, Li et al. 2010). The contact interaction throughout the process of thermal imprint is provided in Fig. 1.12.

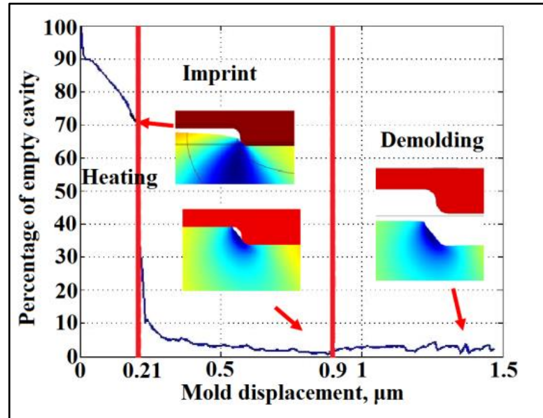

Fig. 1.12. The contact interaction between the master microstructure and polymer throughout the process of thermal imprint

During demoulding, the polymer and master microstructure shrink at dissimilar rates because they are produced from different materials. This causes high contact stress between the polymer and vertical walls of the master microstructure (Fig. 1.13.). Demoulding requires highly precise alignment, accurate control of temperature and force to avoid microstructure defects (Kolew, Heilig et al. 2011). Low filling ratio and relatively long cycle time present additional challenges (Yao, Nagarajan et al. 2006; Mehne 2008).

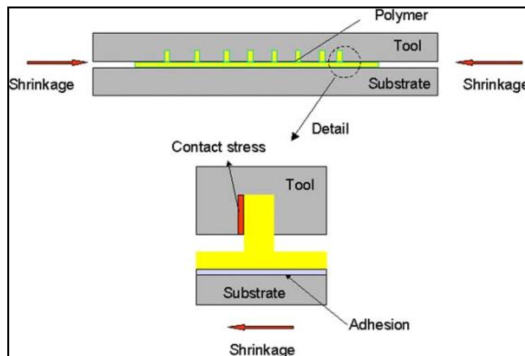

Fig. 1.13. Difference in shrinkage during demoulding causes high contact stress between the master microstructure and polymer perpendicular walls (Worgull, Heckele et al. 2005)

Such methods as high-frequency vibratory excitation assistance, rubber-assistance and gas-assistance are proposed to improve the process results (Linfa, Yujun et al. 2014; Liu and Dung 2005; Narijauskaite, Palevicius et al. 2013; Mekaru, Goto et al. 2007; Mekaru, Nakamura et al. 2006).

To avoid gas inclusions in the replicated microstructure, vacuum is applied during the replication process. Foil is placed in the thermal imprint device and vacuum is generated, which leads to absence of gas between the master microstructure and polymer (Kolew, Heilig et al. 2011; Roos, Wissen et al. 2003).

Assistance by high-frequency vibratory excitation (Fig. 1.14.) reduces the process duration and imprint pressure, as well as enhances the flow of molten polymer towards the master microstructure (Liu and Dung 2005; Seo and Park 2012; Lin and Chen 2006; Chien-Hung and Rongshun 2007) thus improving replicability. Additionally, assistance by high-frequency vibratory excitation is beneficial to the retraction of the master microstructure and reduces the contact surface stress, consequently eliminating possible damage (Mena, Manero et al. 1979; Zachariades and Chung 1987; Casulli, Clermont et al. 1990; Mekaru, Nakamura et al. 2006; Linfa, Yujun et al. 2014).

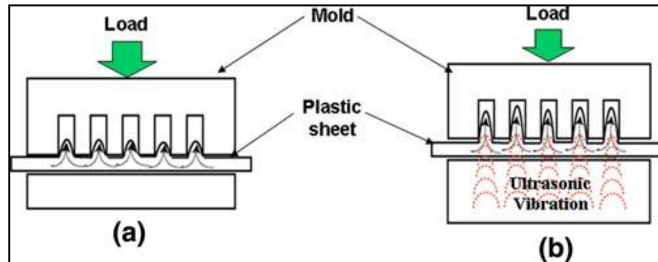

Fig. 1.14. Thermal imprint: without high-frequency vibrations (a); with high-frequency vibrations (b) (Mekaru, Nakamura et al. 2006)

1.3.4. A comparison of the processes

The most important parameters to be considered when selecting the technology for microstructure replication are: dimensions of the replicated features, cycle times, production output and expenses.

Thermal imprint enables to replicate microstructures with dimensions in the micro/nanometre range (Kolew, Heilig et al. 2011; Kolew, Münch et al. 2010; Julien, Thierry et al. 2007; Heckele and Schomburg 2004; Mehne 2008; Schift, David et al. 2000). UHE can be applied to emboss features of several micrometres (Khuntontong, Blaser et al. 2008; Hoffmeister 1988) and microinjection moulding is applied for replicating macro/microscopic features (Schift and Söchtig 1998).

The duration of thermal imprint ranges from several minutes to half an hour per single microstructure. (Worgull 2009; Mehne 2008). Therefore, the process is applicable for replicating microstructures in small to medium outputs (10 to 100 parts) (Julien, Thierry et al. 2007; Eusner, Hale et al. 2010). Microinjection moulding is characterized by cycle times of several minutes per microstructure and is appropriate for medium and large scale production (Heckele and Schomburg 2004; Kolew, Münch et al. 2010; Heckele, Bacher et al. 1998; Julien, Thierry et al. 2007). The duration of UHE process is approximately several seconds per single part (Khuntontong, Blaser et al. 2008; Khuntontong P. 2008; Khuntontong, Blaser et al. 2009), thus it is applicable in large scale manufacturing.

Microinjection moulding is the most expensive technology, while thermal imprint and UHE are economical methods for microstructure replication, with approximate equipment costs of 10,000 €. In addition, thermal imprint and UHE machines are uncomplicated when compared to microinjection moulding devices

(Madou, Lee et al. 2001; Khuntontong P. 2008; Sackmann, Burlage et al. 2015; Burlage, Gerhardy et al. 2012).

In general, thermal imprint and UHE are appropriate technologies which can replace traditional lithographic methods for the replication of precise microstructures (Schift, Jaszewski et al. 1999). However, microinjection moulding is more applicable for replicating structures with larger features (Schift, David et al. 2000; Schift and Söchtig 1998; Khuntontong 2008). Consequently, thermal imprint and UHE are chosen to replicate topologically complex microstructures.

1.4. Polymer rheology in thermal imprint technologies

Rheological behaviour of pre-heated polymer is analysed in order to comprehend the processes which occur during thermal replication.

1.4.1. Viscoelastic behaviour of the polymer

Amorphous and semi-crystalline thermoplastic polymers are applicable in thermal imprint technologies. They act as viscoelastic materials in the molten state and the deformation of molten polymer in the imprint process varies with respect to time. The viscoelastic behaviour of thermoplastic during the process is described by a combination of solid-body mechanical elements: spring, damper and friction body, i.e. Maxwell and Generalized Maxwell models (Fig. 1.15.) (Menges 1999; Pahl, Gleissle et al. 1995; Worgull, Heckele et al. 2003).

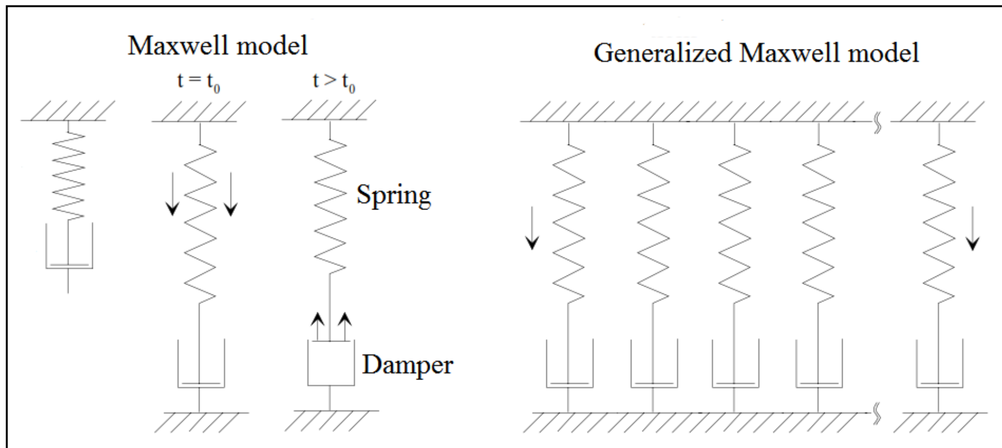

Fig. 1.15. Maxwell and Generalized Maxwell models

The Maxwell element contains a spring (elastic modulus – E) and a damper (viscosity – η) which are connected in succession. In order to approach the model to real conditions, more springs–damper elements are considered, i.e. Generalized Maxwell model is applied. The stress relaxation is expressed as Hook's law and relaxation performance of Generalized Maxwell model is expressed as a sum of individual Maxwell models (Menges 1999; Worgull, Heckele et al. 2003).

1.4.2. Molecular orientation and relaxation

The flow process deforms and orientates the polymer macromolecules in the direction of the flow. It is reversed through relaxation or preserved by rapid cooling. Relaxation is a function of temperature and depends on thermal motion of the molecular segments. The material reverts to the initial point due to limited duration of applied stress or high viscosity (low temperature) of the polymer. On the other hand, extended application of stress and high temperature increase the molecular mobility, which stimulates the polymer to move back to the initial order (Menges 1999; Worgull, Heckele et al. 2003). The decomposition of the orientations depends on the temperature and occurs through:

- Relaxation. A reduction of stress and decomposition of orientations by constant deformation.
- Retardation. The entire molecular chain is moved collectively. Molecules move spontaneously by taking new arrangement. Shrink films can be used as a practical example.

Relaxation is longer (approximately 10^4 times) when compared to retardation, since molecular chains do not move spontaneously but rather slide along each other.

1.4.3. Rheological description of the polymer melt

Two types of deformations occur in the polymer melt when thermal imprint technologies are applied (Menges 1999; Worgull, Heckele et al. 2003):

- Shear deformation. The adhesion between the melt and the master results in shear deformation. The melt flows laterally because of low Reynolds number and high viscosity.
- Stretch deformation occurs because of the delay or acceleration of the melt in the flow direction. Such deformations assist to plan orientations and are distinguished into uniaxial and biaxial. Stretch deformation is dominant at lower process temperature (slightly above glass transition temperature) while increased process temperature leads to higher shear deformation.

1.4.4. Structural viscous behaviour of the polymer

The viscosity of the polymer melt is not constant since shear stress and shear velocity are not proportional. Polymer melt acts linearly similar to Newtonian fluid under low shear rates; however, an increase of the shear rate induces non-linearity between shear rate and shear stress. Viscosity can be controlled through a magnitude of applied mechanical stress and temperature regulation; a temperature increase leads to decreased viscosity and increment of stress results in increased viscosity (Pahl, Gleissle et al. 1995; Worgull, Heckele et al. 2003). The thermal imprint models are mathematically described using the Cross method (Menges 1999; Worgull, Heckele et al. 2003); the viscosity function (Fig. 1.16.) is expressed by two straight lines.

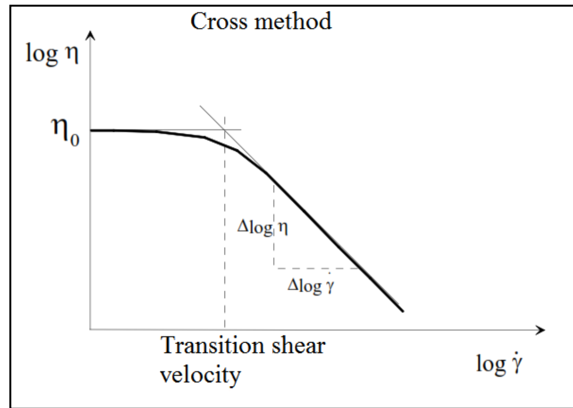

Fig. 1.16. A description of structural viscous polymer behaviour expressed using the Cross method

1.4.5. Cooling of the molten polymer (p-V-T diagram)

As the temperature is dissipating, the molecular chains of amorphous polymer lose mobility, the melt viscosity increases and the material solidifies. The change in enthalpy and specific volume is low during the transition phase. The volume decreases linearly above and below glass transition temperature (Fig. 1.17. (a)).

As the temperature is reduced, segments of semi-crystalline polymer are crystalized. The specific volume decreases and the crystallization heat, which must be removed before the polymer is cooled, is generated. Both firm and molten polymer are present under the crystallization temperature, which leads to the possibility of material shrinkage and cracks. The crystallization temperature depends on the cooling rate; a higher cooling rate decreases the crystallization temperature. The cooling down of the amorphous and semi-crystalline material is provided in p-V-T diagrams (Fig. 1.17.), which characterize the interaction between pressure – *p*, specific volume – *V* and temperature – *T*.

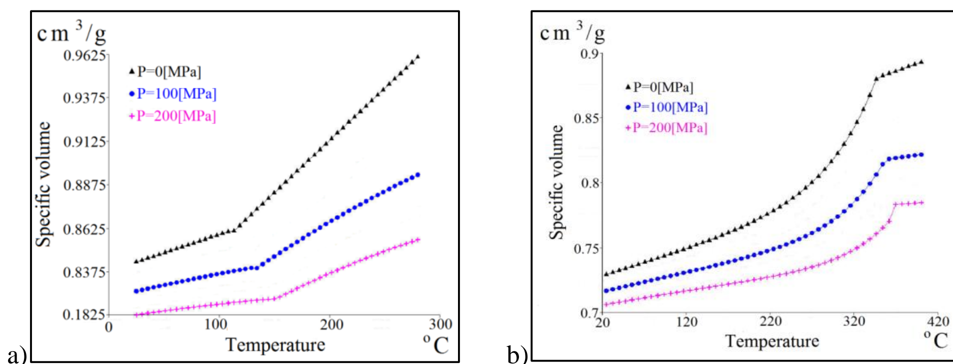

Fig. 1.17. p-V-T diagrams of amorphous (PMMA) (a) and semi-crystalline (PEEK) (b) polymers (Worgull, Heckele et al. 2003)

Plastic is compressible independently of the structure (amorphous or semi-crystalline) and state (molten or firm) and the specific volume depends on the pressure. The curve generated for amorphous polymer increases linearly above and below glass transition point while the glass transition temperature increases linearly with pressure. The curve for semi-crystalline polymer attains a paraboloid shape under the crystallization temperature and becomes linear above it. The increment of pressure results in a linear increase of the crystallization temperature.

The mathematical description of the p-V-T behaviour is provided using two approaches to approximation equations.

- The approach of coefficients is based on empirical investigations and explains the behaviour of amorphous and semi-crystalline polymers by eight coefficients (Thienel 1978).
- The Tait approach is established on the behaviour of specific volumes $V(T,p)$ and $V(T,0)$ under $p=0$. (Worgull, Heckele et al. 2003).

The p-V-T diagram is formed by derivatives of temperature and pressure-dependent values (Thienel 1978; Worgull, Heckele et al. 2003).

The resulting shrinkage must be considered in the p-V-T diagram when analysing the forming process, therefore, the characteristic pressure and temperature data are included in the diagram (Fig. 1.18.).

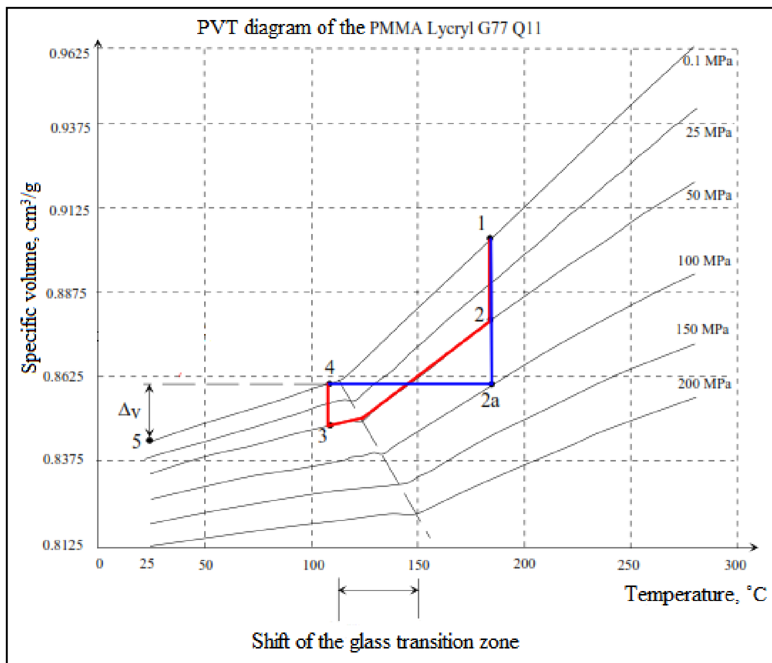

Fig. 1.18. The p-V-T diagram of thermal imprint process with isobaric (1-2-3-4) and isochoric (1-2a-4) cooling (Worgull, Heckele et al. 2003)

Two possible cooling options of the thermal imprint process, namely, isobaric and isochoric cooling are plotted in the p-V-T diagram.

- The process with isobaric cooling is described by the 1-2-3-4 curve. Line 1-2 characterizes the path-controlled isothermal imprint process and the pressure-controlled isobaric imprint initiates at point 2. Cooling below glass transition temperature begins at point 3. Line 3-4 specifies isothermal demoulding; the imprint pressure achieves ambient value and the specific volume increases.
- The 1-2a-4 curve describes the process with isochoric cooling. Line 1-2a specifies the path-controlled isothermal imprint process. The distance between the polymer and the master tool is kept constant and the polymer is demoulded. The imprint pressure must be sufficiently high to ensure that the polymer adapts to the profile of the master tool.

The specific volume difference between demoulding (point 4) and ambient (point 5) temperatures defines the polymer shrinkage. Isochoric cooling with assistance of pressure increment reduces the processing shrinkage.

1.4.6. Shrinkage

Thermodynamic material properties, such as compressibility and thermal expansion lead to polymer shrinkage. It is expressed by the relative deviation between any measurement of the master tool and the replicated part (Menges 1999; Worgull, Heckele et al. 2003).

The shrinkage is distinguished into radial (flow direction) and tangential process shrinkages. The difference between them characterizes the shrinkage anisotropy.

Shrinkage resistance is divided into internal and external. The master tool which surrounds the polymer induces external shrinkage resistance which relaxes the stress and reduces shrinkage. After the tool is demoulded, the free shrinkage emerges.

The internal shrinkage resistance is induced by the cooling-caused stresses and orientations. The temperature profile increases with the thickness of the polymer part as a result of low heat conductivity. Consequently, every single layer of the part demonstrates a different contraction potential. The outer layers are characterized by lower temperature than the inner layers. The temperature difference induces internal stresses.

The difference between linear heat expansion coefficients in the orientation direction results in different shrinkage values. The molecular orientation, which is dependent on the flow direction, and the relaxation of the orientation contribute to the anisotropy of shrinkage. The sum of shrinkage anisotropies leads to the distortion of the polymer part (Menges 1999; Worgull, Heckele et al. 2003).

1.4.7. Polymer flow

The process of the polymer melt flow is different from those which occur within the fluids of low molecular weight. The flow of the fluids of low molecular weight takes place as a result of individual molecules jumping to the neighbouring empty position. Higher temperature induces higher kinetic energy, therefore, the reactions between molecules are more frequent and the existence of the stress makes the flow

more direct. On the other hand, if there is no empty space in the molecule, then even a high amount of energy is not capable to induce the flow.

Polymers are characterized by stretched, flexible molecule chains and strong intermolecular interaction. Rubbery elastic deformation is implemented by moving macromolecular segments in accordance with the direction of acting stress, which shifts the mass centre of the macromolecule.

The polymer flow requires a sufficient amount of activation energy, which is generated by activation heat and entropy of viscous flow. The increment of activation energy in viscous flow is observed until the appropriate magnitude of molecular mass is achieved. If the length of the polymer chain exceeds the length of the segment, the activation energy is no longer dependent on the molecular mass of the polymer. Viscous flow of the polymers is evaluated by centre of gravity displacement of the macromolecules. The higher molecular mass of the polymer, the more coordinated movements must occur in order to move the centre of gravity.

1.4.8. Rheological characteristics and their dependence on vibrations

The application of high-frequency vibratory excitation enhances polymer (amorphous and crystalline) melt flow, thus improving the replicability of the imprint process (Kong, Xu et al. 2009). The increased vibration frequency reduces the melt viscosity and increases the flow rate. In addition, the increment of the vibration amplitude decreases the melt viscosity at constant frequency. The dependence between the polymer flow and high-frequency vibratory excitation demonstrates that the most significant decrease in polymer viscosity is obtained at lower melt temperatures (Li and Shen 2008; Li, Shen et al. 2006).

The application of high-frequency vibratory excitation in polymer processing enhances mechanical properties, such as tensile strength, elastic modulus, etc..(J. B. Li 2010; An, Gao et al. 2015)

1.5. Quality assessment

1.5.1. Diffraction efficiency

Diffraction efficiency η is the deviation between the theoretically ideal and the physically implemented CGH. It is the relation between the energy which passes to a particular area g_r and total energy which enters the microstructure (Giuseppe A. Cirino 2011; Soifer, Kotlar et al. 1997).

$$\eta = \frac{\sum_{m=-\frac{A}{2}}^{+(\frac{A}{2})-1} \sum_{n=-\frac{B}{2}}^{+(\frac{B}{2})-1} \left| g_{m-M_0,\, n-N_0} \right|^2}{MN}, \quad (3)$$

Similarly, diffraction efficiency can be expressed as the ratio of the diffracted and transmitted energy. The equation attains the following expression:

$$\eta = \frac{\eta_D}{\eta_T}, \quad (4)$$

here: η – diffraction efficiency, η_D – diffracted energy, η_T – transmitted energy. The diffracted energy is expressed as:

$$\eta_D = \frac{\sum_{m=-\frac{A}{2}}^{+\frac{A}{2}-1} \sum_{n=-\frac{B}{2}}^{+\frac{B}{2}-1} \left| g_{m-M_0, n-N_0} \right|^2}{\sum_{m=-\frac{A}{2}}^{+\frac{A}{2}-1} \sum_{n=-\frac{B}{2}}^{+\frac{B}{2}-1} \left| g_{m,n} \right|^2}, \quad (5)$$

The transmitted energy is expressed with:

$$\eta_T = \frac{\sum_{m=-\frac{A}{2}}^{+\frac{A}{2}-1} \sum_{n=-\frac{B}{2}}^{+\frac{B}{2}-1} \left| G_{k,l} \right|^2}{MN}, \quad (6)$$

here: M and N – two-dimensional rectangular elements of the hologram plane, M_0 and N_0 – coordinates of central reconstruction window, $G_{k,l}$ – complex transmittance, $g_{m,n}$ – discrete inverse Fourier transform, A and B – dimensions of the reconstruction window.

The total energy of phase-only holograms composes the signal $\eta = \eta_D$, while amplitude-only holograms absorb half of the energy, i.e. η_T=0.5 and η_D=0.25. As there is a twin signal, 25 percent of energy is applied for generating the signal (Bracewell 1986).

Higher diffraction efficiency values in +1 and –1 maxima of the periodic microstructure are needed in many applications, as they indicate high-quality of DOE (E. Popov; Hirai, Yoshida et al. 2003).

1.5.2. Atomic Force Microscope

The technique which is established on the concepts of scanning tunnelling microscope (STM) allows observing the atomic size features of the surface morphology (Binnig, Quate et al. 1986; Raposo, Ferreira et al. 2007; Binnig, Rohrer et al. 1982; Binnig, Quate et al. 1986; Binnig and Rohrer 1999). The AFM registers the topographic images in the x and y directions. The registered surface elevations are related to x and y coordinates, thus the image is described in terms of a matrix with N lines and M columns and z(x,y) as the function of height (Clarke 1994).

The distance between the AFM tip and the investigated surface is the critical factor which influences the topographic data acquisition. If the interatomic distance is significant, the attractive force between the tip and the surface is low, but as the tip approaches the surface, the attraction increases until the atoms are so close that the electron clouds begin to repel each other electrostatically. The interaction forces approach zero at a distance of several angstroms. Normally, the topographic images are acquired while keeping the extent of interactions constant throughout the tip

scanning, in direct contact (contact) and intermittent contact (tapping) approaches. In the contact mode, the tip wears due to the abrasive and adhesive contact with the surface, what leads to tip contamination and surface damage; deformations can also arise causing the elastic wear out in the non-contact mode. Thus, the interactions between the tip and the surface may cause topographic image artefacts and sometimes surface damage. Since the form and structure of the tip is conditioned by the sample, the tip used for a particular investigation is important in order to achieve proper results. Regarding the shape, tip artefacts may arise if the surface features are of the same or smaller magnitude when compared to the tip. When this occurs, the tip can no longer adequately represent the profile curves. Feature broadening is one of errors which occurs as the radius of the tip curvature is comparable or larger than the size of the surface feature.

Tip contamination is another cause for image distortion convolution, as the size of the contaminant is close to the surface size features. In order to avoid this, the state of the tip must be evaluated before making each measurement. The status of the tip can be verified by scanning the bi-axially oriented polypropylene (BOPP) film. If the tip is contaminated or damaged, the fibre-like network is not detected (Nie, Walzak et al. 2004). The BOPP is chosen since it is soft, hydrophobic and has low surface energy; all these features allow avoiding the tip contamination (Nie, Walzak et al. 2002).

Tip compression against the feature is another type of image distortion which occurs as the tip is above the feature and pressures it. This can cause surface damage and an error in the image. For such experiments, carbon nanotube tips are the most rational choice when aiming to avoid tip compression, since these tips are flexible, which limits the force on the sample and inhibits the surface damage (Guo, Wang et al. 2005).

The AFM cantilevers are required to have low spring constant and high resonant frequency. A qualitative measurement demands cantilever adjustment, which involves determining the elastic constant and considering whether the stiffness is acceptable for observing a particular surface.

Using the contact approach, the spring constant of the cantilever bounds both the minimum tracking force applied on the surface and the speed of scanning (Cleveland, Manne et al. 1993). The value of the spring constant of the cantilever restricts the scanning speed when working in the non-contact regime (Burnham, Chen et al. 2002; Velegol and Logan 2002; Cumpson, Hedley et al. 2004).

1.6. The aim and objectives of the dissertation

The study of literature reveals that UHE and thermal imprint are appropriate technologies for microstructure replication due to such advantages as low cost and the size of replicated features. However, there are deficiencies which must be eliminated in order to make these technologies completely applicable for replicating topologically complex microstructures. Moreover, there is no established technology for replicating the entire surface of a microstructure with high-quality and uniformity.

In addition, the data on how the quality of the replica is influenced by the process regimes are limited.

UHE is technology for replicating microstructures with features smaller than 1 mm (Schomburg, Burlage et al. 2011). However, there is limited information about imprinting microstructures with features of several micrometres, therefore it is necessary to establish the process flow in order to apply this method for microstructure replication. The flow initiates with experiments exploiting pre-structured foils, with an aim to determine how additional heat generation by applying the foils influences the set of appropriate process parameters. The embossing of microstructures is performed under the established sets of appropriate process parameters. Consequently, the influence of process parameters and the application of pre-structured foils on the quality of the replicated microstructure is determined.

Low filling ratio and polymer distortions of the replicated microstructure are the predominant defects of thermal imprint process. High-frequency vibratory excitation is selected as a measure to eliminate these problems. Therefore, two different VAPs are designed and applied in the experiments of thermal imprint to ensure uniform displacement field throughout the entire surface. The quality of the replica is investigated by applying non-contacting diffraction efficiency measurement and AFM. These methods enable to compare the adequacy between the replicated and theoretically ideal products.

The replication of periodic microstructures is performed to facilitate the study of RDE and compare the quality of the replica with theoretically ideal values. When the aim is achieved and the process is established, it is necessary to combine the process flow of topologically complex microstructure design, realization and replication, i.e. to develop a design, fabrication and replication of a topologically complex master microstructure by applying CGH, EBL and thermal imprint technologies.

According to the study of literature, **the aim of the dissertation** is to: investigate the influence of high-frequency vibratory excitation on the quality of microstructures replicated using thermal imprint technologies.

To achieve the aim, the following **objectives have been established**:

1. To select the methods, equipment and materials enabling to design, fabricate and replicate microstructures by using high-frequency-assisted thermal imprint technologies.
2. To develop a master microstructure for the replication on polymer by using high-frequency-assisted thermal imprint technologies.
3. To develop a microstructure replication technology which operates on the basis of high-frequency vibrations, ensuring high-replicability and uniformity of the replicated microstructure.
4. To characterize microstructures replicated by applying imprint technologies with assistance of high-frequency vibrations.

2. MATERIALS AND EQUIPMENT

This chapter presents the materials and equipment which are necessary for the fabrication and replication, as well as dynamic and quality analysis of the master microstructure.

The first part of the chapter introduces the equipment which is applied for the fabrication of the master microstructure, thermal imprint, UHE, ODS and microstructure quality analysis. The materials which have been used in the study are described in the second part of the chapter.

2.1. The experimental equipment

EBL system: Raith e-LiNEplus high-resolution electron beam lithographic system equipped with Schottky thermionic field emission gun is applied to fabricate the master microstructure.

The travel range of the EBL device is 100×100 mm. The machine exploits thermal field emission filament technology and a laser interferometer-controlled platform. The column voltage varies from 100 V to 30 kV and the laser stage can move with an accuracy of 2 nm. The system is equipped with six apertures of different size: 7.5, 10, 20, 30, 60, and 120 µm. The current of the electron beam is controlled by choosing the appropriate aperture.

Typically, larger patterns are separated into smaller writing fields which are subsequently joined together to form the finished pattern. Usually, the writing field area is 100 μm^2 and the pixel size is 2 nm^2; however, the size of the writing field can vary from 500 nm^2 to 2 mm^2.

The system uses three software packages for proximity effect corrections, 3-D lithography and metrology.

Thermal imprint equipment: A hydraulic device (Fig. 2.1.) constructed by a team of scientists at the Institute of Material Science (KTU) is applied in thermal replication of microstructures. The main characteristics of the equipment are provided in Table 2.1.

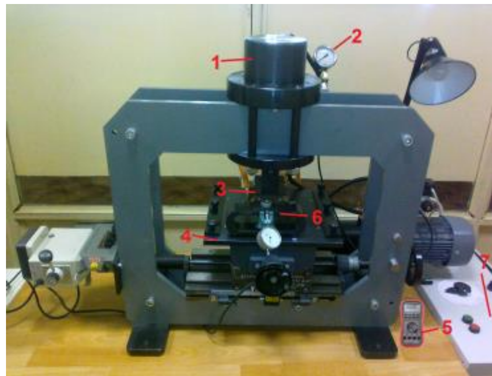

Fig. 2.1. The device for thermal imprint: hydraulic piston (1), pressure gauge (2), horn (3), stage (4), thermometer (5), dynamometer (6), control block for temperature, imprint duration and pressure (7).

Table 2.1 The characteristics of the thermal imprint device

Range of temperature, ˚C	20–200
Range of pressure, N/m^2	$0–10^6$
Horn measurements, mm	20×20

UHE equipment: HIQ Dialog 1200 device (Fig. 2.2.) manufactured by Herrmann Ultrasonics is applied in the UHE process.

Fig. 2.2. HiQ DIALOG 1200 UHE experimental setup: display (1), UAT (2), anvil with the master mould and a polymer piece on it (3), heating tool (4).

Ultrasonic vibratory excitation is generated by piezo-ceramic. The operating frequency and amplitude of the device are 35 kHz and 16.3 μm, correspondingly. The following parameters can be modified according to the process conditions:

- Trigger force. The force of the imprinted UAT at which ultrasonic vibratory excitation initiates. The trigger force ranges from 0 to 650 N.
- Force of vibrations. The force of a vibrating UAT which is imprinted into the substrate. The force of vibrations ranges from 0 to 650 N.
- Duration of vibrations. The duration of the application of ultrasonic vibratory excitation is determined correspondingly to the processed polymer and its thickness.
- Solidification force. The force applied to solidify the molten polymer, which initiates after the UAT ceases to vibrate.
- Solidification duration. The duration for applying the solidification force which is imposed with regards to the processed polymer and its thickness.

2.2. Measurement equipment

The piezoelectrically-driven VAPs vibrate with the amplitudes of micrometre order, hence, the equipment must be capable to detect such amplitudes. According to the prerequisite, the holographic interferometer and LDV are applied in the experimental ODS study.

ESPI holography system PRISM: The setup (Fig. 2.3.) manufactured by HYTEC is applied for analysing the VAPs ODS.

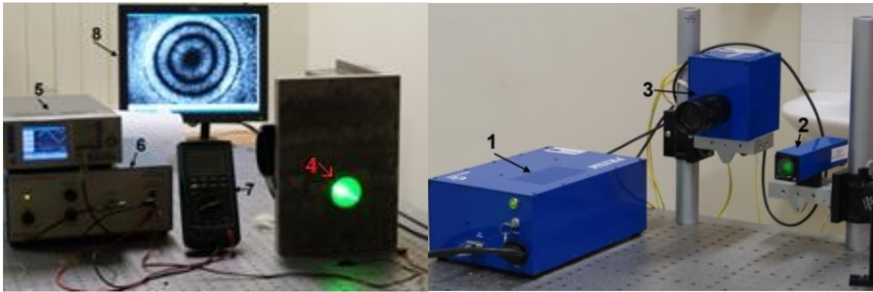

Fig. 2.3. The PRISM system setup: control block (1), illumination head of the object (2), video head (3), VAP (4), signal generator (5), amplifier (6), voltmeter (7) and interference fringe (8)

The setup operates on the basis of holographic interferometry (Fig. 2.4.). The object beam passes through the lens system, moves to the analysed object, and is reflected from it. The reference beam arrives at the camera, where it interferes with the reflected object beam. The interference patterns are transferred to a computer, where they are processed with the PRISMA-DAQ software.

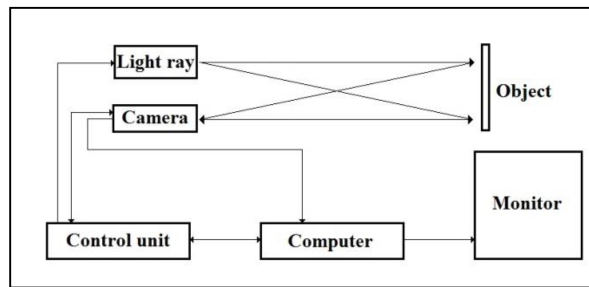

Fig. 2.4. The operating scheme of the PRISM system optical setup

Displacements which occur in the VAP are in the micrometre order. The digital holographic interferometry enables to visualize the dynamic processes of such scale in real-time and full-field mode. It is one of the most effective techniques for the study of dynamic processes (Valin, Gonçalves et al. 2005). The results obtained by using this method are vibration responses with modes at specific frequencies. White regions are described as nodes, i.e. the displacement is zero. Black regions are zones which vibrate with a particular amplitude. The characteristics of the PRISM system are presented in Table 2.2.

Table 2.2 The characteristics of the PRISM system

Sensitivity Measurement	< 20 nm
Dynamic Range	10 µm
Range Measurement	> 100 µm
Largest Part Size	1 meter diameter
Working Distance	>1/4 meter
Data Acquisition Rate	30 Hz
Laser	20 V

LDV OFV-5000. The device (Fig. 2.5.) is manufactured by POLYTEC. It enables to perform non-contact frequency response analysis of the vibrating object.

The LDV setup operates as follows: a laser beam passes through the beam splitter and is divided into object and reference beams. Subsequently, the object beam arrives at the vibrating object and is reflected. The object beam approaches the second beam splitter which divides the beam and directs it towards the third beam splitter. Here, the object beam interferes with the reference beam. The ODS of the object is interpreted as black/white interferential fringes.

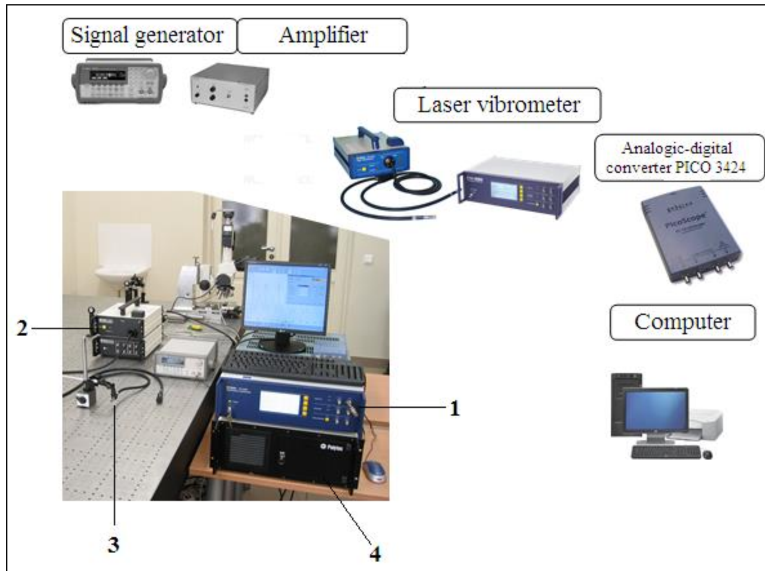

Fig. 2.5. The experimental setup of LDV Polytec: Vibrometer Polytec OFV-5000 (1), Interferometer Polytec OFV-512 (2), Sensor head Polytec OFV-130-3 micro-spot (3), Polytec computer (4)

The depth and period of microstructures are 600 nm and 4 μm, respectively. Consequently, the equipment must be capable to analyse microstructures of such geometrical parameters. The quality analysis is performed by applying the following devices:

- Optical microscope Keyence VHX-500F
- AFM (AFM) NT-206S
- Laser diffractometer

Optical microscope Keyence VHX-500F. The device (Fig. 2.6.) is manufactured by KEYENCE and is employed to analyse the pyramid tool and the pre-structured PC. The microscope generates high-definition (18 million pixels) 2D and 3D profile images and indicates the depth. The apparatus includes a VH-Z100R model lens whose magnification ranges from 100 to 1000 times. The field of view varies from 0.0610 to 3200 mm^2.

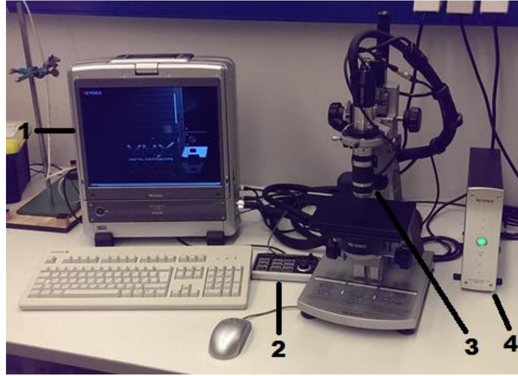

Fig. 2.6. The optical microscope Keyence VHX-500F: the monitor (1), the touch pad console (2), the optical column (3), the computer (4)

AFM NT-206S: The device is manufactured by NANOTOP and applied in the investigation of surface morphology.
The characteristics of AFM NT-206S are:

- Process modes:
  - Static
  - Dynamic
  - Static/dynamic force spectroscopy
- Maximum scanning area: 30×30 µm
- Measurement environment: 512×512 points
- Maximum height of irregularities: 4 µm
- Horizontal resolution: 2 nm
- Upright resolution: 0.1– 0.2 nm
- Scanning speed: 10 µm /sin X–Y plane

Laser diffractometer (Fig. 2.7.) is constructed for measuring diffraction efficiency. The analysis of diffraction efficiency initiates by illuminating the sample with laser light which diffracts as it passes through the sample. The intensity values of the diffracted maxima are registered by a photodiode which is connected to the ammeter. The electric current, which is registered by the ammeter, is directly proportional to the light intensity. RDE is calculated by applying the following equations:

$$RE_{i,j} = \frac{I_{i,j}}{I_j} \quad , \tag{7}$$

$$I_j = \sum_i I_{i,j} \quad , \tag{8}$$

here: $RE_{i,j}$ – RDE, $I_{i,j}$ – the light intensity of maxima and I_j – the sum of light intensities.

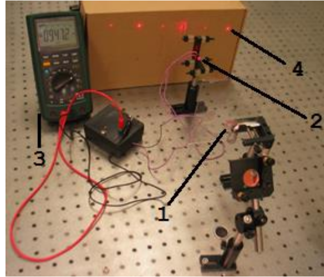

Fig. 2.7. Diffraction efficiency measurement setup: the sample (1), the photodiode (2), the ammeter (3) and distribution of diffraction maxima (4)

2.3. Materials

PMMA ($(C_5O_2H_8)_n$) (molecular mass – 35K) is applied as a resist during the formation of CGH. The general properties of the material are presented in Table 2.3.

Table 2.3 The general properties of PMMA

Density	1.18 g/cm^3
The glass transition temperature (T_g)	105 °C
Melting point	160 °C
Refractive index (n_D)	1.4905

Nickel film is utilized to metalize the master microstructure. The general properties of nickel film are presented in Table 2.4.

Table 2.4 The general properties of nickel film

Melting point	1455 °C
Density	8.908 g/cm^3
Young's modulus	200 GPa

PC. Amorphous PC is used in thermal microstructure replication because of its linear pressure-volume-temperature dependency. This linearity enables to avoid cracks and distortions in the demoulding step. Thermal, chemical, and physical characteristics of the PC are presented in Tables 2.5–2.7.

Table. 2.5 The thermal properties of PC (Pérez, Vilas et al. 2010)

Melting temperature (T_m)	267 ˚C
Glass transition temperature (T_g)	150 ˚C
Heat deflection temperature – 10 kN	145 ˚C
Heat deflection temperature – 0.45 MPa	140 ˚C
Heat deflection temperature – 1.8 MPa	128– 138 ˚C
Upper working temperature	115– 130 ˚C
Lower working temperature	–40 ˚C
Linear thermal expansion coefficient	65– 70*10^{-6} /K
Specific heat capacity	1.2– 1.3 kJ/(kg*K)
Thermal conductivity 23˚C	0.19– 0.22 W/(m*K)

Table. 2.6 The mechanical properties of PC

Young's modulus	2.0–2.4 GPa
Tensile strength	55–75 MPa
Compressive strength	>80 MPa
Poisson's ratio	0.37
Coefficient of friction	0.31

Table. 2.7 The physical properties of PC

Density	1.20–1.22 g/cm
Refractive index	1.584–1.586
Water absorption – equilibrium	0.16–0.35 %
Water absorption – over 24 h	0.1 %
Light transmittance	88 %

Piezoelectric materials. Lead zirconate titanate (PZT-4 and PZT-5) piezoceramic rings are applied as actuators in VAP device designs; both actuators operate in the thickness mode (d_{33} direction). The characteristics of PZT-4 and PZT-5 are presented in Tables 2.8–2.9.

Table 2.8 The properties of PZT-4

General	
Density $(10^3 kg/m^3)$	7.5
Curie temperature (˚C)	328
Elastic Constants	
c_{11}^E (GPa)	139
C_{33}^E (GPa)	115
Piezoelectric constants	
e_{31} (C/m^2)	–5.2
e_{33} (C/m^2)	15.1
e_{15} (C/m^2)	12.7
Dielectric constants	
ε_{11}^T $(10^{-9} F/m)$	6.461
ε_{33}^T $(10^{-9} F/m)$	5.620

Table 2.9 The properties of PZT-5

General	
Density $(10^3 kg/m^3)$	7.75
Curie temperature (˚C)	350
Elastic Constants	
c_{11}^E (GPa)	15
C_{33}^E (GPa)	18.8
Piezoelectric constants	
e_{31} (C/m^2)	–10.6
e_{33} (C/m^2)	24.8
e_{15} (C/m^2)	38.2
Dielectric constants	
ε_{11}^T $(10^{-9} F/m)$	1730
ε_{33}^T $(10^{-9} F/m)$	1700

2.4. The conclusions of the chapter

The equipment and materials are selected correspondingly to the initial requirements. The Raith e-LiNEplus electron beam lithography system is used to fabricate the master microstructure with features of several micrometres.

ODS analysis of the VAP device designs requires high definition and capacity to register the amplitudes of micrometre order, thus the holographic interferometry system PRISM and LDV Polytec are applied for the analysis.

The thermal imprinting experiments are performed with a hydraulic thermal imprint device. HiQ DIALOG 1200 machine made by Herrmann Ultrasonics was selected for the UHE process. This device provides sufficient imprint pressure which is required to transfer the profile of the master microstructure to the polymer.

The depth and period of the periodic microstructure are 600 nm and 4 μm, respectively. Following the requirements, AFM NT-206S has been selected for the study of surface morphology, and the diffraction efficiency is measured with a laser diffractometer.

PZT-4 and PZT-5 piezoelectric materials are applied to fabricate VAPs. Amorphous PC has been chosen as a substrate for thermal replication due to its linear pressure-volume-temperature characteristics which reduce the likelihood of defects.

3. MICROSTRUCTURE DESIGN, REALIZATION AND REPLICATION

To perform thermal microstructure replication, it is necessary to design and fabricate the master microstructure. The EBL technology enables to fabricate the periodic master microstructure, however, the fabrication of a topologically complex master microstructure poses certain issues and requires novel design and fabrication. This chapter describes the use of CGH technology involving the Gerchberg-Saxton algorithm with FFT to design the master microstructure as well as the application of EBL to fabricate it.

Secondly, the chapter explains the utilization of the UHE process for replicating high-quality microstructures. The influence of additional heat generation through pre-structured foils on the size of appropriate process parameter set is analysed in this chapter.

Finally, the chapter explains the high-frequency vibratory excitation-assisted development of a thermal imprint. VAPs generate ODS with uniform displacement field throughout their entire operating surface; for the thermal imprint process, they are numerically simulated, fabricated and experimentally analysed. Numerical frequency response analysis and experimental verification are performed in order to determine the operating frequencies of the devices. The ODS ensures a uniform polymer flow towards the master microstructure.

3.1. Generating a computer-generated hologram

The Gerchberg-Saxton algorithm with FFT is applied in CGH computation. When discrete data is involved, DFT for digital signal processing is employed. The transformation converts space/time-based data into frequency-based data and the conversion is described with the following formula:

$$F(u,v) = \frac{1}{NM} \sum_{x=0}^{M-1} \sum_{y=0}^{M-1} f(x,y) e^{-i2\pi\left(\frac{xu}{M}+\frac{yn}{N}\right)}, \tag{9}$$

here: u and v – discrete spatial frequencies, M and N – the quantity of sections in x and y directions of space and frequency domains, $F(u,v)$ – 2D discrete $f(x,y)$ spectra (Giuseppe A. Cirino 2011).

Initially, an arbitrary number generator creates phase scattering $\varphi[-\pi, \pi]$. The steps of Gerchberg-Saxton algorithm are the following:

The initial field u_n^H is calculated in the hologram plane:

$$u_n^H = A(I_H)\exp(i\varphi_{n-1}^H), \tag{10}$$

The initial field u_n^H is propagated from the image plane to the object plane and the amplitude information is discarded:

$$\varphi_n^T = P(FFT(u_n^H)), \tag{11}$$

The amplitude and phase of the illumination field are added to the phase information in order to retrieve the object field u_n^T :

$$u_n^T = A(I_T)\exp(i\varphi_n^T) , \tag{12}$$

The object field u_n^T is propagated from the object plane to the image plane:

$$\varphi_n^H = P(FFT^{-1}(u_n^T)) , \tag{13}$$

The reconstructed I_n and the expected images are compared and iterative quality assessment begins. The correlation between the images is calculated in order to determine the necessity of additional iterations. The calculations finish when adequate quality of the hologram is achieved, i.e. further iterations do not improve the quality, which is defined by a specific threshold:

$$I_n = \left|u_n^T\right|^2 , \tag{14}$$

The phase of the reconstructed image is combined with the field amplitude of the expected irradiance and should additional iterations be necessary, the process is repeated from the initial step.
The amplitude extracting function *A(z)* of complex numbers is defined as follows:

$$A(z) = \sqrt{x^2 + y^2} , \tag{15}$$

The angle extracting function *P(z)* is expressed as:

$$P(z) = \tan^{-1}(\frac{y}{x}) , \tag{16}$$

CGH generation is realized with *Matlab* software. A direct DFT computation of *N*-point requires N^2 complex multiplications and $N(N-1)$ complex additions. However, FFT reduces the amount of calculation.

The logo of KTU (Fig. 3.1.) is used to realize the algorithm and establish the process flow.

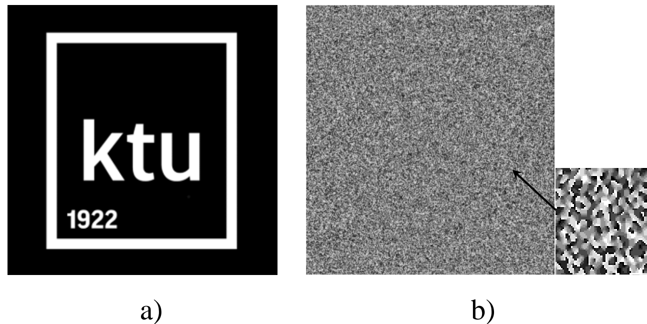

a) b)

Fig. 3.1. The logo of KTU (a) and its CGH (b)

The hologram is 2×2 mm in size and has 10^6 pixels. It is designed for the exposition on PMMA (molecular mass – 35K; refractive index – 1.49). Laser light (wavelength – 632.8 nm) is applied to reconstruct the hologram. Its pixels have eight greyscale levels, i.e. black colour denotes zero exposition (maximum PMMA thickness) and white area designates maximum exposition (minimum PMMA thickness).

3.2. The realization of a CGH by using Electron Beam Lithography

The process of EBL is carried out by using the Raith e-LiNEplus EBL system. The steps of the EBL process are:

1) A silicon wafer (size – 10×10 mm) is exposed to the oxygen plasma. The duration of exposition is 5 min.
2) The silicon wafer is heated on a hot plate for 30 min at the temperature of 150° C.
3) The wafer is spin-coated with PMMA. The rotational frequency of spin-coating is 2000 rpm.
4) The PMMA is hardened. The temperature of hardening – 200° C.
5) The EBL process. The acceleration voltage – 10 kV.
6) The development of PMMA. The solvents of 1:3 methyl isobutyl ketone (MIBK) and isopropyl alcohol (IPA) are applied in the development.
7) Washing the samples with water and drying with compressed air flow.

The fabricated microstructure is metalized with nickel film (thickness – 20 nm, $T_{melting}$ = 1455 °C, purity – 99.99 %) by applying electron beam evaporation ($T_{substrate}$ = 20 ˚C, residual gas pressure – 10^{-4} Pa, deposition rate v = 1–2 nm/s).

UV light hardening is carried out by applying acrylic trimethylolpropane-ethoxylate (layer thickness – 2 μm, area – 3 cm^2), PET substrate, and a home-made device (T=20 °C, irradiation distance – 10 cm, UV light source DRT-230: λ=360 nm, I=10000 lx).

A copy of the test structure is fabricated making a direct polymer replica by sandwiching the UV-photopolymer between the test structure stamper and the substrate. When the test structure is removed, the replica is left for post-polymerization. The duration of exposure is defined experimentally.

Finally, a nickel stamp is fabricated by using the electroplating process (with nickel-sulfonate ($Ni(SO_3NH_2)$) electrolyte and additives). The process conditions of electroplating are the following: pH 3.5–4.5, temperature – 50 ˚C, electric current density – 4 mA/cm^2).

3.3. The investigation of a CGH

Normally, CGHs are distributed into writing fields and the electron beam is exposed to one pixel after another within this writing field. However, exposing the pixels in rows or columns causes their overlapping and rounded corners due to the beam distribution according to the Gaussian law. Consequently, dividing the pixels into four portions is proposed as a solution to this problem. The pattern is divided into smaller subdivisions to expose larger regions, therefore the exposition time increases four times, since it is necessary to expose 4×10^6 pixels. On the other hand, the quality

of the hologram increases. The aforementioned improvement increases the RDE of the fabricated hologram (58 %), when compared to a normally exposed hologram (29 %).

The images of the exposed holograms are presented in Fig. 3.2. The area of the writing field is 100 μm^2 and the pixel dimensions are 2×2 μm. Fig. 3.2. (a and b) demonstrates the writing field stitching error and the overlapping pixels. The writing field without the stitching error is provided in Fig. 3.2 (c). The heights of the pixels are: 200, 400, 600, 800, 1000, 1200, 1400 and 1600 nm corresponding to 8 greyscale levels.

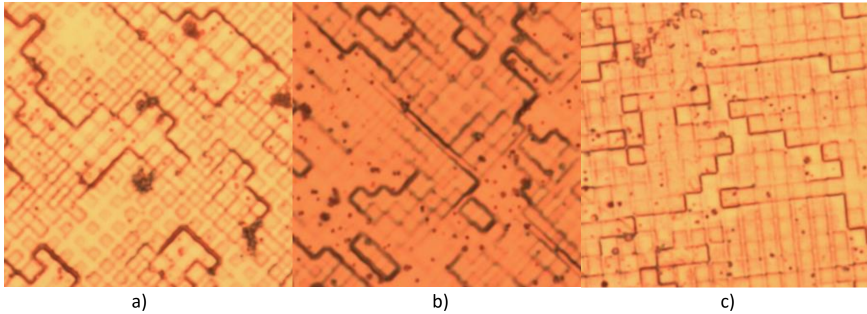

Fig. 3.2. Pictures of CGHs generated on PMMA: a stitching error (a), overlapping pixels (b) and the exposed area without a stitching error (c)

3.4. Results

During the improvement of the process flow, six trial holograms were fabricated (Fig. 3.3.). The reconstructed diffraction image of the KTU logo is provided in Fig. 3.4. The RDE measurements of the metalized CGH illuminated with lasers of three different wavelengths, namely, 632.8 nm (red colour), 441.6 nm (blue colour) and 532 nm (green colour) are performed. The measurement results are presented in Fig. 3.5.

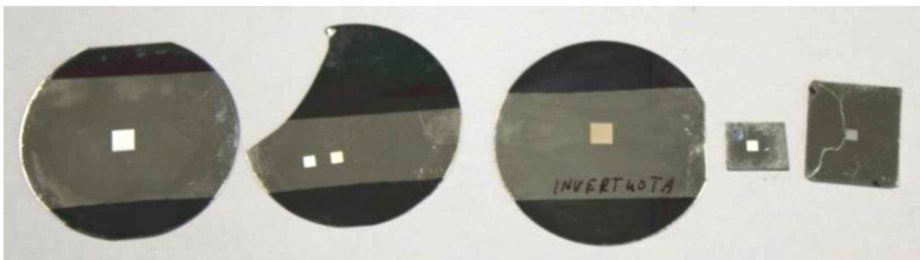

Fig. 3.3. CGHs generated on the PMMA

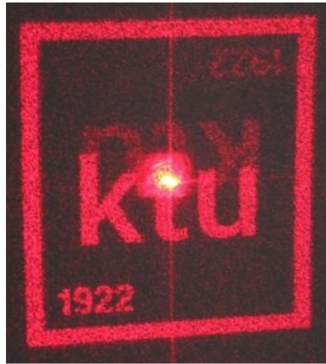

Fig. 3.4. The diffraction view of the KTU logo CGH

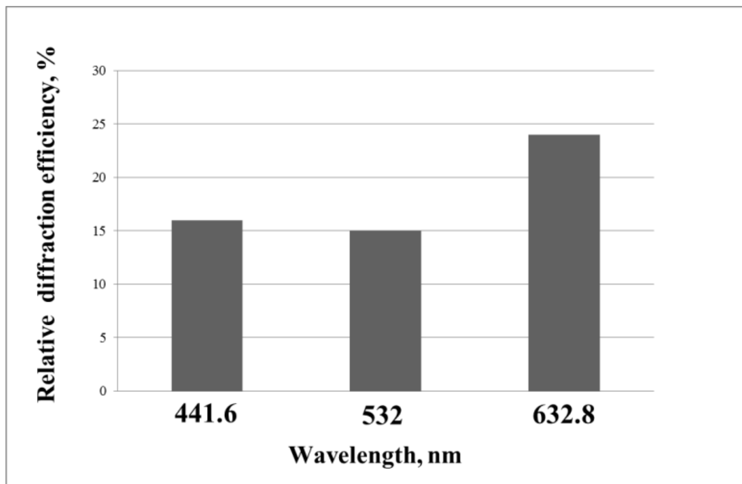

Fig. 3.5. The relation between the RDE and the wavelength of the laser light

The CGH is designed for illumination with the wavelength of 632.8 nm (red light), therefore it is characterized by the maximum value of the RDE (24 %) when the wavelength of 632.8 nm illuminates the CGH. The wavelengths of 441.6 and 532 nm generate RDE of 16 and 15 %, respectively.

The RDE decreases from 58 to 24 % throughout the processing steps. The most significant decrease is observed after the UV light hardening process.

The next step is thermal imprint experiment of the fabricated CGH into the PC. The AFM images of the master microstructure and the replica are presented in Fig. 3.6.

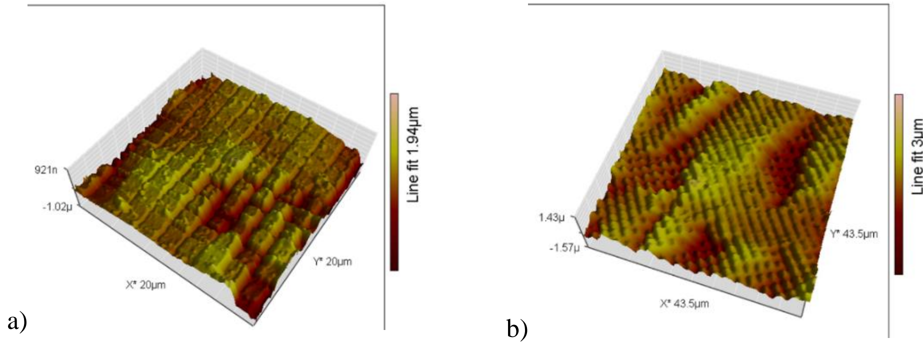

Fig. 3.6. The difference between the master microstructure (a) and its thermal replica (b)

The thermal replica differs from the master microstructure, i.e. it includes rounded edges etc., therefore further process improvement by applying high-frequency vibratory excitation is necessary.

3.5. The Ultrasonic Hot Embossing process

The UHE process depends on the temperature distribution within a stack of thermoplastic foils, hence the process results can be modified by navigating the absorption of ultrasonic energy between the layers of thermoplastic foils. The ultrasonic energy is concentrated on the reduced contact zone (protruding features) between the thermoplastic layers. The friction between these layers depends on the roughness of the foils. Sets of appropriate process parameters with different foil orientations are compared in order to determine how the process parameters are governed by the additional heat generation through increased surface roughness (pre-structured foils). This enables to establish minimal replication parameters. Finally, experiments with periodic microstructures are performed and the effect of additional heat generation on the quality of replicated microstructures is investigated.

3.5.1. The fabrication of pre-structured foils

The aim of pre-structured foils is to generate additional heat through increased surface roughness. Pre-structured PC foils (Fig. 3.7. (b)) of constant surface roughness are replicated by ultrasonically embossing aluminium with a milled pyramid tool (Fig. 3.7. (a)).

a)

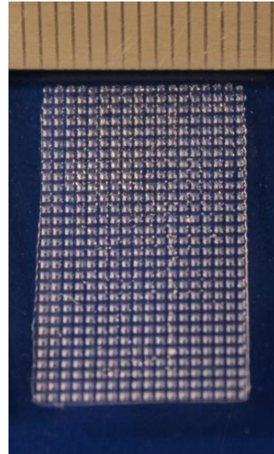

b)

Fig. 3.7. The pyramid tool milled on the aluminium (a) and the embossed pyramid tool on the PC (b)

PTC Creo 3.0. CAD software is applied to design the pyramid tool and the tool is milled with a DATRON M7HP CNC milling machine on an aluminium plate of 4×40×60 mm dimensions. The dimensions of a single pyramid are as follows: a square base of 450×450 µm and a height of 300 µm. The total area of pyramids on the plate is 20×32 mm. The process parameters for fabricating pre-structured foils are presented in Table. 3.1. A pre-structured foil is formed by placing two flat PC foils (250 µm in thickness, each) on an anvil and embossing-welding them. As a result, a single pre-structured PC foil of 500 µm in thickness is obtained (Fig. 3.8.).

Table 3.1 The process parameters for fabricating pre-structured PC foils

Process parameter	**The value of a parameter when embossing on PC**
UHE device	HiQ DIALOG 1200 from Herrmann Ultrasonics
Frequency of vibration, kHz	35
Amplitude of vibration, µm	16.3
Force during vibrations, N	650
Duration of vibrations, s	0.5
Holding duration, s	1.5
Force during holding, N	300

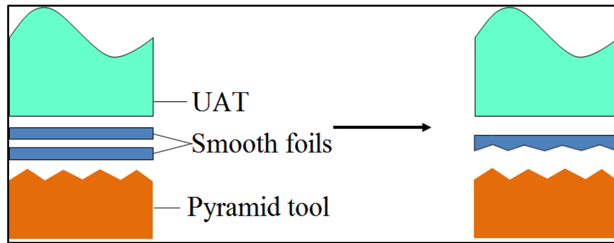

Fig. 3.8. The fabrication of pre-structured polymer foils

3.5.2. An analysis of the sets of appropriate process parameters

The protruding cross tool (Fig. 3.9.) was fabricated to emboss the foils and compare sets of appropriate process parameters.

The purpose of control marks is to facilitate the quality inspection of the embossed foils. The specimen is considered as fully embossed, if all four control marks are detectible. In the case when control marks are not visible, the specimen is regarded as not embossed, i.e. the embossing parameters are not sufficiently high. White patches indicate specimen damage caused by overly high pressure or inadequate processing duration (Fig. 3.10.).

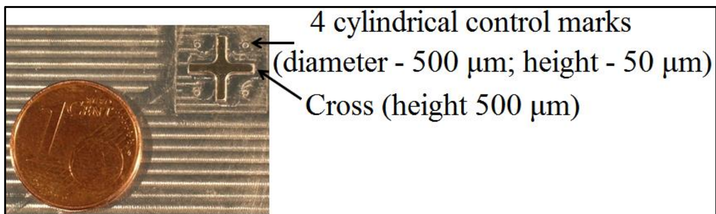

Fig. 3.9. The protruding tool

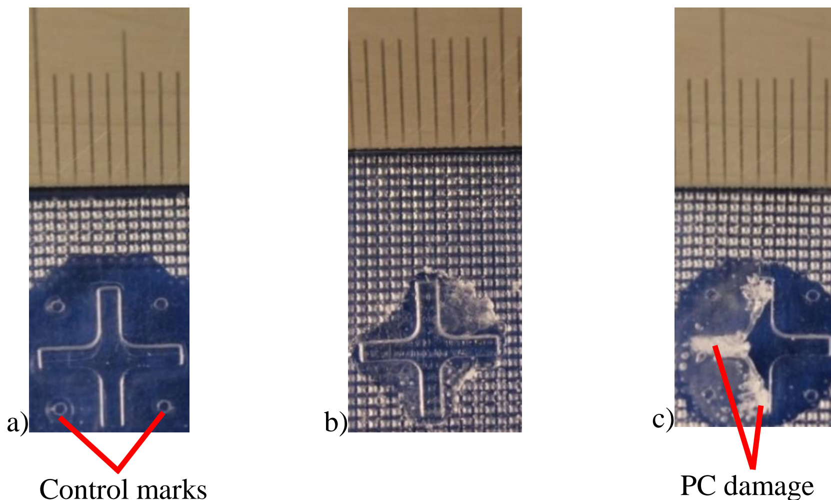

Fig. 3.10. Specimens embossed on the PC: a successfully embossed specimen (a), an insufficiently embossed specimen (b) and polymer damage (c)

The force and duration of embossing are altered during the experiments, as it is necessary to determine the parameters which produce fully or insufficiently embossed structures. All other parameters of the process are maintained constant; they are presented in Table. 3.2.

Table 3.2 Process parameters for finding sets of appropriate process parameters

Process parameter	The value of a parameter when embossing on PC
UHE device	HiQ DIALOG 1200 from Herrmann Ultrasonics
Frequency of vibration, kHz	35
Amplitude of vibration, µm	16.3
Force during vibrations, N	Varied
Duration of vibrations, s	Varied
Holding duration, s	1.5
Force during holding, N	300
Tool temperature, °C	30

As Table 3.2 shows, the vibration amplitude is constant during the experiments (16.3 µm). The energy is force integral along the displacement, therefore, higher force transfers more energy. The ultrasonic energy is directly proportional to the force and duration of ultrasonic excitation. Therefore, an increase in force reduces the duration of vibrations. The boundaries of the sets of appropriate process parameters must be expressed as lines of invariable energy which is required to soften and decompose the polymer.

The sets of appropriate process parameters of five different foil orientations are provided in Fig. 3.11–3.15. The square denotes an insufficiently embossed specimen, i.e. the process parameters are inadequate. The circle indicates a well-embossed sample with clearly visible control marks and the rhombus signifies a damaged specimen.

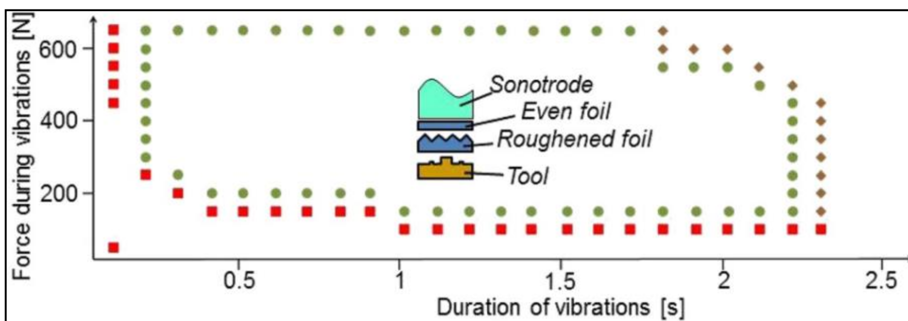

Fig. 3.11. The surface of a pre-structured foil faces a smooth foil on the top

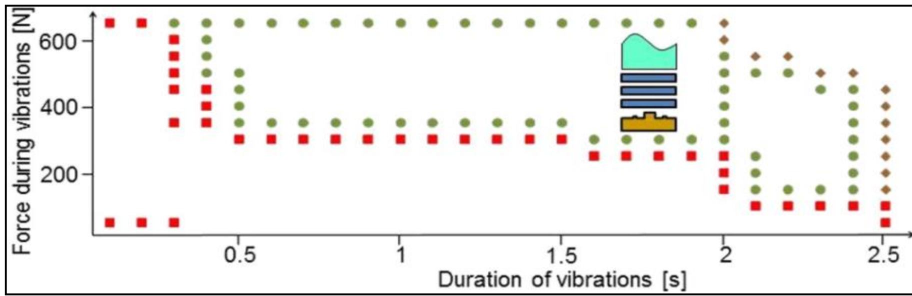

Fig. 3.12. Three smooth foils are embossed

Figures 3.11 and 3.12 demonstrate that additional heat generation in the upper part of the stack enables to fabricate well-embossed microstructures faster and with lower embossing force (0.2 s and 300 N). In addition, this increases the set of appropriate process parameters, i.e. establishes more parameters at which high-quality microstructures are replicated.

Pyramids of pre-structured foil fronting the UAT (Fig. 3.13.) result in a narrower set of appropriate process parameters, when compared to the results seen in Fig. 3.11. This can be described by inessential heat generation between the surface of UAT and the upper wall of the stack. A sufficient amount of heat is generated due to the friction between the UAT and the polymer, therefore, no additional heating is required.

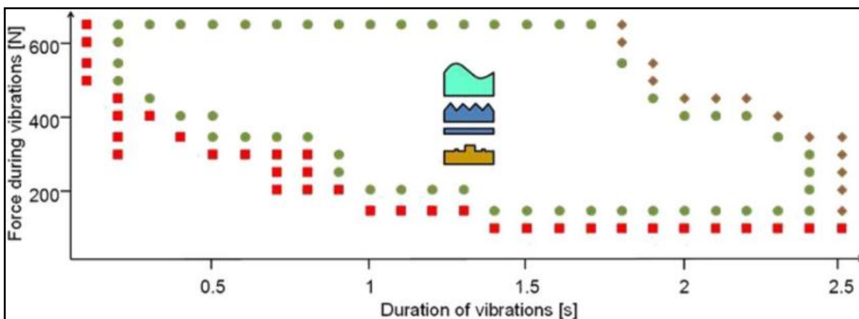

Fig. 3.13. The pre-structured surface of the foil faces the UAT

The set of appropriate process parameters is minimized the most when the pyramids of pre-structured foils are in contact with the tool (Fig. 3.14.). The temporal parameters which are necessary to obtain well-embossed microstructures are the highest (0.4 s and 600 N), while with the shortest process duration (1.2 s and 150 N) the microstructures are damaged. This can be explained by unnecessary additional heat generation in the location which is already characterised by the largest heat generation. Furthermore, the acoustic energy is absorbed at the tool-polymer interface zone and the upper polymer layers are not pre-heated.

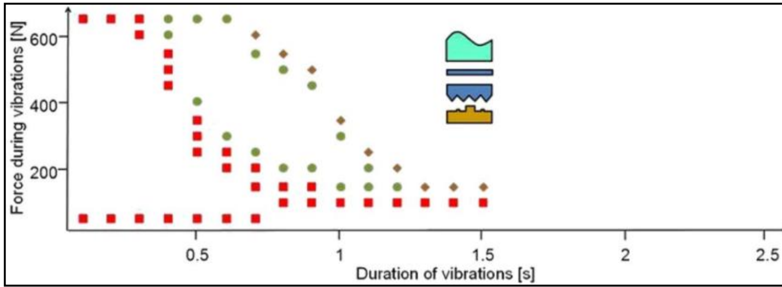

Fig. 3.14. The pre-structured foil surface faces the tool

Pre-structured pyramids facing an even foil placed on the tool (Fig. 3.15.) produce second to lowest temporal parameters (0.3 s and 500 N).

In general, additional heat generation is required in the upper third of the polymer stack (Fig. 3.11.), as it results in the lowest temporal parameters and expands the set of appropriate process parameters.

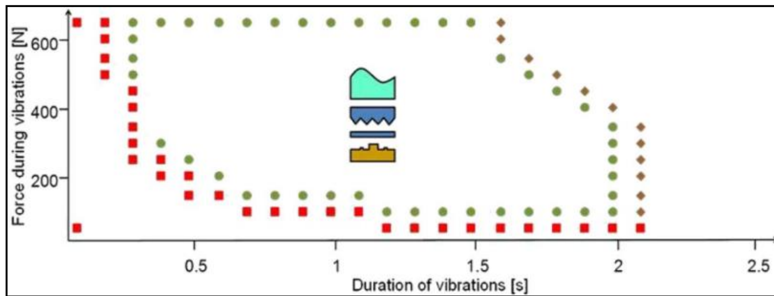

Fig. 3.15. The pre-structured surface faces the even foil located on the tool

The polymer is broken down by the energy and duration of the ultrasound; consequently, the breakdown borders in all cases, except Fig. 3.14, are vertical lines.

The sets of appropriate process parameters can vary slightly with respect to changes in microstructure design and applied materials. However, the deviations should not be significant and the study of embossing precise periodical microstructures can be performed.

3.6. The development of VAPs for thermal imprint assisted by high-frequency vibrations

VAPs are developed and fabricated for the thermal imprint process; they operate on the basis of inverse piezoelectric effect, i.e. converting AC voltage to harmonic mechanical displacements. The purpose of a VAP is to stimulate the flow of pre-heated polymer towards the master microstructure and enhance replicability.

The objective of the VAPs device is to generate uniform vibratory displacements at every point of the top operating surface (Fig. 3.16). The ODS ensures uniform beneficial influence of the high-frequency vibratory excitation throughout the entire surface of the replicated microstructure.

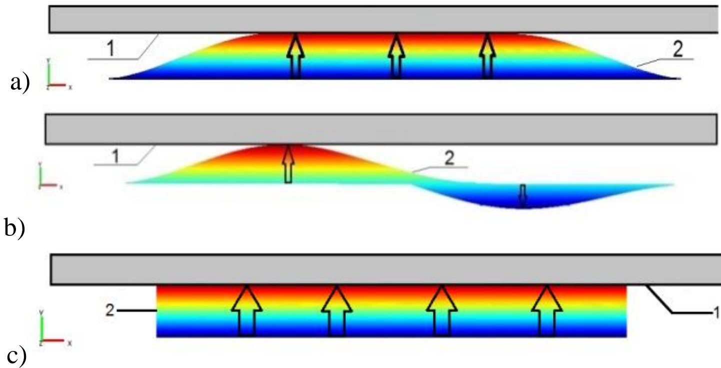

Fig. 3.16. Contact patterns between the VAP (2) and the polymer (1): the first ODS of the membrane (a), the second ODS of the membrane (b) and the ODS when the operating surface is in full contact with the polymer (c)

The operating process regimes required to generate the ODS are determined after a numerical frequency response analysis of unstressed and pre-stressed devices. The frequency response analysis of pre-stressed devices follows a certain order: firstly, the device is analysed statically to determine the displacement corresponding to the applied thermal imprint stress. Then, frequency response analysis of pre-stressed devices is performed. The *Comsol Multiphysics 3.5a* software is applied for FE analysis; the fabrication and experimental analysis are carried out to find the frequencies of the required ODS and to verify the model.

The geometries of both device designs are determined correspondingly to the mandatory restrictions:

- The distance between the anvil and the horn in thermal imprint device is 37 mm, thus the VAP and PC plate 2 mm thick must correspond to this requirement. Moreover, there must be additional space for horn motion.
- The outer diameter of PZT-5 ring is 40 mm and 22 mm for the PZT-4 ring. The outer diameter of the device design must correspond to the diameters of the piezo-ceramic rings to avoid membrane deflection shapes.

The material and geometric aspects of the devices are selected with regards to the conditions of application, i.e. the devices must simultaneously withstand the pressure of 600 kPa and transmit vibrations to the PC sample. According to the initial conditions, two devices are designed: VAP-1 and VAP-2. The design of VAP-1 (Fig. 3.17) contains two stainless steel parts and two PZT-5 piezo-ceramic rings (outer diameter – 40 mm, inner diameter – 32 mm and height – 5 mm) which are fastened with an M5×25 bolt.

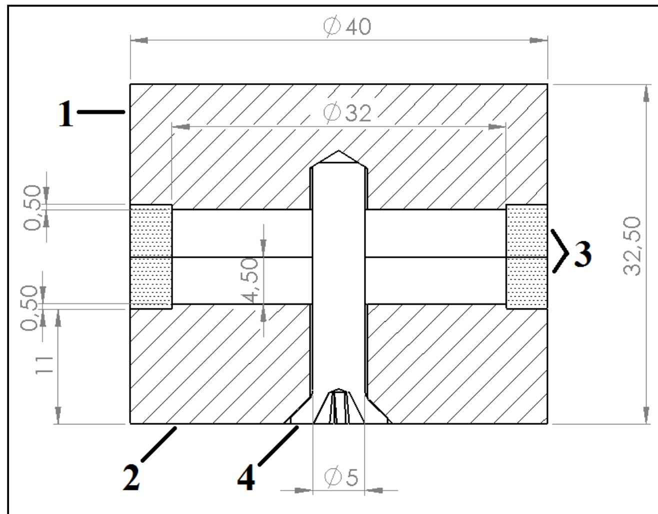

Fig. 3.17. The cross section view of VAP-1: the top (1), the bottom (2), two PZT-5 rings (3) and an M5×25 bolt (4)

The second device design is VAP-2 (Fig. 3.18.); it contains two steel parts and four PZT-4 rings (outer diameter – 22 mm, inner diameter – 10 mm, and height – 5 mm). The device is tightened with a spring (stiffness – 4700 N/m) instead of a bolt, which results in higher displacements and lower operating frequencies because of reduced stiffness. The spring is attached to a bolt (top) and a rod (bottom).

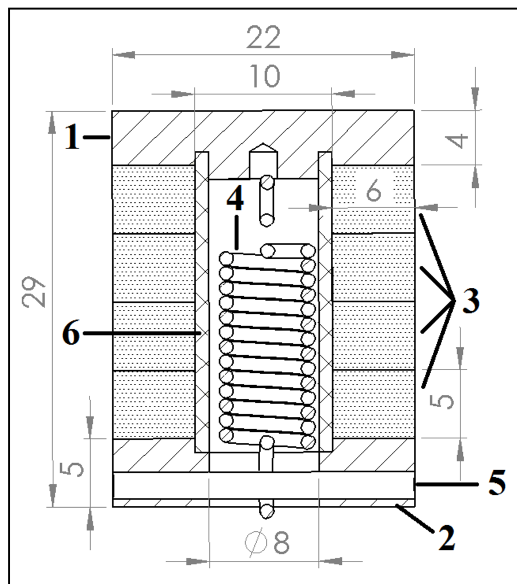

Fig. 3.18. The cross section view of VAP-2: the top (1), the bottom (2), four PZT-4 rings (3), the spring (4), the rod for holding the spring (5) and the plastic tube (6)

The images of both prototypes are provided in Fig. 3.19. The application of several piezo-ceramic rings results in a multilayer effect, i.e. the superposition of layers causes higher amplitudes. The higher amplitude and force increase the velocity of pre-heated polymer flow which leads to increased replicability (Goldfarb and Celanovic 1997).

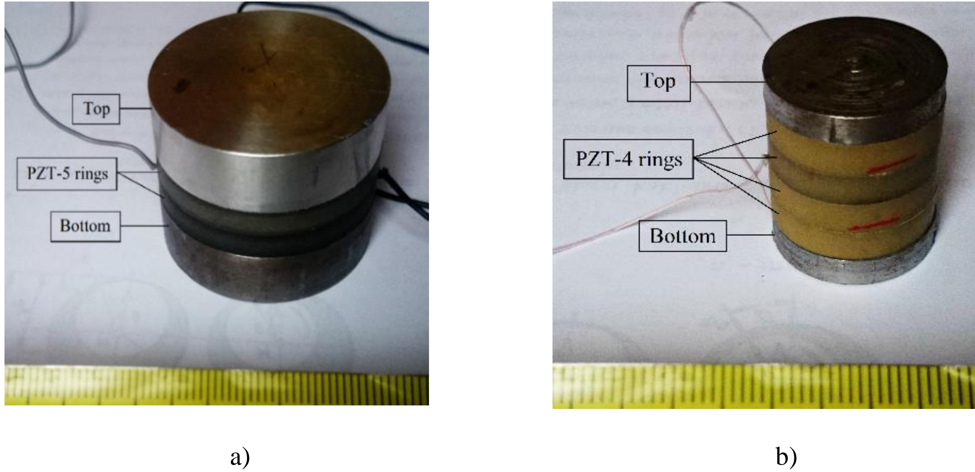

a) b)

Fig. 3.19. Prototypes of VAPs: VAP-1 (a) and VAP-2 (b)

3.6.1. Finite Element model

This chapter presents the FE model for both device designs. The model is 3D, since the aim of numerical frequency response analysis is to determine the frequency at which the operating surface of a VAP vibrates with a uniform displacement field.

Initially, the logarithmic decrement technique is applied to evaluate the damping of devices. The damping ratios of VAPs are determined by performing the bump test and the transient response is obtained. The logarithmic decrement is calculated by using the following formula:

$$\delta = \frac{1}{n}\ln\left(\frac{x(t)}{x(t+nT)}\right), \tag{17}$$

here: $x(t)$ is amplitude at time t and $x(t+nT)$ is amplitude at time after n periods. The damping ratio is calculated with:

$$\zeta = \frac{\delta}{\sqrt{(2\pi)^2 + \delta^2}}, \tag{18}$$

For higher precision, the logarithmic decrement and the damping ratio are calculated for different periods: n= 1, 5, 10, 15, 20. Finally, the results are averaged (see Table 3.3).

Table 3.3 The average logarithmic decrements and damping ratios of the devices

VA device	Average logarithmic decrement	Average damping ratio
VAP-1	0.12	0.02
VAP 2	0.35	0.06

VAP-1 can be described by the following geometric parameters: the height of piezo-ceramic h_{piezo} – 10 mm; the height of the device h_{con} – 32.5 mm and the diameter of VAP-1 – 40 mm. The bottom of the device is immovably fixed in all directions of the global coordinate axis. The actuation voltage between the top and the bottom of PZT-5 varies from 5 to 100 V. High tensile steel 4340 and PZT-5 are used for the metallic part of VAPs and the piezo-ceramic material.

The following assumptions are made in the modelling of VAP-1:

- The bolt, top and bottom parts are made from high tensile steel 4340 and considered as a single element in modelling.
- A single PZT-5 ring (10 mm high) is used instead of two PZT-5 rings.

The boundary conditions of the VAP-2 are: the height of piezo-ceramic h_{piezo} – 20 mm; the height of the device h_{con} – 29 mm; and the diameter – 22 mm. The bottom of the VAP is immovably fixed in all directions of the global coordinate axis. The actuation voltage between the bottom and the top surfaces of the PZT-4 alternates from 5 to 100 V. High tensile steel 4340 and PZT-4 are selected for VAPs metallic and piezo-ceramic parts, respectively.

The following assumptions are made in the modelling of VAP-2:

- High tensile steel 4340 rod (26 μm in diameter) is designed to replace the spring. The stiffness of the rod and the spring are equivalent.
- The spring, top and bottom parts of the VAP are made from high tensile steel 4340 and considered as a single monolithic component.
- A single PZT-4 ring (height – 20 mm) is designed in order to substitute four PZT-4 rings.

The numerical frequency response analysis of pre-stressed devices is performed in order to determine the operating frequencies of the required ODS. The FE model must be adapted to the conditions of the thermal imprint experiment.

The PC plate (20×20 mm large and 2 mm thick h_{pc}) and the master mould of the same dimensions ($h_{m\ mold}$ – 6 mm) stress the device. The master mould is made from structural steel. The properties of the PC and the structural steel are provided in Table 3.4.

Table 3.4 The properties of PC and structural steel

Material properties	PC	Structural steel
Young modulus, Pa	2×10^9	200×10^9
Poisson's ratio	0.37	0.33
Density, kg/m^3	1200	7850

The pressure of pre-stressed devices is defined as displacement U of the upper plane of the master mould with respect to the applied pressure (100–500 kPa). The displacement U, which is a response to pressure, is determined by performing a numerical static analysis, which is then followed by the numerical frequency response analysis of pre-stressed devices.

2D images of unstressed and pre-stressed devices with their corresponding boundary conditions are provided in Figs. 3.20 and 3.21. The device designs are meshed with quadratic tetrahedral finite elements. Every element has ten nodes and four dependent variables (the electric potential Q and displacements in u,v and w directions).

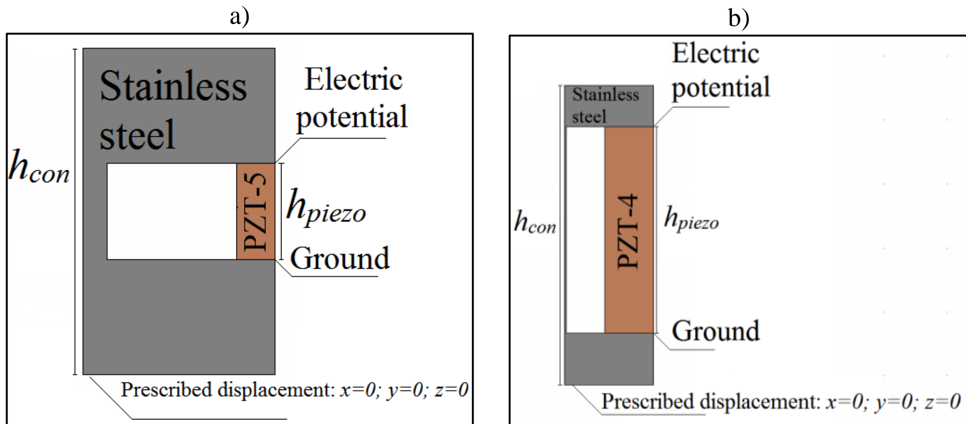

Fig. 3.20. Computational schemes with boundary conditions of unstressed VAP-1 (a) and VAP-2 (b)

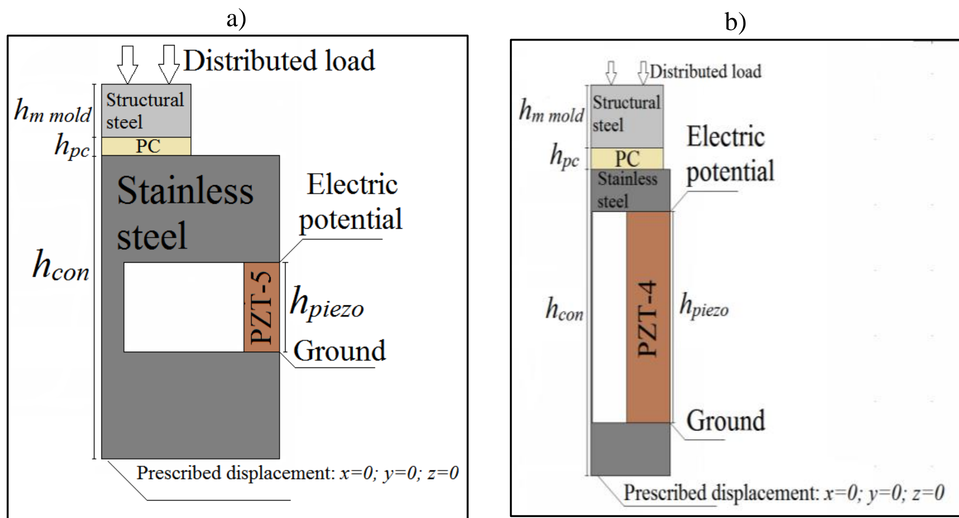

Fig. 3.21. Computational schemes with boundary conditions of pre-stressed VAP-1 (a) and VAP-2 (b)

Constitutive equations

The material parameters of the piezoelectric constituents of devices are selected as a stress–charge form for the constitutive equation.

The material parameters for both of the piezoelectric materials (PZT-4 and PZT-5) are characterized by the elasticity matrix– c_e, the coupling matrix– e and the relative permittivity matrix– ε_{rs}. The polarization of piezo-ceramic elements is considered to be in y direction, i.e. corresponding to real conditions.

The elasticity matrix characterizes the stress applied to the material and its strain response. The stress–strain relationship throughout the elasticity matrix is expressed as follows:

$$\sigma = c_e \varepsilon , \tag{19}$$

here: σ – stress, ε – strain and c_e – the elasticity matrix.

The elasticity matrix of PZT-5 has the following expression:

$$c_E = \begin{bmatrix} 1.20346e11 & 7.51791e10 & 7.50901e10 & 0 & 0 & 0 \\ 7.51791e10 & 1.20346e10 & 7.50901e10 & 0 & 0 & 0 \\ 7.50901e10 & 7.50901e10 & 1.10867e11 & 0 & 0 & 0 \\ 0 & 0 & 0 & 2.10526e10 & 0 & 0 \\ 0 & 0 & 0 & 0 & 2.10526e10 & 0 \\ 0 & 0 & 0 & 0 & 0 & 2.25734e10 \end{bmatrix}$$

The elasticity matrix of PZT-4 is expressed as follows:

$$c_E = \begin{bmatrix} 1.38999e11 & 7.78366e10 & 7.42836e10 & 0 & 0 & 0 \\ 7.78366e10 & 1.38999e10 & 7.42836e10 & 0 & 0 & 0 \\ 7.42836e10 & 7.42836e10 & 1.15412e10 & 0 & 0 & 0 \\ 0 & 0 & 0 & 2.5641e10 & 0 & 0 \\ 0 & 0 & 0 & 0 & 2.5641e10 & 0 \\ 0 & 0 & 0 & 0 & 0 & 3.0581e10 \end{bmatrix}$$

The coupling matrix. The piezo-coupling matrix, denoted by e, is applied in the stress–charge relationship:

$$\sigma = c_E \varepsilon - e^T E , \tag{20}$$

here: σ – stress, ε – strain and E – the electric field.
The coupling matrix of PZT-5 is expressed as:

$$e = \begin{bmatrix} 0 & 0 & 0 & 0 & 12.2947 & 0 \\ 0 & 0 & 0 & 12.2947 & 0 & 0 \\ -5.35116 & -5.35116 & 15.7835 & 0 & 0 & 0 \end{bmatrix}$$

The coupling matrix of PZT-4 is expressed as follows:

$$e = \begin{bmatrix} 0 & 0 & 0 & 0 & 12.7179 & 0 \\ 0 & 0 & 0 & 12.7179 & 0 & 0 \\ -5.20279 & -5.20279 & 15.0804 & 0 & 0 & 0 \end{bmatrix}$$

The relative permittivity matrix ε_{rS} is applied in the constitutive relation of stress–charge and strain–charge forms:

$$D = e\varepsilon + \varepsilon_0 \varepsilon_{rS} E \, , \tag{21}$$

The relative permittivity matrix of PZT-5 can be represented with:

$$\varepsilon_{rS} = \begin{vmatrix} 919.1 & 0 & 0 \\ 0 & 919.1 & 0 \\ 0 & 0 & 826.6 \end{vmatrix}$$

The relative permittivity matrix of PZT-4 is expressed with:

$$\varepsilon_{rS} = \begin{vmatrix} 762.5 & 0 & 0 \\ 0 & 762.5 & 0 \\ 0 & 0 & 663.2 \end{vmatrix}$$

The piezoelectric equations are written in the forms of nodal displacement $\{U\}$ and nodal electrical potential $\{\phi\}$. The force F for unstressed devices is equal to zero, and the nodal electric loads are expressed by $\{Q\}$:

$$\begin{bmatrix} [M_{UU}] & 0 \\ 0 & 0 \end{bmatrix} \begin{Bmatrix} \{\ddot{U}\} \\ \{\ddot{\phi}\} \end{Bmatrix} + \begin{bmatrix} [C_{UU}] & 0 \\ 0 & 0 \end{bmatrix} \begin{Bmatrix} \{\dot{U}\} \\ \{\dot{\phi}\} \end{Bmatrix} + \begin{bmatrix} [K_{uu}] & [K_{u\phi}] \\ [K_{u\phi}] & [K_{\phi\phi}] \end{bmatrix} \begin{Bmatrix} \{U\} \\ \{\phi\} \end{Bmatrix} = \begin{Bmatrix} \{0\} \\ \{Q\} \end{Bmatrix}, \tag{22}$$

$$[K_{UU}] = \iiint_{\Omega e} [B_U]^T [c][B_U] dV \, , \tag{23}$$

$$[K_{U\phi}] = \iiint_{\Omega e} [B_U]^T [e][B_U] dV \, , \tag{24}$$

$$[K_{\phi\phi}] = \iiint_{\Omega e} [B_\phi]^T [\varepsilon][B_\phi] dV \, , \tag{25}$$

$$[M_{UU}] = \rho \iiint_{\Omega e} [N_U]^T [N_U] dV \, , \tag{26}$$

$$[C_{UU}] = \beta [K_{UU}], \tag{27}$$

here: $[K_{UU}]$ – mechanical stiffness matrix, $\lfloor K_{U\phi} \rfloor$ – piezoelectric coupling matrix, $\lfloor K_{\phi\phi} \rfloor$ – dielectric stiffness matrix, $[M_{UU}]$ – mass matrix, ρ – piezoelectric density, $[N_U]$ – matrix of elemental shape functions, $[C_{UU}]$ – mechanical damping matrix, $[B_U]$ and $\lfloor B_\phi \rfloor$ – derivatives of FE model shape functions, $[c]$ – elastic coefficients, $[e]$ – piezoelectric coefficients, $[\varepsilon]$ – dielectric coefficients, β – damping coefficient. The VAP is excited with a harmonic voltage signal and the electrical potential is expressed as follows:

$$Q = A \sin \omega, \tag{28}$$

here: A – amplitude and ω – angular frequency.
The simulated dynamic behaviour of a VAP is provided in terms of point displacement. The frequency response problem for the unstressed device is solved to obtain these vibration responses:

$$\begin{bmatrix} K_{UU} - \varpi C_{UU} - \varpi^2 M_{UU} & K_{U\phi} \\ K_{\phi U} & K_{\phi\phi} \end{bmatrix} \begin{Bmatrix} \{U\} \\ \{\phi\} \end{Bmatrix} = \begin{Bmatrix} \{0\} \\ \{Q\} \end{Bmatrix}, \tag{29}$$

The displacement of a pre-stressed device corresponding to the applied pressure is determined according to the formula:

$$[K_{UU}]\{U\} = \{F\}, \tag{30}$$

Consequently, the pre-stressed frequency response analysis is performed by modifying equation (29), i.e. displacement is added:

$$\begin{bmatrix} K_{UU} - \varpi C_{UU} - \varpi^2 M_{UU} & K_{U\phi} \\ K_{\phi U} & K_{\phi\phi} \end{bmatrix} \begin{Bmatrix} \{U\} \\ \{\phi\} \end{Bmatrix} = \begin{Bmatrix} \{F(U_0)\} \\ \{Q\} \end{Bmatrix}, \tag{31}$$

3.6.2. Validation of the FE model

The analysis of the unstressed VAP-1

The FE model is verified by comparing the simulated and experimentally obtained operating frequencies. Firstly, y-directional numerical frequency response curves of the centre and four edge points of both unstressed devices (Fig. 3.22) are obtained.

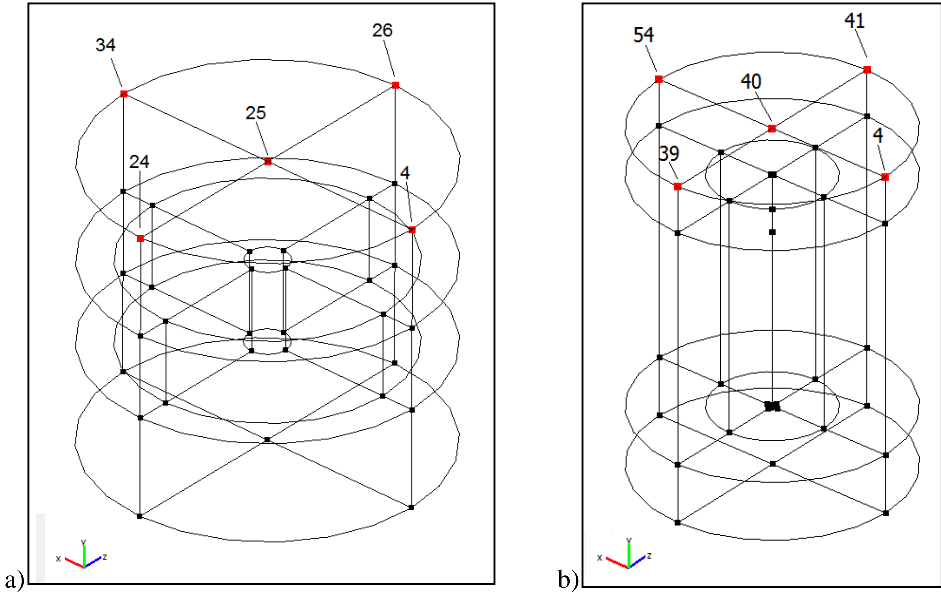

Fig. 3.22. The points analysed during numerical frequency response analysis of unstressed devices VAP-1 (a) and VAP-2 (b)

The numerically simulated frequency response curves registered at points 4, 24, 25, 26 and 34 and the displacement field of VAP-1 are provided in Fig. 3.23. The main focus is to detect the frequency at which the peaks of frequency response curves coincide. Mutual peaks indicate ODS with uniform displacements throughout the analysed points.

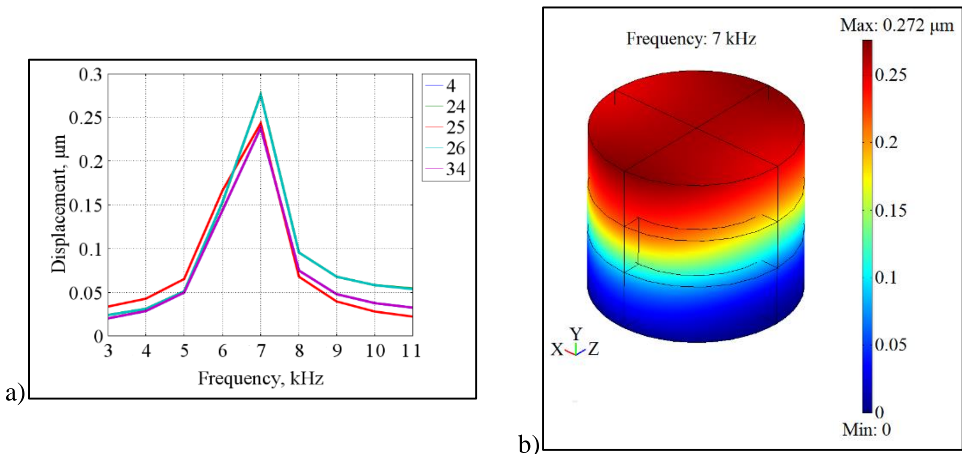

Fig. 3.23. Numerically simulated frequency response curves (a) and the visualization of the simulated displacement field (b) of the unstressed VAP-1

The frequency response plot in Fig. 3.23 (a) indicates that the unstressed VAP-1 vibrates with uniform amplitudes throughout the operating surface at the excitation frequency of 7 kHz. Displacement values at the analysed points range from 0.242 to 0.272 μm. The visualization of the displacement field (Fig. 3.23. (b)) confirms the uniformity of amplitudes, i.e. the operating surface is of homogenous colour.

Experimental ODS analysis is carried out with the holographic interferometry system PRISM. White regions are considered as nodal lines, i.e. zero displacements, while the black areas are considered as vibrating zones. To compare the results, the vibration responses are observed at different frequencies (Fig. 3.24). The holographic aspect where the entire surface is black is considered to be the required ODS (Fig. 3.24 (b)).The following step is frequency response analysis by applying LDV. Three characteristic points of the unstressed VAP-1 are analysed: the midpoint, 1 and 2 cm from the midpoint of the device. The results are presented in frequency response plots (Fig. 3.25).

Fig. 3.24. ODS analysis of VAP-1: the frequency of 30.98 kHz (a) and 7.5 kHz (b)

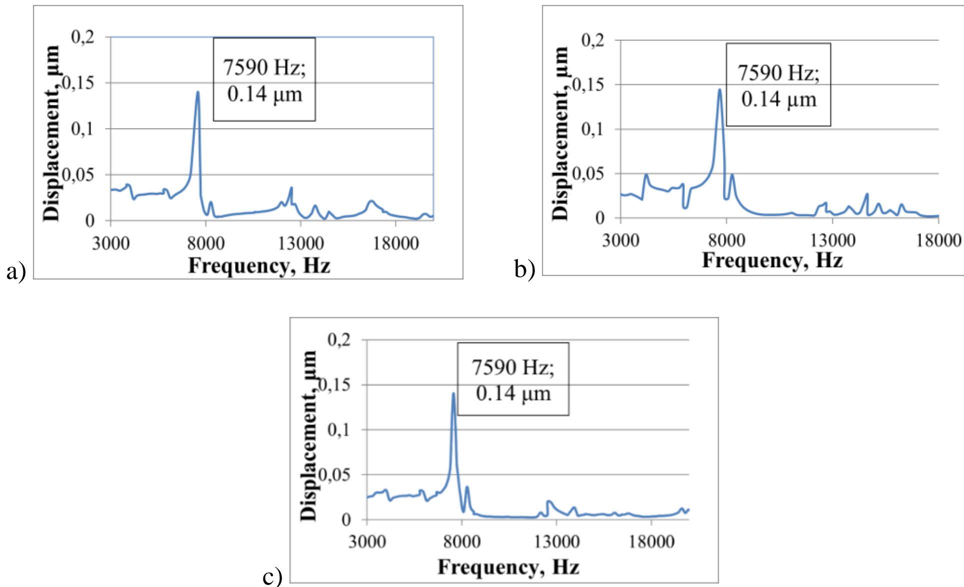

Fig. 3.25. Frequency response plots of VAP-1: 2 cm (a), 1 cm from centre (b) and at the centre (c)

Dynamic behaviour demonstrates that VAP-1 vibrates with a uniform amplitude along the operating surface at the excitation frequency of 7.5 kHz. The frequency response to harmonic excitation study demonstrates that mutual amplitude peaks of 0.14 μm are obtained at the excitation frequency of 7.59 kHz.

The analysis of the unstressed VAP-2

Numerically simulated frequency response curves of the unstressed VAP-2 obtained at points 4, 39, 40, 41 and 54 and the displacement field visualization are provided in Fig. 3.26.

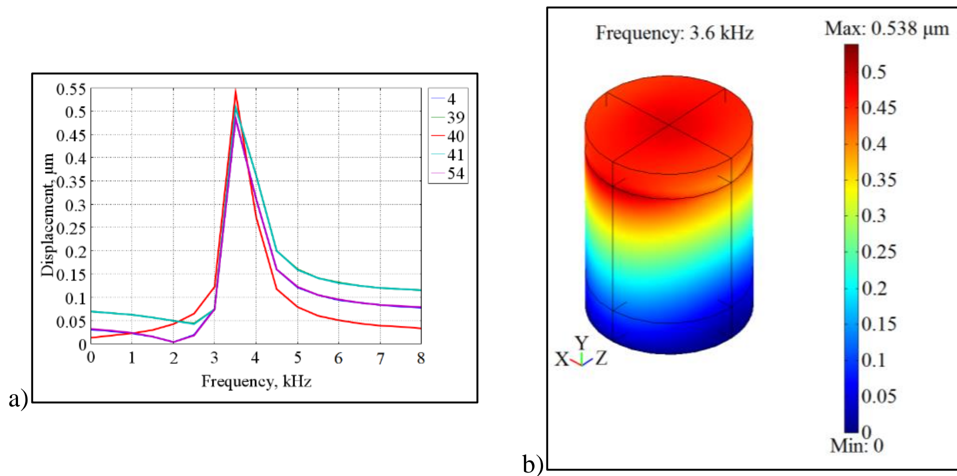

Fig. 3.26. Numerically simulated frequency response curves (a) and the visualization of the simulated displacement field (b) of the unstressed VAP-2

The numerical frequency response analysis of VAP-2 specifies the mutual peaks (Fig. 3.26. (a)) at the excitation frequency of 3.6 kHz. Displacement values at the analysed points fluctuate from 0.497 to 0.538 μm. The visualization of the displacement field (Fig. 3.26. (b)) validates the uniformity of amplitudes.

The results of experimental ODS analysis performed with the PRISM system are presented in Fig. 3.27.

Fig. 3.27. ODS analysis of VAP-2: frequency of 17.750 kHz (a) and 3.1 kHz (b)

The vibration response at the excitation frequency of 3.1 kHz indicates that the device generates a uniform displacement field throughout the operating surface.

Three characteristic points are selected for frequency response analysis with LDV: the midpoint, 0.5 cm and 1 cm from the midpoint of the device. Frequency response plots of the unstressed device are presented in Fig. 3.28. The vibration response validates that the analysed points vibrate with uniform displacement (0.61 µm) at the excitation frequency of 3.15 kHz.

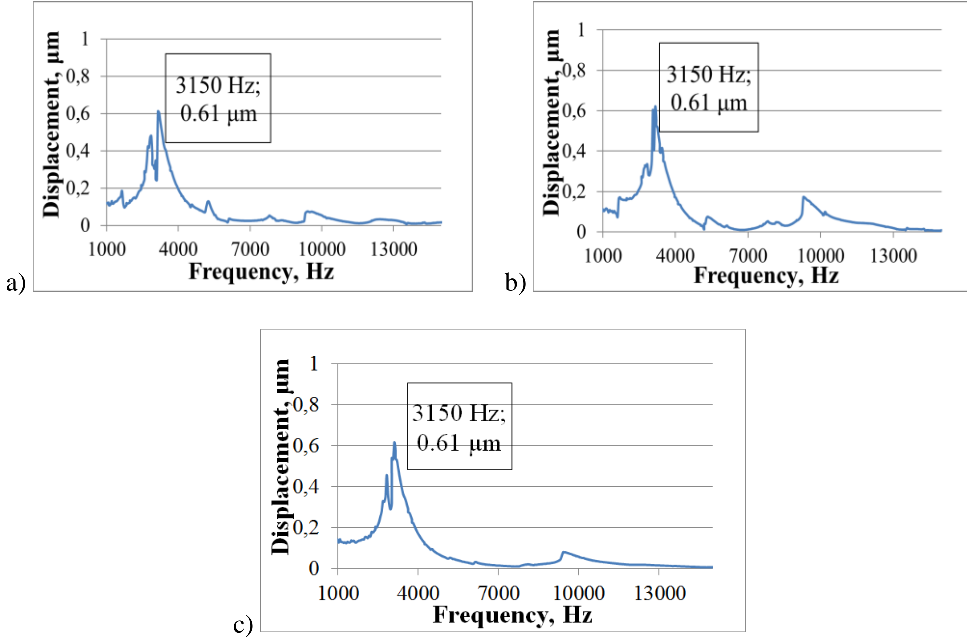

Fig. 3.28. Frequency response plots of VAP-2: 1 cm (a) and 0.5 cm from centre (b), and at the centre (c)

FE model is validated by comparing the numerical and experimental excitation frequency values which are required to obtain uniform displacement fields. The operating frequency differences between the achieved results are provided in Table 3.5.

Table 3.5 Differences between experimental and numerically obtained operating frequencies of unstressed devices

VAP-1	VAP-2	Average
6.7 %	16.1 %	11.4 %

The highest divergence between the numerically obtained and experimental frequencies is 16.1 %.

3.6.3. A study of pre-stressed devices

The pre-stressed devices are studied to determine the operating regimes of the required ODS.

Numerical frequency response analysis of pre-stressed devices

The original FE model is adapted by adding displacement which corresponds to the applied pressure to investigate the contact points of VAPs and the PC plate (Fig. 3.29.). Frequency response curves of pre-stressed devices are presented in Fig. 3.30.

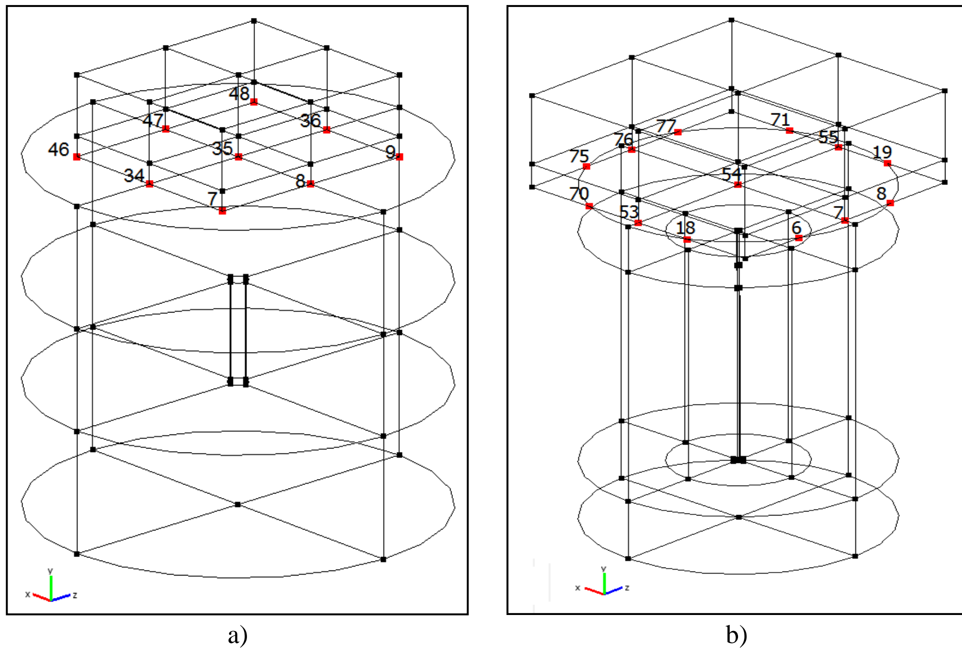

a) b)

Fig. 3.29. Points analysed during the numerical frequency response analysis of pre-stressed devices: VAP-1 (a) and VAP-2 (b)

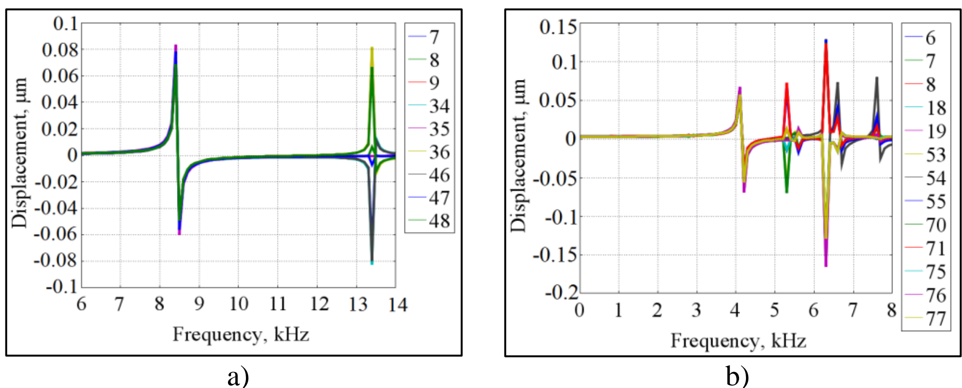

a) b)

Fig. 3.30. Numerically simulated frequency response curves of pre-stressed devices: VAP-1 (a) and VAP-2 (b)

The numerically simulated frequency response plot of a pre-stressed VAP-1 demonstrates a uniform displacement field registered at the excitation frequency of 8.35 kHz. The corresponding ODS of VAP-2 is observed at the excitation frequency of 4.1 kHz. The numerical frequency response analysis validates that pre-stressed devices generate the required ODS.

Experimental frequency response analysis of pre-stressed devices

Experimental frequency response analysis of pre-stressed devices is performed with a self-made setup (Fig. 3.31) which contains a VAP, an LDV, a dynamometer and a clamp. The clamp pre-stresses the device according to the conditions of thermal imprint. The universal dynamometer BGI with an attached SSM-series compression/tension sensor is used to measure the pressure. The vibration responses of pre-stressed devices are registered with the LDV.

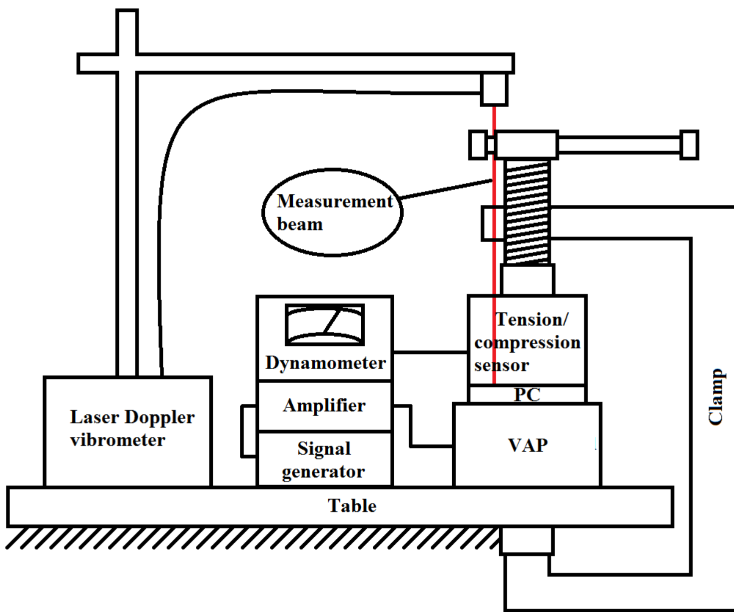

Fig. 3.31. The setup for frequency response analysis of a pre-stressed VAP

The frequency response of pre-stressed devices is analysed at 0.5 and 1 cm from the midpoint (Fig. 3.32). The midpoints are covered with the clamp, the PC plate and the dynamometer. The results of vibration response analysis of the pre-stressed (100 to 500 kPa) devices are presented in Figs. 3.33.–3.34.

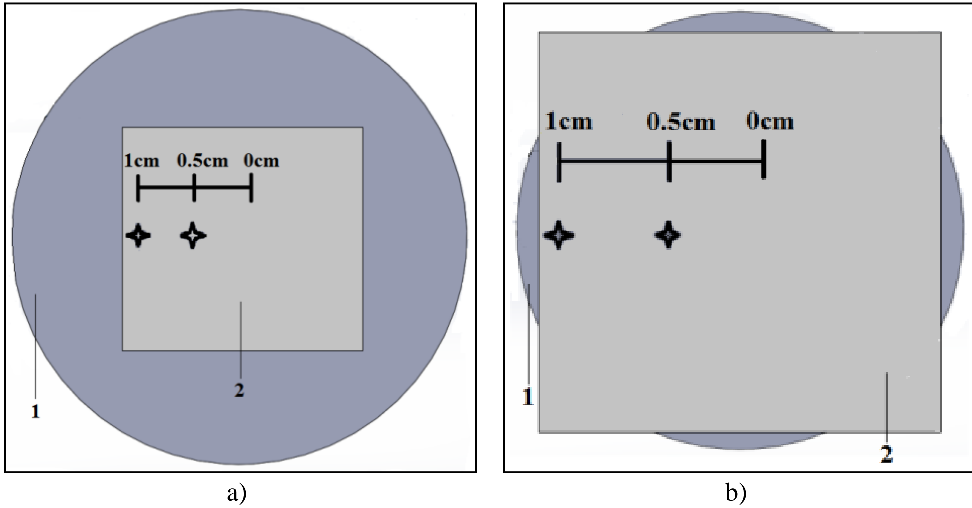

a) b)

Fig. 3.32. Points of pre-stressed VAP-1 (a) and VAP-2 (b) analysed with the LDV: VAP (1) and the applied pressure (2)

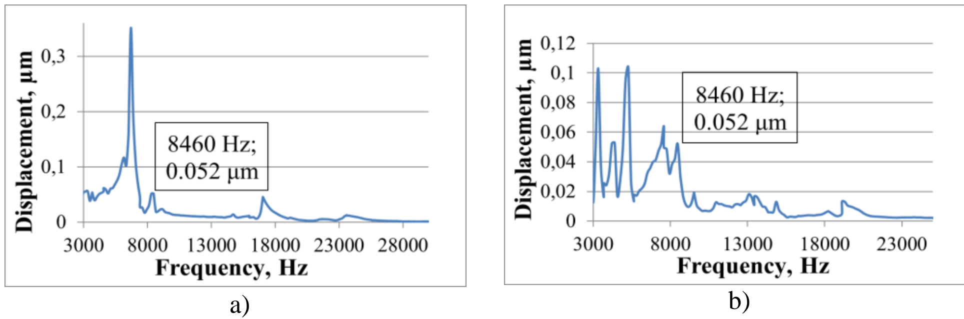

a) b)

Fig. 3.33. Frequency response plots of the pre-stressed VAP-1: 1 cm (a) and 0.5 cm from the midpoint (b)

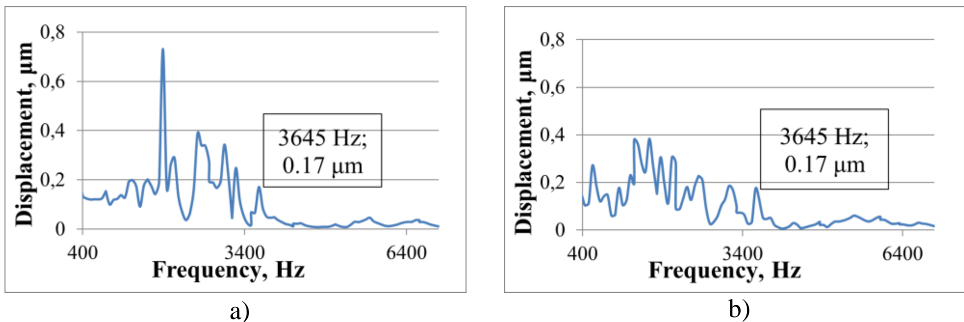

a) b)

Fig. 3.34. Frequency response plots of the pre-stressed VAP-2: 1 cm (a) and 0.5 cm from the midpoint (b)

The pre-stressed VAP-1 vibrates with the amplitude of 0.052 µm at the excitation frequency of 8.46 kHz, while VAP-2 vibrates with the amplitude of 0.17

μm at the excitation frequency of 3.645 kHz. The pre-stressed devices generate the required ODS at higher excitation frequency than the unstressed device.

The numerical and experimental operating frequencies are compared in order to validate the FE model. Frequency divergences between the numerical and experimental results are presented in Table 3.6.

Table 3.6. Differences between the experimental and numerically obtained operating frequencies of pre-stressed devices

VAP-1	VAP-2	Average
1.3 %	12.5 %	6.9 %

The highest divergence between the numerical and experimental operating frequencies is 12.5 %. The results of this research show that pre-stressed VAPs exhibit lower divergence of the operating frequency than the unstressed devices. Pre-stressing the device increases its stiffness and decreases the adverse oscillations which, in turn, leads to lower discrepancy. Pre-stressed devices generate uniform displacement fields (required ODS) throughout the operating surface at appropriate operating frequencies.

3.6.4. An investigation of lateral displacements

The study also investigates the vibrational responses of the lateral amplitudes obtained at the operating excitation frequencies of pre-stressed VAPs. The aim of the research is to determine the correspondence between the magnitude of lateral vibration amplitudes and the quality of the replicated microstructure. The upper surface of the devices is scanned with the LDV, and the analysed points are presented in Fig. 3.35. The results of frequency response analysis are presented in Fig. 3.36. and Table 3.7.

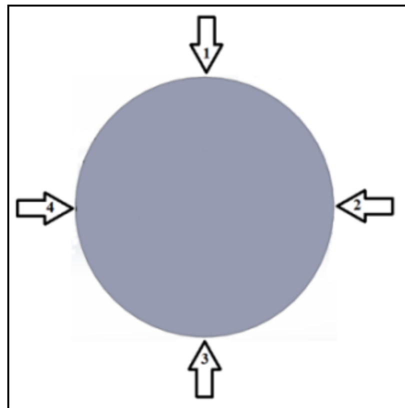

Fig. 3.35. The analysed lateral points of device designs

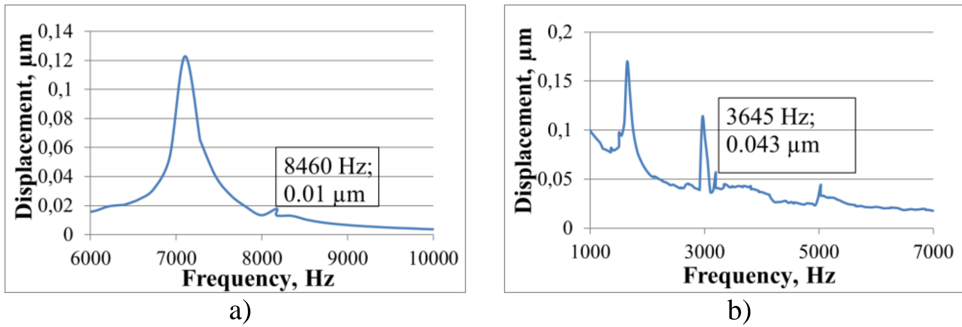

Fig. 3.36. Frequency response plots obtained at first lateral point of VAP-1 (a) and first lateral point of VAP-2 (b)

Table 3.7. Frequency response results obtained at points 2, 3, and 4 of the vibrating pre-stressed devices

Design of VAP	Point	Vibration frequency, kHz	Displacement (µm)
VAP-1	2	8.46	0.011
VAP-1	3	8.46	0.0105
VAP-1	4	8.46	0.0104
VAP-2	2	3.645	0.024
VAP-2	3	3.645	0.018
VAP-2	4	3.645	0.022

The mean values of lateral displacements are 0.0105 µm for VAP-1 and 0.026 µm for VAP-2. Higher lateral amplitudes of this VAP are obtained due to the presence of a spring in the device design. It decreases the stiffness, which results in larger amplitudes and lower operating frequencies.

3.7. Conclusions of the chapter

The first part of the chapter discusses the design of a topologically complex master microstructure by applying CGH. EBL is used for the fabrication of CGH, and the microstructure is hardened with UV light and electroplated with nickel.

Moreover, the chapter describes the improvement of the UHE process. Research demonstrates that beneficial exploitation of additional heat generation through the application of pre-structured foil enables to modify the set of appropriate process parameters, emboss microstructure faster and with a reduced embossing force as well as enhance the quality of the replica.

Finally, the chapter explains the research and development of VAPs for the process of thermal imprint. The aim is to fabricate devices which vibrate with uniform displacement fields over the operating surface. The frequency response is first analysed numerically in order to determine the operating excitation frequencies of the required ODS. Then, the experimental analysis is executed to validate the numerical results. The following statements conclude the chapter:

- Dividing the pixels into portions eliminates their overlapping, rounded corners, and increases RDE of the hologram from 29 to 58 %.

- The metallised CGH demonstrates the highest RDE (24 %) when it is illuminated with a wavelength of 632.8 nm (red laser light). The wavelengths of 441.6 nm (blue laser light) and 532 nm (green laser light) produce lower results: 16 and 15 %, respectively.
- Hardening with a UV light and the metallisation of CGH decrease the RDE from 58 to 24 %.
- Generating additional heat in the upper second third portion of the stack decreases the UHE process parameters (duration of vibrations – 0.2 s and embossing force – 300 N) required to emboss the microstructure, and increases the set of appropriate process parameters.
- VAPs which vibrate with uniform displacement fields have been developed and their operating frequencies have been determined. Pre-stressing the VAP-1 increases the operating frequency from 7.59 to 8.46 kHz. The operating frequency of VAP-2 inclines from 3.15 to 3.65 kHz, as a response to the applied pressure.

4. EXPERIMENTS OF MICROSTRUCTURE REPLICATION

This chapter of the dissertation discusses the experiments of microstructure replication applying UHE and the technology of thermal imprint assisted by high-frequency vibratory excitation. The aim is to determine the relationship between the process parameters and the quality of the replicated microstructure. The establishment of these relationships enables to improve the process results.

4.1. UHE of periodic microstructures

The replication of periodic microstructures is performed after determining sets of appropriate process parameters. The aim of this experiment is to determine how the diffraction efficiency of the embossed DOE depends on the additional heat generation through pre-structured foils.

A nickel master microstructure (Fig. 4.1) is applied in UHE process. The nominal dimensions of the master microstructure are as follows: period – 4 µm and depth – 603.7 nm. A theoretically ideal microstructure is modelled with *GSolver* software, in order to identify the target value of RDE. The modelling has revealed that the theoretically ideal RDE of +1 and –1 maximum is 38.95 %.

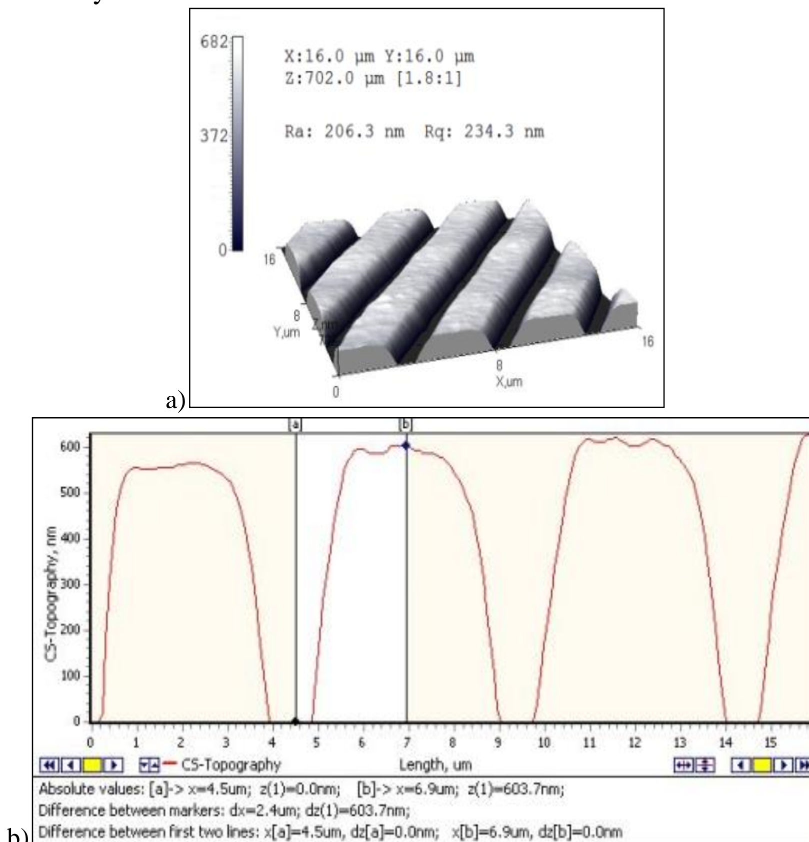

Fig. 4.1. AFM image of the master microstructure: 3D (a) and profile view (b)

The embossed specimens are divided into six sample groups (Table. 4.1.) according to the foil orientation. The first five groups correspond to five different pre-structured foil orientations, while the sixth group represents the experiments with a 2 mm thick PC plate.

The RDE of samples are averaged within the sample groups and statistically analysed with *SPSS 13.0.* software. Independent specimen t-test with the confidence interval of 95 % is applied in calculation and the statistical results are provided in Fig. 4.2.

Table 4.1 Sample groups

Group	**1**	**2**	**3**	**4**	**5**	**6**
Foil orientation						

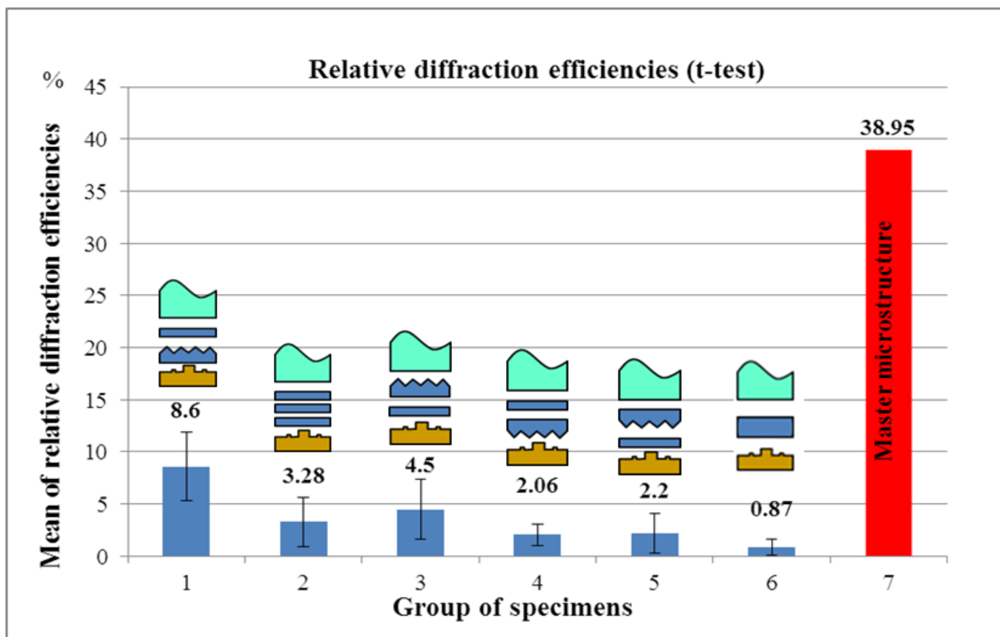

Fig. 4.2. The statistical t-test of RDE with 95 % confidence interval

The first and the third sample groups demonstrate the highest average RDE: 8.6 and 4.5 %, correspondingly. The lowest result (0.87 %) is observed in the sixth specimen group. This can be explained by the fact that the PC plate is overly thick and an insufficient amount of ultrasonic energy reaches the tool.

The results obtained from this experiment are 4.52 times lower than the theoretically ideal value, which suggests that further quality improvement is

necessary. The process of thermal imprint assisted by high-frequency vibratory excitation is selected as the alternative for the experiment.

4.2. Experiments with thermal imprint

The thermal imprinting experiments (Fig. 4.3.) analyse how the quality of the replicated microstructures is influenced by the following parameters: the magnitude of lateral vibration amplitudes, the temperature, the imprinting pressure and the character of the waveform.

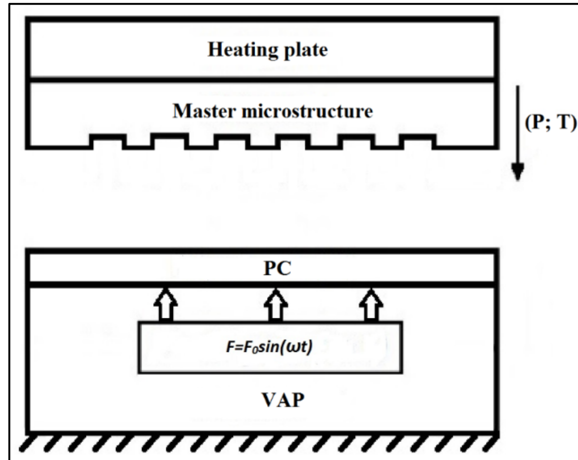

Fig. 4.3. Thermal imprint assisted by high-frequency vibratory excitation

The experiments apply high-frequency vibratory excitations with sine and ramp waveforms. Time acceleration function of vibratory excitation with sine waves is expressed as follows:

$$a(t) = -a\omega^2 \sin \omega t\,, \tag{32}$$

The ramp waveform is a superposition of several sine waves characterized by different frequencies. The time acceleration function of this waveform attains the following expression:

$$a(t) = -a_1\omega^2 \sin \omega t - 4a_2\omega^2 \sin 2\omega t - 9a_3\omega^2 \sin 3\omega t ... - n^2 a_n \sin n\omega t\,, \tag{33}$$

here: a, a_1, a_2 and a_3 – coefficients of acceleration, t – time, and ω – angular frequency.

The ramp waveform generates higher acceleration; therefore it is possible to achieve higher force which stimulates the pre-heated polymer to flow. The experimental matrix of thermal imprint experiments is composed and the data can be seen in Table. 4.2.

Table 4.2 The experimental matrix of thermal imprint

Design of VAP and type of waveform (frequency of vibrations, kHz)	Pressure, kPa	Temperature, ˚C	Duration of imprint, s
Without vibrations	100	148	10
VAP-1 sine waveform (8.46)	200	152	
VAP-2 sine waveform (3.645)	300		
VAP-1 ramp waveform (8.46)	400		
VAP-2 ramp waveform (3.645)	500		

The master microstructure of the following geometrical parameters is applied in the experiments: period – 4 μm and depth – 603.7 nm. The replicated samples are grouped according to the heating temperature, VAP design and the type of waveform used in the experiments. Separate groups include specimens fabricated applying different pressure values (100 to 500 kPa). Grouping of the samples enables to determine the influence of pressure on the mean RDE. The sample groups are provided in Table 4.3.

Table 4.3 The groups of samples

Group	VAP and waveform	Imprint temperature, ˚C
1	Without vibrations	148
2	Without vibrations	152
3	VAP-1 (sine waveform)	148
4	VAP-1 (sine waveform)	152
5	VAP-2 (sine waveform)	148
6	VAP-2 (sine waveform)	152
7	VAP-1 (ramp waveform)	148
8	VAP-1 (ramp waveform)	152
9	VAP-2 (ramp waveform)	148
10	VAP-2 (ramp waveform)	152

4.2.1. Results

The RDE of the samples is measured, and the quality of the replicated microstructures is investigated in terms of mean RDE in +1 and –1 maxima and the profile depth. Subsequently, the obtained RDE values are averaged within separate sample groups and analysed statistically using *SPSS 13.0.* software in the independent specimen t-test mode. The chart of statistical results is presented in Fig. 4.4; it characterizes the mean RDE of discrete groups with the confidence interval of 95 %.

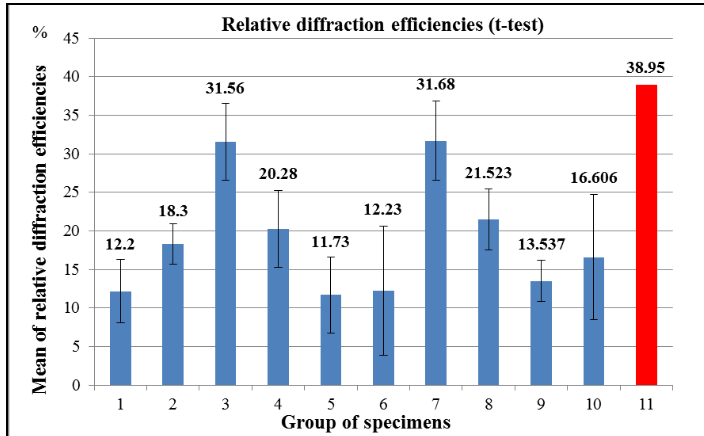

Fig. 4.4. The statistical t-test of mean RDE with 95 % confidence interval of the specimen groups replicated by using the thermal imprint process

Replication without the assistance of high-frequency vibratory excitation produces the average RDE of 12.2 % (imprint temperature – 148 ˚C) and 18.3 % (imprint temperature – 152 ˚C).

Sample group No.3 exhibits the mean RDE of 31.56 %. Groups No.4, No.5 and No.6 are characterized by values of 20.28, 11.73 and 12.23 %, respectively. The statistical analysis reveals that the diffraction efficiency of group No.3 differs from groups No.4, No.5 and No.6, i.e. the zero hypothesis about the equality of mean values is rejected ($p<0.05$). There is no significant difference of RDE between groups No.4, No.5 and No.6.

The specimen group No.7 demonstrates an average RDE of 31.68 %, while groups No.8, No.9 and No.10 are characterized by an average RDE of 21.52, 13.54 and 16.61 %, respectively. The statistical study indicates that the diffraction efficiency of group No.7 contrasts from groups No.8, No.9 and No.10, i.e. the zero hypothesis about the equality of mean values is rejected ($p<0.05$). There is no significant difference of RDE between groups No.8, No.9 and No.10.

Lower mean values of RDE are observed in microstructures which are produced without vibratory excitation and with the assistance of VAP-2. In addition, the application of high-frequency vibratory excitation with ramp waveform increases the RDE, when compared to sine waveform. Fig. 4.5 provides the relation between the amplitude of lateral displacements and the average RDE.

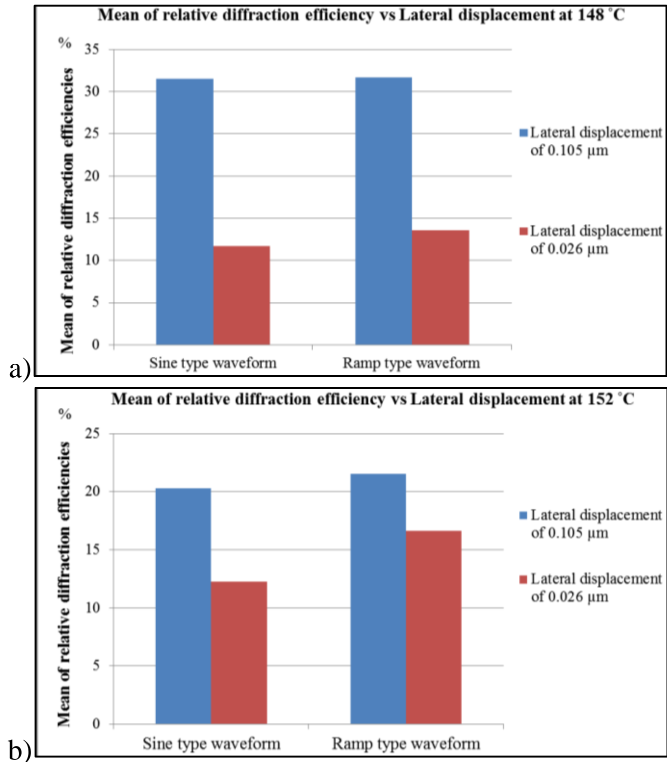

Fig. 4.5. The relation between the lateral displacement and the mean value of RDE when imprinting under the temperature of 148 ˚C (a) and 152 ˚C (b)

Figures 4.5(a) and 4.5(b) demonstrate that an increase in lateral displacements leads to a decrease of the mean RDE. This correlation is less obvious when the process temperature is 152 ˚C. The application of sine waveform decreases the mean RDE by 1.66 times, while the ramp waveform decreases it by 1.29 times. A more pronounced trend is observed under the imprint temperature of 148 ˚C (sine waveform – 2.69 and ramp waveform – 2.33 times).

Lateral displacements induce lateral polymer flow and deformations. The viscosity of the polymer decreases at higher imprint temperature, thus it returns to the initial position. However, at a lower imprint temperature, the polymer is of higher viscosity, therefore plastic lateral residual deformations are greater. On the other hand, maximum values of mean RDE are obtained at a lower imprint temperature and decreased lateral displacements. The obtained correlations demonstrate that a decrease in lateral vibration amplitudes and imprint temperature enhances the mean RDE of the replicated microstructures.

AFM measurements are performed to investigate the topology of the replicated microstructures. Fig. 4.6 demonstrates the profile and 3D images of the sample from the first sample group. The AFM images of other specimen groups are provided in the appendices. The images enable to analyse the profile morphology of the replicated microstructure and compare it with the master microstructure.

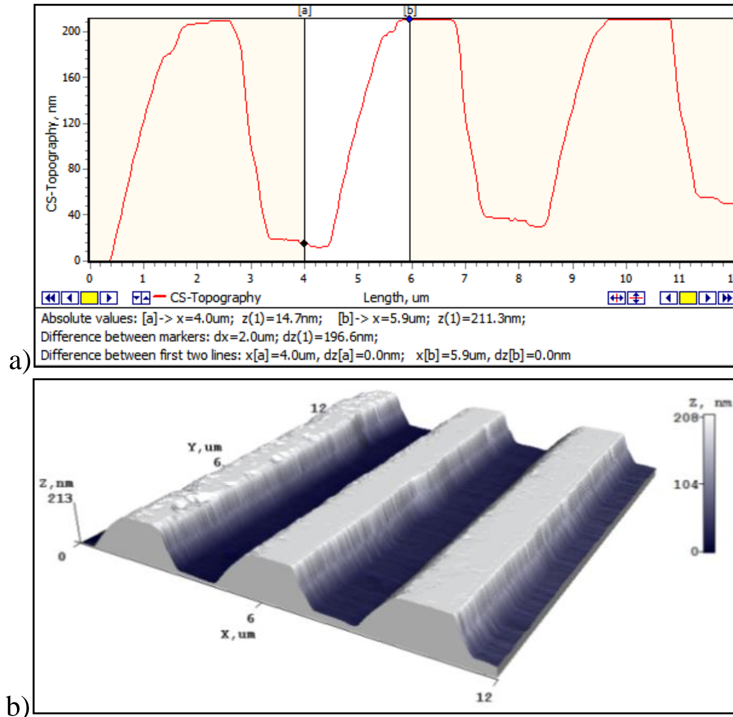

Fig. 4.6. The profile (a) and 3D (b) views of the microstructure replicated without the assistance of high-frequency vibrations, under the temperature of 148 ˚C

The profile view indicates that the difference between the land and the ridge of the replicated microstructure is 196.6 nm. Generalized results which specify the depths of the replicated microstructures are provided in Table 4.4.

Table 4.4. The AFM profile depth measurements with respect to the process regimes

Design of VAP and waveform	Imprint temperature, ˚C	Depth of the imprinted microstructure, nm
Without vibrations	148	196.6
Without vibrations	152	250.7
VAP-1 (sine waveform)	148	464.9
VAP-1 (sine waveform)	152	258.0
VAP-2 (sine waveform)	148	189.5
VAP-2 (sine waveform)	152	152.6
VAP-1 (ramp waveform)	148	470.8
VAP-1 (ramp waveform)	152	279.1
VAP-2 (ramp waveform)	148	188.0
VAP-2 (ramp waveform)	152	283.1

The numerical values demonstrate that microstructures replicated with the application of VAP-1 and ramp waveform vibratory excitation under the imprint temperature of 148 ˚C are characterized by the greatest depth – 470.8 nm. The least successful result is obtained when VAP-2 and ramp waveform vibratory excitation under the imprint temperature of 148 ˚C are applied.

The microstructure imprinted with the assistance of VAP-2 and ramp waveform vibrations is characterized by the third greatest profile depth, namely 283.1 nm. However, this specimen is characterized by the sixth highest mean RDE, that of 16.61 %. This can be explained by the profile length inequality (lateral distortions) between the land and the ridge, caused by high lateral displacements. The relationship between the profile depth and the magnitude of lateral and normal displacements is provided in the Figs. 4.7 and 4.8.

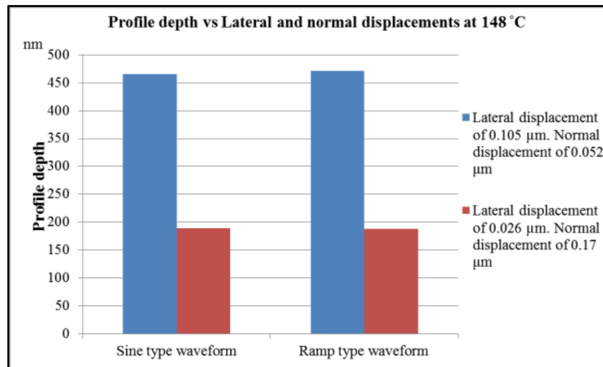

Fig. 4.7. The relation between the lateral and normal displacements and the profile depth when imprinting under the temperature of 148 ˚C

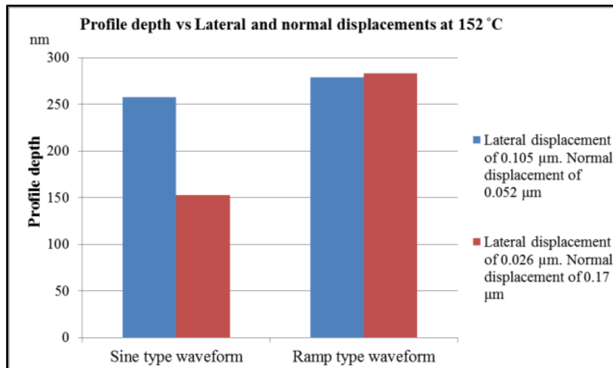

Fig. 4.8. The relation between the lateral and normal displacements and the profile depth when imprinting under the temperature of 152 ˚C

The results of analysis with the AFM demonstrate that high normal amplitudes increase the profile depth, while higher lateral displacements lead to distortions and reduced replicability of the microstructure.

4.3. Conclusions of the chapter

The chapter has discussed the experiments of UHE and thermal imprint assisted by high-frequency vibratory excitation, as well as analysed the quality of the replicated microstructures. The following conclusions are formulated:

- Generating additional heat in the upper second third portion of the stack during the process of UHE increases the mean RDE by 8.6 %.
- The application of ramp waveform high-frequency vibratory excitation and VAP-1 (at the temperature of 148 ˚C) results in the RDE of 31.68 %, while the application of sine waveform under the same process conditions leads to RDE of 31.56 %. Statistically, there is no significant difference between the results with the confidence level of 95 %. In addition, both groups are characterised by low sensitivity to variations of the imprint pressure. Therefore, it is proven that scientific information is important in situations where high imprint pressure is not recommended.
- The increase of lateral displacements decreases the mean RDE from 1.29 to 2.69 times with respect to process parameters.
- The application of ramp waveform and VAP-1 under the imprint temperature of 148 ˚C results in the greatest depth of the replicated microstructure, that of 470.8 nm. This is the closest value to the profile depth of the master microstructure (603.7 nm).

5. GENERAL CONCLUSIONS

1. CGH technology was selected to design a topologically complex master microstructure. The technology of EBL is the most applicable method to rapidly fabricate precise microstructures. In order to replicate microstructures with high-precision and low-cost, high-frequency-assisted thermal imprint and UHE technologies are the most suitable.
2. During the process of EBL, the pixels were divided into portions. This allowed avoiding rounded corners and pixels overlapping, thereby improving the fidelity of the fabricated image. The study of diffraction efficiency demonstrates that the applied measures result in 58 % diffraction efficiency value, what is by 29 % more when compared to the initial trials.
3. Pre-structured pyramids in the second upper third of the stack during the UHE process result in the largest set of appropriate process parameters. This foil orientation reduces temporal and force parameters (0.2 s and 300 N) and produces the highest mean RDE of the embossed periodical microstructure (8.6 %).
   Device designs which vibrate with uniform displacement fields over the operating surface have been developed, numerically simulated, fabricated and experimentally analysed. Pre-stressing the VAP-1 increases the operating frequency by 11.5 % when compared to the unstressed device. The operating frequency of the pre-stressed VAP-2 increases by 15.7 %. VAP-2 vibrates with 2.47 times higher lateral amplitudes (0.03 μm) when compared to VAP-1 (0.01 μm).
4. The application of VAP-1 and ramp waveform vibrations (at the imprint temperature of 148 ˚C) in thermal imprint leads to a mean RDE of 31.68 % and a profile depth of 470.8 nm. The application of VAP-1 and sine waveform (at the temperature of 148 ˚C) results in RDE of 31.56 % and the profile depth of 464.9 nm. In addition, microstructures replicated by applying the aforementioned parameters are characterised by low sensitivity to changes in pressure. This validates the applicability of this technology when high pressure is not recommended.

REFERENCES

1. AN, F., GAO, J., LEI, C., DENG, Z., LI and SHEN. Vibration assisted extrusion of polypropylene. *Chinese Journal of Polymer Science.* 2015, **33**(5): 688-696.
2. BALLANTYNE, J. P.. Mask fabrication by electron-beam lithography, Academic Press**:** 1980, 259-307.
3. BARTOLINI, R., W. HANNAN, D. KARLSONS and M. LURIE. Embossed hologram motion pictures for television playback. *Appl Opt.* 1970, **9**(10): 2283-2290.
4. BINNIG, G., C. F. QUATE and C. GERBER. Atomic Force Microscope. *Physical Review Letters.* 1986, **56**(9): 930-933.
5. BINNIG, G. and H. ROHRER. In touch with atoms. *Reviews of Modern Physics.* 1999, **71**(2): S324-S330.
6. BINNIG, G., H. ROHRER, C. GERBER and E. WEIBEL. Surface Studies by Scanning Tunneling Microscopy. *Physical Review Letters.* 1982, **49**(1): 57-61.
7. BRACEWELL, R. N.. The Fourier Transform and its Applications. McGraw Hill, 1986.
8. BREWER, G. R.. *1 - High resolution lithography. Electron-Beam Technology in Microelectronic Fabrication*, Academic Press**,** 1980, 1-58.
9. BURLAGE, K., C. GERHARDY and W. K. SCHOMBURG (2012). Ultrasonic Hot Embossing and Welding of Micro Structures. Micromechanics and Microactuators: Proceedings of MAMM 2010, Aachen, Germany, May 27-29, 2010. K. G. Ananthasuresh, B. Corves and V. Petuya. Dordrecht, Springer Netherlands**:** 113-123.
10. BURNHAM, N., X. CHEN, C. HODGES, G. MATEI, E. THORESON, C. ROBERTS, M. DAVIES and S. TENDLER. Comparison of calibration methods for atomic-force microscopy cantilevers. *Nanotechnology.* 2002, **14**(1): 1.
11. CASULLI, J., J. R. CLERMONT, A. VON ZIEGLER and B. MENA. The oscillating die: A useful concept in polymer extrusion. *Polymer Engineering & Science.* 1990, **30**(23): 1551-1556.
12. CHANG, T. H. P.. Proximity effect in electron-beam lithography. *Journal of Vacuum Science & Technology.* 1975, **12**(6): 1271-1275.
13. CHIEN-HUNG, L. and C. RONGSHUN. Effects of mold geometries and imprinted polymer resist thickness on ultrasonic nanoimprint lithography. *Journal of Micromechanics and Microengineering.* 2007, **17**(7): 1220.
14. CHOU, S. Y. and P. B. FISCHER. Double 15-nm-wide metal gates 10 nm apart and 70 nm thick on GaAs. *Journal of Vacuum Science & Technology.* 1990, B **8**(6): 1919-1922.
15. CHRISTIAN, H. and M. WALTER. *Einführung in die Kunststoffverarbeitung. Einführung in die Kunststoffverarbeitung*, Carl Hanser Verlag GmbH & Co. KG**:** I-XX., 2015.
16. CLARKE, M. G. Scanning Force Microscope Springs Optimized for Optical—Beam Deflection and with Tips Made by Controlled Fracture. *Journal of Applied Physics.* 1994, **Vol. 76**(No. 1): pp. 172-182.
17. CLEVELAND, J. P., S. MANNE, D. BOCEK and P. K. HANSMA. A nondestructive method for determining the spring constant of cantilevers for scanning force microscopy. *Review of Scientific Instruments.* 1993, **64**(2): 403-405.
18. CUMPSON, P. J., J. HEDLEY, C. A. CLIFFORD, X. CHEN and S. ALLEN. Microelectromechanical system device for calibration of atomic force microscope cantilever spring constants between 0.01 and 4 N/m. *Journal of Vacuum Science & Technology.* 2004, A **22**(4): 1444-1449.

19. E. POPOV, E. Gratings: *Theory and Numeric Applications, Popov, Institut Fresnel.*
20. EUSNER, T., M. HALE and D. E. HARDT. Process Robustness of Hot Embossing Microfluidic Devices. *Journal of Manufacturing Science and Engineering.* 2010, **132**(3): 030920-030920.
21. FARSHCHIAN, B., S. PARK, J. CHOI, A. AMIRSADEGHI, J. LEE and S. PARK. 3D nanomolding for lab-on-a-chip applications. *Lab Chip.* 2012, **12**(22): 4764-4771.
22. FINNE, R. M. and D. L. KLEIN. A Water-Amine-Complexing Agent System for Etching Silicon. *Journal of The Electrochemical Society.* 1967, **114**(9): 965-970.
23. FISCHER, P. B. and S. Y. CHOU. "RIE of sub-50 nm high aspect-ratio pillars, ridges, and trenches in silicon and silicon-germanium." *Microelectronic Engineering*. 1993, **21**(1): 311-314.
24. FRIEDRICH, J. and M. WALTER. *Handbuch Spritzgießen*. Handbuch Spritzgießen, Carl Hanser Verlag GmbH & Co. KG**:** I-5., 2004.
25. GERCHBERG, R. W. A practical algorithm for the determination of phase from image and diffraction plane pictures. *Optik.* 1972, **vol. 35, no. 2**: pp. 237–250.
26. GIUSEPPE A. CIRINO, P. V., RONALDO D. MANSANO, JOSÉ C. PIZOLATO JR., DANIEL B. MAZULQUIM and LUIZ G. NETO. Digital Holography: Computer-Generated Holograms and Diffractive Optics in Scalar Diffraction Domain. *Holography - Different Fields of Application.* 2011, 29-52.
27. GOLDFARB, M. and N. CELANOVIC. Modeling piezoelectric stack actuators for control of micromanipulation. *IEEE Control Systems.* 1997, **17**(3): 69-79.
28. GREN, P.. Four-pulse interferometric recordings of transient events by pulsed TV holography. *Optics and Lasers in Engineering.* 2003, **40**(5–6): 517-528.
29. GUO, L., R. WANG, H. XU and J. LIANG. Why can the carbon nanotube tips increase resolution and quality of image in biological systems? *Physica E: Low-dimensional Systems and Nanostructures.* 2005, **27**(1–2): 240-244.
30. HECKELE, M., W. BACHER and D. K. MÜLLER. Hot embossing - The molding technique for plastic microstructures. *Microsystem Technologies.* 1998, **4**(3): 122-124.
31. HECKELE, M. and W. K. SCHOMBURG. Review on micro molding of thermoplastic polymers. *Journal of Micromechanics and Microengineering.* 2004, **14**(3): R1.
32. HERZIG, H. P.. *Micro-optics: Elements, Systems and Applications*. Taylor & Francis, 1997.
33. HIRAI, Y., S. YOSHIDA and N. TAKAGI. Defect analysis in thermal nanoimprint lithography. *Journal of Vacuum Science & Technology.* 2003, B **21**(6): 2765-2770.
34. HOFFMEISTER, M., LOMAS, C. G., Fundamentals of Hot Wire Anemometry *ZAMM - Journal of Applied Mathematics and Mechanics / Zeitschrift für Angewandte Mathematik und Mechanik*. 1988, **68**(2): 110-110.
35. HOLMGREN, H., LJUNGSTRÖM, A., ALMSTRAND, B. BAKE and A.-C. OLIN. Size distribution of exhaled particles in the range from 0.01 to 2.0 µm. *Journal of Aerosol Science.* 2010, **41**(5): 439-446.
36. YANG, H., L. FAN, A. JIN, Q. LUO, C. GU and Z. CUI. Low-energy Electron-beam Lithography of ZEP-520 Positive Resist. *1st IEEE International Conference on Nano/Micro Engineered and Molecular Systems*. 2006.
37. YAO, D.. *Polymer Micro-Molding/Forming Processes. Micro-Manufacturing*, John Wiley & Sons, Inc., 2011, 197-233.

38. YAO, D., P. NAGARAJAN, L. LI and A. Y. YI. A Strategy for Rapid Thermal Cycling of Molds in Thermoplastic Processing. *Journal of Manufacturing Science and Engineering*. 2006, **128**(4): 837-843.
39. YU, H. W., C. H. LEE, P. G. JUNG, B. S. SHIN, J.-H. KIM, K.-Y. HWANG and J. S. KO. Polymer microreplication using ultrasonic vibration energy. *Journal of Micro/Nanolithography, MEMS, and MOEMS.* 2009, **8**(2): 021113-021113-021117.
40. J. B. LI, K. K. X., X. B. LIN, X. Y. WU, G. L. GAO. Research on the Flow Characteristics of Polymer Injection Molding under Ultrasonic Vibration and Plastics' Mechanical Strength. *Applied Mechanics and Materials.* 2010, **Vols. 37-38**: pp. 1092-1100.
41. JAHNS, J. J. TURUNEN and F. WYROWSKI, Diffractive Optics for Industrial and Commercial Applications. *Laser and Particle Beams.* 1997, **17**(01): 139-141.
42. JUANG, Y.-J., L. J. LEE and K. W. KOELLING. Hot embossing in microfabrication. Part I: Experimental. *Polymer Engineering & Science.* 2002, **42**(3): 539-550.
43. JULIEN, G., C. THIERRY and M. PATRICE. Microinjection molding of thermoplastic polymers: a review. *Journal of Micromechanics and Microengineering.* 2007, **17**(6): R96.
44. KAMP, M., M. EMMERLING, S. KUHN and A. FORCHEL . Nanolithography using a 100 kV electron beam lithography system with a Schottky emitter. *Journal of Vacuum Science & Technology.* 1999, B **17**(1): 86-89.
45. KELLY, A. L., M. WOODHEAD and P. D. COATES. Comparison of injection molding machine performance. *Polymer Engineering & Science.* 2005, **45**(6): 857-865.
46. KHUNTONTONG, P.. *Fabrication of Polymer Micro Devices by Ultrasonic Hot Embossing*. Doctoral thesis. Aachen, Germany, 2008.
47. KHUNTONTONG, P., T. BLASER and W. K. SCHOMBURG. *Ultrasonic micro hot embossing of polymers exemplified by a micro thermal flow sensor. Integration Issues of Miniaturized Systems - MOMS, MOEMS, ICS and Electronic Components (SSI), 2008 2nd European Conference & Exhibition on*.
48. KHUNTONTONG, P., T. BLASER and W. K. SCHOMBURG. Fabrication of Molded Interconnection Devices by Ultrasonic Hot Embossing on Thin Polymer Films. *IEEE Transactions on Electronics Packaging Manufacturing.* 2009, **32**(3): 152-156.
49. KHUNTONTONG P., B. T., MAAS D., SCHOMBURG W. K.. Fabrication of a polymer micro mixer by ultrasonic hot embossing. *19th MicroMechanics Europe Workshop, 28-30 September, Aachen, Germany,* 2008.
50. KYSER, D. F. and N. S. VISWANATHAN. Monte Carlo simulation of spatially distributed beams in electron-beam lithography. *Journal of Vacuum Science & Technology.* 1975, **12**(6): 1305-1308.
51. KOÇ, M. AND S. MAHABUNPHACHAI. *Micro-Forming. Micro-Manufacturing*, John Wiley & Sons, Inc., 2011, 275-299.
52. KOLEW, A., M. HEILIG, K. SIKORA, M. D, and M. WORGULL. *Multi-component hot embossing of micro- and nanosystems*. Design, Test, Integration and Packaging of MEMS/MOEMS (DTIP), 2011 Symposium on.
53. KOLEW, A., D. MÜNCH, K. SIKORA and M. WORGULL. Hot embossing of micro and sub-micro structured inserts for polymer replication. *Microsystem Technologies.* 2010, **17**(4): 609-618.

54. KONG, J., Y. XU, K.-L. YUNG, Y. XIE and L. HE. Enhanced Polymer Melts Flow though Nanoscale Channels under Vibration. *The Journal of Physical Chemistry.* 2009, C **113**(2): 624-629.
55. KOSLOH, J., J. SACKMANN, R. ŠAKALYS, S. LIAO, C. GERHARDY and W. K. SCHOMBURG. Heat generation and distribution in the ultrasonic hot embossing process. *Microsystem Technologies.* 2016, 1-11.
56. KVEDARAVIČIUS, A. A. N., R.. *Silicio integrinių schemų gamybos vadovas* Vilnius: Mokslas, 1989, pp. 159-179.
57. L.K. MUN, D. D., E. LAVALLEE and J. BEAUVAIS. The impact of charging on low-energy electron beam lithography. *Microscopy and Microanalysis.* 2004, **vol. 10**: pp. 804-809, 812.
58. LAGOSKI, T. J., J. R. A. COUTU and L. A. STARMAN. *Retroreflector for photonic Doppler velocimetry,* 2009.
59. LEE, C.-S., C.-G. KANG and S.-W. YOUN. Effect of forming conditions on linear patterning of polymer materials by hot embossing process. *International Journal of Precision Engineering and Manufacturing.* 2010, **11**(1): 119-127.
60. LEE, Y. H., R. BROWNING, N. MALUF, G. OWEN and R. F. W. PEASE. Low voltage alternative for electron beam lithography. *Journal of Vacuum Science & Technology.* 1992, B **10**(6): 3094-3098.
61. LI, Y. and K. SHEN. The Effect of Melt Vibration on Polystyrene Melt Flowing Behavior During Extrusion. *Journal of Macromolecular Science.* 2008, Part B **47**(6): 1228-1235.
62. LI, Y., K. SHEN and J. ZHAN. Improving rheological property of polymer melt via low frequency melt vibration. *Journal of Applied Polymer Science.* 2006, **102**(6): 5292-5296.
63. LIAO, S., C. GERHARDY, J. SACKMANN and W. K. SCHOMBURG. Tools for ultrasonic hot embossing. *Microsystem Technologies.* 2014, **21**(7): 1533-1541.
64. LIEDERT, R., L. K. AMUNDSEN, A. HOKKANEN, M. MAKI, A. AITTAKORPI, M. PAKANEN, J. R. SCHERER, R. A. MATHIES, M. KURKINEN, S. UUSITALO, L. HAKALAHTI, T. K. NEVANEN, H. SIITARI and H. SODERLUND. Disposable roll-to-roll hot embossed electrophoresis chip for detection of antibiotic resistance genemecA in bacteria. *Lab on a Chip.* 2012, **12**(2): 333-339.
65. LIN, C.-H. and R. CHEN. Ultrasonic nanoimprint lithography: a new approach to nanopatterning. *Journal of Micro/Nanolithography, MEMS, and MOEMS.* 2006, **5**(1): 11003-11006.
66. LIN, M.-C., J.-P. YEH, S.-C. CHEN, R.-D. CHIEN and C.-L. HSU. Study on the replication accuracy of polymer hot embossed microchannels. *International Communications in Heat and Mass Transfer.* 2013, **42**: 55-61.
67. LINFA, P., D. YUJUN, Y. PEIYUN and L. XINMIN. Micro hot embossing of thermoplastic polymers: a review. *Journal of Micromechanics and Microengineering.* 2014, **24**(1): 013001.
68. LIU, C., J. M. LI, J. S. LIU and L. D. WANG. Deformation behavior of solid polymer during hot embossing process. *Microelectronic Engineering.* 2010, **87**(2): 200-207.
69. LIU, S.-J. and Y.-T. Dung. Hot embossing precise structure onto plastic plates by ultrasonic vibration. *Polymer Engineering & Science*. 2005, **45**(7): 915-925.
70. LO, C. W., M. J. ROOKS, W. K. LO, M. ISAACSON and H. G. Craighead. Resists and processes for 1 kV electron beam microcolumn lithography. *Journal of Vacuum Science & Technology.* 1995, B **13**(3): 812-820.

71. MADOU, M. J., L. J. LEE, S. DAUNERT, S. LAI and C.-H. SHIH. Design and Fabrication of CD-like Microfluidic Platforms for Diagnostics: Microfluidic Functions. *Biomedical Microdevices.* 2001, **3**(3): 245-254.
72. MEHNE, C., STEGER, R., KOLTAY, P., WARKENTIN, D. and HECKELE, M.. Large area polymer microstructure replications through the hot embossing using modular moulding tools. *Proc. IMechE Part B: Journal Engineering Manufacture.* 2008, pp. 93-99.
73. MEKARU, H., H. GOTO and M. TAKAHASHI. Development of ultrasonic micro hot embossing technology. *Microelectronic Engineering.* 2007, **84**(5–8): 1282-1287.
74. MEKARU, H., O. NAKAMURA, O. MARUYAMA, R. MAEDA and T. HATTORI. Development of precision transfer technology of atmospheric hot embossing by ultrasonic vibration. *Microsystem Technologies.* 2006, **13**(3): 385-391.
75. MEMERING, B.. *Rolle-zu-Rolle Fertigung von Mikrostrukturen durch Ultraschallheißprägen, Doctoral thesis.* Aachen, Germany, 2014.
76. MENA, B., O. MANERO and D. M. BINDING. Proceedings of the IUTAM Symposium on Non-Newtonian Fluid Mechanics Complex flow of viscoelastic fluids through oscillating pipes. Interesting effects and applications. *Journal of Non-Newtonian Fluid Mechanics.* 1979, **5**: 427-448.
77. MENGES, G. M., W.; MOHREN, P.. *Spritzgießwerkzeuge- Anleitung zum Bau von Spritzgießwerkzeugen*. Carl Hanser Verlag, München, Wien, 1999.
78. METWALLY, K., L. ROBERT, S. QUESTE, B. GAUTHIER-MANUEL and C. KHAN-MALEK. Roll manufacturing of flexible microfluidic devices in thin PMMA and COC foils by embossing and lamination. *Microsystem Technologies.* 2011, **18**(2): 199-207.
79. MICHAELI, W., A. SPENNEMANN and R. GÄRTNER. New plastification concepts for micro injection moulding. *Microsystem Technologies.* 2002, **8**(1): 55-57.
80. MOHAMMAD, M. A., M. MUHAMMAD, S. K. DEW and M. STEPANOVA. *Fundamentals of Electron Beam Exposure and Development. Nanofabrication: Techniques and Principles.* Vienna, Springer Vienna**,** 2012, 11-41.
81. NARIJAUSKAITE, B.. *Microrelief formation by mechanical imprint method, Doctoral thesis.* Kaunas, 2013.
82. NARIJAUSKAITE, B., A. PALEVICIUS, P. NARMONTAS, M. RAGULSKIS and G. JANUSAS. High-Frequency Excitation for Thermal Imprint of Microstructures Into a Polymer. *Experimental Techniques.* 2013, **37**(5): 41-47.
83. NATHANSON, H. C., W. E. NEWELL, R. A. WICKSTROM and J. R. DAVIS. The resonant gate transistor. *IEEE Transactions on Electron Devices.* 1967, **14**(3): 117-133.
84. NIE, H.-Y., M. J. WALZAK and N. S. MCINTYRE. Use of biaxially oriented polypropylene film for evaluating and cleaning contaminated atomic force microscopy probe tips: An application to blind tip reconstruction. *Review of Scientific Instruments.* 2002, **73**(11): 3831-3836.
85. NIE, H.-Y., M. J. WALZAK and N. S. McIntyre. Atomic force microscopy study of biaxially oriented polypropylene films. *Journal of Materials Engineering and Performance.* 2004, **13**(4): 451-460.
86. NISHCHAL, N. K., J. JOSEPH and K. SINGH. Fully phase encryption using digital holography. *Optical Engineering.* 2004, **43**(12): 2959-2966.

87. NONHOF, C. J. and G. A. LUITEN. Estimates for process conditions during the ultrasonic welding of thermoplastics. *Polymer Engineering & Science.* 1996, **36**(9): 1177-1183.
88. OBERBACH, K. B., E.; BRINKMANN, S.; SCHMACHTENBERG, E.. *Saechtling Kunststoff Taschenbuch*. Carl Hanser Verlag, München, **29. Ausgabe,** 2004.
89. OIKAWA, M., T. SHIMOBABA, N. MASUDA and T. ITO. Computer-generated hologram using an approximate Fresnel integral. *Journal of Optics.* 2011, **13**(7): 075405.
90. ÖZEL, T. and T. THEPSONTHI. Mechanical Micro-Machining. *Micro-Manufacturing*, John Wiley & Sons, Inc., 2011: 235-274.
91. P. KHUNTONTONG, T. B., W.K. SCHOMBURG. Ultrasonic micro hot embossing of thermoplastic polymers. *Proc. 24th Annual Meeting of the Polymer Processing Society, PPS24, June 15-19, 2008, Salerno, Italy*: page II.364.
92. PAHL, M., W. GLEISSLE, H.-M. LAUN and V. D.-G. *Kunststofftechnik. Praktische Rheologie der Kunststoffe und Elastomere*. Düsseldorf, VDI-Verlag, 1995.
93. PARK, J. M., N. H. KIM, B.-K. LEE, K.-H. LEE and T. H. KWON. Nickel stamp fabrication and hot embossing for mass-production of micro/nano combined structures using anodic aluminum oxide. *Microsystem Technologies.* 2008, **14**(9): 1689-1694.
94. PÉREZ, J. M., J. L. VILAS, J. M. LAZA, S. ARNÁIZ, F. MIJANGOS, E. BILBAO, M. RODRÍGUEZ and L. M. LEÓN. Effect of reprocessing and accelerated ageing on thermal and mechanical polycarbonate properties. *Journal of Materials Processing Technology.* 2010, **210**(5): 727-733.
95. RAPOSO, M., Q. FERREIRA and P. RIBEIRO. A guide for atomic force microscopy analysis of soft-condensed matter. *Modern research and educational topics in microscopy.* 2007, **1**: 758-769.
96. ROOS, N., M. WISSEN, T. GLINSNER and H.-C. SCHEER. *Impact of vacuum environment on the hot embossing process,* 2003.
97. RUPRECHT, R., T. GIETZELT, K. MÜLLER, V. PIOTTER and J. HAUSSELT. Injection molding of microstructured components from plastics, metals and ceramics. *Microsystem Technologies.* 2002, **8**(4): 351-358.
98. SAARI, P., R. KAARLI and M. RÄTSEP. Temporally multiplexed Fourier holography and pattern recognition of femtosecond-duration images. *Journal of Luminescence.* 1993, **56**(1): 175-180.
99. SACKMANN, J., K. BURLAGE, C. GERHARDY, B. MEMERING, S. LIAO and W. K. SCHOMBURG. Review on ultrasonic fabrication of polymer micro devices. *Ultrasonics.* 2015, **56**: 189-200.
100. SCHIFT, H., C. DAVID, M. GABRIEL, J. GOBRECHT, L. J. HEYDERMAN, W. KAISER, S. KÖPPEL and L. SCANDELLA. Nanoreplication in polymers using hot embossing and injection molding. *Microelectronic Engineering.* 2000, **53**(1–4): 171-174.
101. SCHIFT, H., R. W. JASZEWSKI, C. DAVID and J. GOBRECHT. Nanostructuring of polymers and fabrication of interdigitated electrodes by hot embossing lithography. *Microelectronic Engineering.* 1999, **46**(1–4): 121-124.
102. SCHIFT, H. and J. SÖCHTIG. LIGA-Technology for the fabrication of positioned planar structures. *Microsystem Technologies.* 1998, **4**(3): 132-134.
103. SCHOMBURG, W. K., K. BURLAGE and C. GERHARDY. Ultrasonic Hot Embossing. *Micromachines*. 2011, 2(2): 157.

104. SCHWARTZ, G. C. and P. M. SCHAIBLE. Reactive ion etching of silicon. *Journal of Vacuum Science & Technology.* 1979, **16**(2): 410-413.
105. SEO, Y.-S. and K. PARK. Direct patterning of micro-features on a polymer substrate using ultrasonic vibration. *Microsystem Technologies.* 2012, **18**(12): 2053-2061.
106. SINGH, K. and R. B. DUPAIX. Hot-embossing experiments of polymethyl methacrylate across the glass transition temperature with variation in temperature and hold times. *Polymer Engineering & Science.* 2012, **52**(6): 1284-1292.
107. SINHA, M. and D. J. BUCKLEY. *Acoustic Properties of Polymers. Physical Properties of Polymers Handbook*. J. E. Mark. New York, NY, Springer New York**,** 2007, 1021-1031.
108. SOIFER, V. A., V. KOTLAR and L. DOSKOLOVICH. *Iteractive Methods For Diffractive Optical Elements Computation*, Taylor & Francis, 1997.
109. SON, J. Y., B. JAVIDI and K. KAE-DAL. Methods for Displaying Three-Dimensional Images. *Proceedings of the IEEE*. 2006, **94**(3): 502-523.
110. THIENEL, P. S., L.; BOGATZ, V.. p, v, T- Diagramm- Beschreibung von Thermoplasten mit einfachen Funktionen. *Maschinenmarkt.* 1978, **vol. 84**: pp. 1735-1737.
111. THOMSON, M. J. and M. R. TAGHIZADEH. Design and fabrication of Fourier plane diffractive optical elements for high-power fibre-coupling applications. *Optics and Lasers in Engineering.* 2005, **43**(6): 671-681.
112. TOLLKÖTTER, A., J. SACKMANN, T. BALDHOFF, W. K. SCHOMBURG and N. KOCKMANN. Ultrasonic Hot Embossed Polymer Microreactors for Optical Measurement of Chemical Reactions. *Chemical Engineering & Technology.* 2015, **38**(7): 1113-1121.
113. VALIN, J. L., E. GONÇALVES, F. PALACIOS and J. R. PÉREZ. Methodology for analysis of displacement using digital holography. *Optics and Lasers in Engineering.* 2005, **43**(1): 99-111.
114. VELEGOL, S. B. and B. E. LOGAN. Contributions of bacterial surface polymers, electrostatics, and cell elasticity to the shape of AFM force curves. *Langmuir.* 2002,**18**(13): 5256-5262.
115. VELTEN, T., H. SCHUCK, W. HABERER and F. BAUERFELD. Investigations on reel-to-reel hot embossing. *The International Journal of Advanced Manufacturing Technology.* 2009, **47**(1): 73-80.
116. VIG, A. L., T. MÄKELÄ, P. MAJANDER, V. LAMBERTINI, J. AHOPELTO and A. KRISTENSEN. Roll-to-roll fabricated lab-on-a-chip devices. *Journal of Micromechanics and Microengineering.* 2011, **21**(3): 035006.
117. VILALTA-CLEMENTE, A. and A. GLOYSTEIN. *Principles of Atomic Force Microscopy.* Physics if Advanced Materials Winter School, 2008, 1-8.
118. WHITESIDE, B. R., M. T. MARTYN and P. D. COATES. In-process Monitoring of Micromoulding – Assessment of Process Variation. *International Polymer Processing.* 2005, **20**(2): 162-169.
119. WHITESIDE, B. R., M. T. MARTYN, P. D. COATES, P. S. ALLAN, P. R. HORNSBY and G. GREENWAY. Micromoulding: process characteristics and product properties. *Plastics, Rubber and Composites.* 2003, **32**(6): 231-239.
120. WILSON, W. L., K. CURTIS, M. TACKITT, A. HILL, A. HALE, M. SCHILLING, C. BOYD, S. CAMPBELL, L. DHAR and A. HARRIS. High density, high performance optical data storage via volume holography: Viability at last? *Optical and Quantum Electronics.* 2000, **32**(3): 393-404.

121. WYROWSKI, F.. Diffraction efficiency of analog and quantized digital amplitude holograms: analysis and manipulation. *Journal of the Optical Society of America.* 1990, A **7**(3): 383-393.
122. WOLF, B.. *Handbook of Ion Sources*. Florida: Boca Raton. 1995, pp. 209-229.
123. WORGULL, M... *Hot Embossing.* Boston, William Andrew Publishing.2009.
124. WORGULL, M., M. HECKELE and W. K. SCHOMBURG. *Analyse des Mikro-Heißprägeverfahrens*, FZKA, 2003.
125. WORGULL, M., M. HECKELE and W. K. SCHOMBURG. Large-scale hot embossing. *Microsystem Technologies.* 2005, **12**(1): 110-115.
126. WORGULL, M., J.-F. HÉTU, K. K. KABANEMI and M. HECKELE. Hot embossing of microstructures: characterization of friction during demolding. *Microsystem Technologies.* 2008, **14**(6): 767-773.
127. ZACHARIADES, A. E. and B. CHUNG. New polymer processing technologies for engineering the physical and mechanical properties of polymer products. *Advances in Polymer Technology.* 1987, **7**(4): 397-409.
128. ZHAO, J., R. H. MAYES, G. CHEN, P. S. CHAN and Z. J. XIONG. Polymer micromould design and micromoulding process. *Plastics, Rubber and Composites.* 2003, **32**(6): 240-247.
129. ZHAO, J., R. H. MAYES, G. CHEN, H. XIE and P. S. CHAN. Effects of process parameters on the micro molding process. *Polymer Engineering & Science.* 2003, **43**(9): 1542-1554.

LIST OF AUTHOR'S PUBLICATIONS

Publications in journals listed in the ISI Web of Science database with citation index

In internationally recognised publishing houses

1. Šakalys, Rokas; Janušas, Giedrius; Palevičius, Arvydas; Čekas, Elingas; Jūrėnas, Vytautas; Sodah, Amer. Microstructures replication using high frequency excitation // Microsystem technologies. Berlin: Springer. ISSN 0946-7076. 2016, vol. 00, p. [1-13]. [Science Citation Index Expanded (Web of Science); SpringerLINK]. [IF: 0,875; AIF: 3,485; IF/AIF: 0,251; Q3; 2014 Journal Citation Reports® Science Edition (Thomson Reuters, 2016)].
2. Kosloh, J.; Sackmann, J.; Šakalys, Rokas; Liao, S.; Gerhardy, C.; Schomburg, W.K.. Heat generation and distribution in the ultrasonic hot embossing process // Microsystem technologies. Berlin: Springer. ISSN 0946-7076. 2016, vol. 00, p. [1-11]. [Science Citation Index Expanded (Web of Science); SpringerLINK]. [IF: 0,875; AIF: 3,485; IF/AIF: 0,251; Q3; 2014 Journal Citation Reports® Science Edition (Thomson Reuters, 2016)].
3. Palevičius, Arvydas; Janušas, Giedrius; Čekas, Elingas; Šakalys, Rokas. Analysis of the influence of high-frequency excitation into quality of the replicated microstructure // Experimental techniques. Hoboken, NJ: Wiley-Blackwell. ISSN 0732-8818. 2015, vol. 39, iss. 00, p. [1-12]. [Science Citation Index Expanded (Web of Science)]. [IF: 0,545; AIF: 1,482; IF/AIF: 0,368; Q3; 2014 Journal Citation Reports® Science Edition (Thomson Reuters, 2016)].
4. Narijauskaitė, Birutė; Palevičius, Arvydas; Gaidys, Rimvydas; Janušas, Giedrius; Šakalys, Rokas. Polycarbonate as an elasto-plastic material model for simulation of the microstructure hot imprint process // Sensors. Basel: MDPI AG. ISSN 1424-8220. 2013, vol. 13 issue 9, p. 11229-11242. [Science Citation Index Expanded (Web of Science); Academic Search Complete]. [IF: 2,048; AIF: 2,677; IF/AIF: 0,765; Q1; 2013 Journal Citation Reports® Science Edition (Thomson Reuters, 2016)].

In international publishing houses

1. Palevičius, Arvydas; Ponelytė, Sigita; Guobienė, Asta; Prosyčevas, Igoris; Puišo, Judita; Šakalys, Rokas. Design and fabrication of piezoelectric nanocomposite structures for microdevice applications // Journal of micro/nanolithography, MEMS, and MOEMS. Bellingham: SPIE. ISSN 1932-5150. 2013, vol. 12, iss. 4, art. no. 043004, p. [1-5]. [Science Citation Index Expanded (Web of Science); Compendex]. [IF: 1,205; AIF: 3,128; IF/AIF: 0,385; Q3; 2013 Journal Citation Reports® Science Edition (Thomson Reuters, 2016)].

In national publishing houses

1. Šakalys, Rokas; Janušas, Giedrius; Palevičius, Arvydas; Bendikienė, Regita; Palevičius, Ramutis. Microstructure replication using high frequency vibroactive pad // Mechanika / Kauno technologijos universitetas, Lietuvos mokslų akademija, Vilniaus Gedimino technikos universitetas. Kaunas: KTU. ISSN 1392-1207. 2015, Vol. 21, no. 2, p. 134-140. [Science Citation Index Expanded (Web of Science); INSPEC; Compendex; Academic Search Complete; FLUIDEX; Scopus]. [IF: 0,292; AIF: 1,862; IF/AIF: 0,157; Q4; 2014 Journal Citation Reports® Science Edition (Thomson Reuters, 2016)].
2. Narijauskaitė, Birutė; Palevičius, Arvydas; Janušas, Giedrius; Šakalys, Rokas. Numerical investigation of dynamical properties of vibroactive pad during hot imprint process // Journal of vibroengineering / Vibromechanika, Lithuanian Academy of Sciences, Kaunas University of Technology, Vilnius Gediminas Technical University. Kaunas: Vibroengineering. ISSN 1392-8716. 2013, vol. 15, no. 4, p. 1983-1990. [Science Citation Index Expanded (Web of Science); INSPEC; Academic Search Complete; Central & Eastern European Academic Source (CEEAS); Computers & Applied Sciences Complete; Current Abstracts; TOC Premier]. [IF: 0,660; AIF: 2,255; IF/AIF: 0,293; Q3; 2013 Journal Citation Reports® Science Edition (Thomson Reuters, 2016)].

Publications in journals listed in the ISI Web of Science database without citation index

In internationally recognised publishing houses

1. Palevičius, Arvydas; Šakalys, Rokas; Janušas, Giedrius; Narmontas, Pranas. Investigation of dependency of microstructure quality on vibration mode // Nanotechnology in the security systems: NATO advanced research workshop on nanotechnology in the security systems, Yalta, Ukraine, September 29 - October 03, 2013 / Edited by J. Bonča, J. Kruchinin. Dordrecht: Springer Science+Business Media, 2015. (NATO Science for Peace and Security Series C: Environmental Security, ISSN 1874-6519), ISBN 9789401790048. p. 49-54. [Conference Proceedings Citation Index; SpringerLINK].

In international publishing houses

1. Palevičius, Arvydas; Janušas, Giedrius; Čekas, Elingas; Šakalys, Rokas; Palevičiūtė, Ieva; Ramoška, Evaldas. Microstructures replication using high frequency excitation // Proceedings of SPIE: Smart sensors, actuators and MEMS VII and Cyber Physical systems, Barcelona, Spain, May 4, 2015 [elektroninis išteklius] / Edited by José Luis Sánchez-Rojas; Riccardo Brama. Bellingham, WA: SPIE. ISSN 0277-786X. 2015, vol. 9517, Article 951722, p. [1-9]. [Conference Proceedings Citation Index- Science].
2. Janušas, Giedrius; Guobienė, Asta; Prosyčevas, Igoris; Palevičius, Arvydas; Ponelytė, Sigita; Baltrušaitis, Valentinas; Šakalys, Rokas. Novel composite piezoelectric material for energy harvesting applications // Proceedings of SPIE:

Electroactive polymer actuators and devices (EAPAD) 2015, San Diego, California, US, March 08, 2015 [elektroninis išteklius]. Bellingham: SPIE. ISSN 0277-786X. 2015, vol. 9430, Article 943030, p. 1-6. [Conference Proceedings Citation Index- Science].

Publications in other international database journals (In periodic and non-periodic journals and conference proceedings)

In national publishing houses

1. Janušas, Giedrius; Čekas, Elingas; Šakalys, Rokas; Palevičiūtė, Ieva; Ramoška, Evaldas. Experimental and modelling means for analysis and replication periodical microstructures // Journal of measurements in engineering / Lithuanian Academy of Sciences, Kaunas University of Technology, Vilnius Gediminas Technical University. Kaunas: Vibroengineering. ISSN 2335-2124. 2015, vol. 3, iss. 1, p. 23-34. [Inspec; Academic OneFile].
2. Šakalys, Rokas; Janušas, Giedrius; Palevičius, Arvydas; Čekas, Elingas. Optical evaluation of periodical microstructure, replicated using ultrasonic hot imprint, according to process regimes // Vibroengineering procedia: international conference Vibroengineering - 2014, Katowice, Poland, 13-15 October, 2014. Kaunas: JVE International. ISSN 2345-0533. 2014, vol. 3, p. 204-208. [Compendex; Academic OneFile].
3. Šakalys, Rokas; Palevičius, Arvydas; Janušas, Giedrius. Vibroactive pad improvement using stack type piezoactuator // Vibroengineering procedia : international conference Vibroengineering - 2013, Druskininkai, Lithuania, 17-19 September 2013. Kaunas: Vibroengineering. ISSN 2345-0533. 2013, vol. 2, p. 109-112. [Compendex; Scopus].

Publications in other peer-reviewed scientific journals

Publications in conference proceedings

In internationally recognised publishing houses

1. Šakalys, Rokas; Janušas, Giedrius; Palevičius, Arvydas. Quality analysis of periodical microstructures, created by using high frequency vibration excitation // International electronic conference on sensors and applications, 1-16 June, 2014. Basel: MDPI AG, 2014. p. 1-6.

In national publishing houses

1. Šakalys, Rokas; Janušas, Giedrius; Palevičius, Arvydas. Vibroactive pad for replication of microstructure and its experimental analysis // Mechanika 2014: proceedings of the 19th international conference, 24, 25 April 2014, Kaunas University of Technology, Lithuania / Kaunas University of Technology, Lithuanian Academy of Science, IFTOMM National Committee of Lithuania, Baltic Association of Mechanical Engineering. Kaunas: Technologija. ISSN 1822-2951. 2014, p. 225-227.

2. Narijauskaitė, Birutė; Palevičius, Arvydas; Janušas, Giedrius; Šakalys, Rokas. Numerical investigation of dynamical properties of vibroactive pad // Vibroengineering procedia: international conference Vibroengineering- 2013, Druskininkai, Lithuania, 17-19 September, 2013. Kaunas: Vibroengineering. ISSN 2345-0533. 2013, vol. 1, p. 15-18.

UDK 678.02+534.232+004.932](043.3)

SL344. 2017-03-20 12 leidyb. apsk. l. Tiražas 10 egz.
Išleido Kauno technologijos universitetas, K. Donelaičio g. 73, 44249 Kaunas
Spausdino leidyklos „Technologija“ spaustuvė, Studentų g. 54, 51424 Kaunas

APPENDIXES

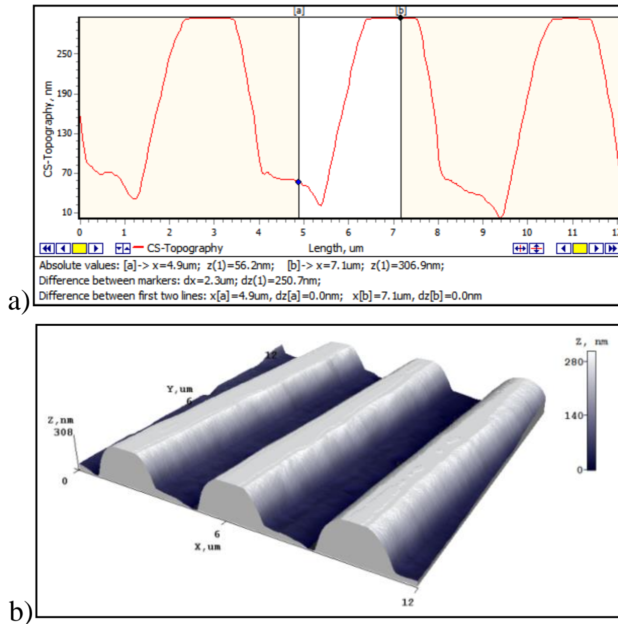

The profile (a) and 3D (b) views of the microstructure replicated without the assistance of high-frequency vibrations, under the temperature of 152 ˚C

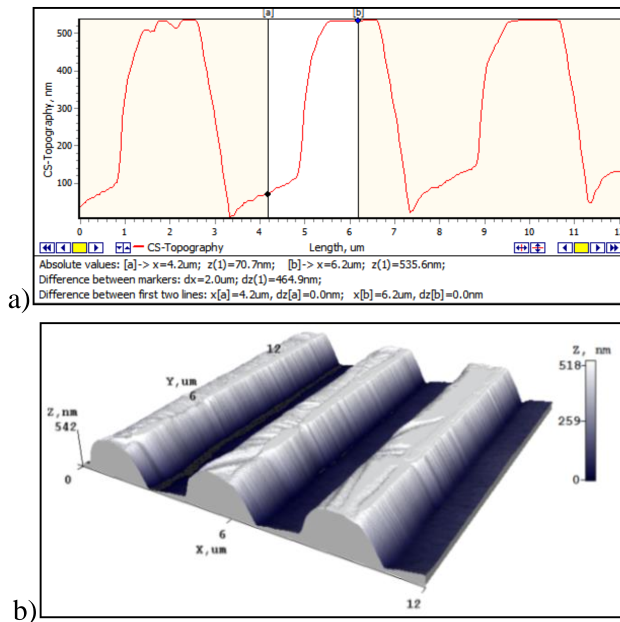

The profile (a) and 3D (b) views of the microstructure replicated by using VAP-1 with sine waveform excitation, under the temperature of 148 ˚C

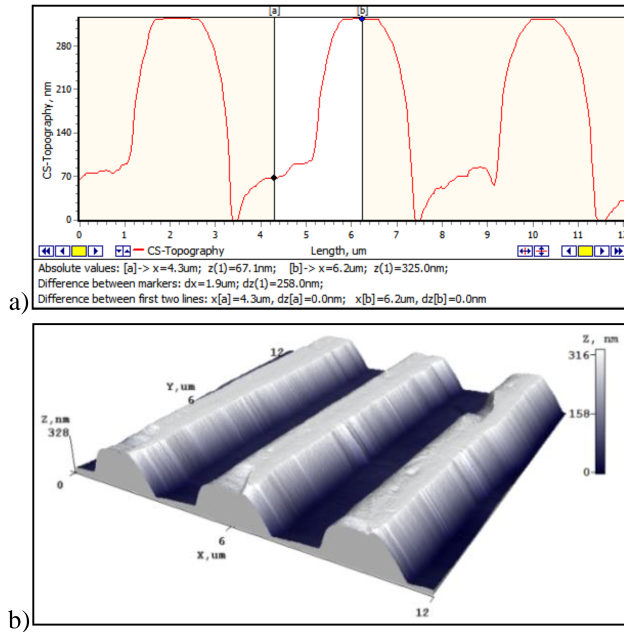

The profile (a) and 3D (b) views of the microstructure replicated by using VAP-1 with sine waveform excitation, under the temperature of 152 ˚C

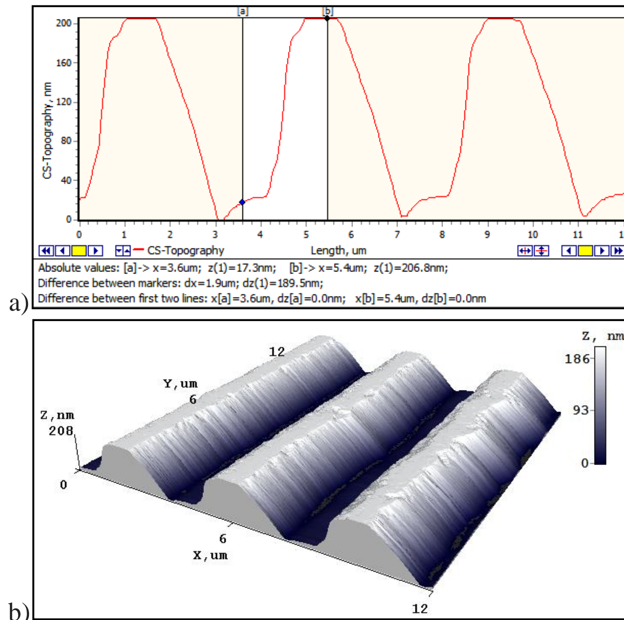

The profile (a) and 3D (b) views of the microstructure replicated by using VAP-2 with sine waveform excitation, under the temperature of 148 ˚C

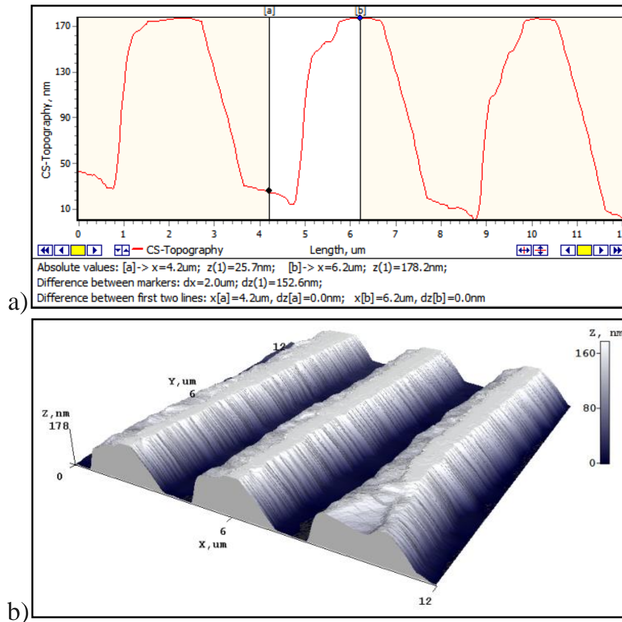

The profile (a) and 3D (b) views of the microstructure replicated by using VAP-2 with sine waveform excitation, under the temperature of 152 ˚C

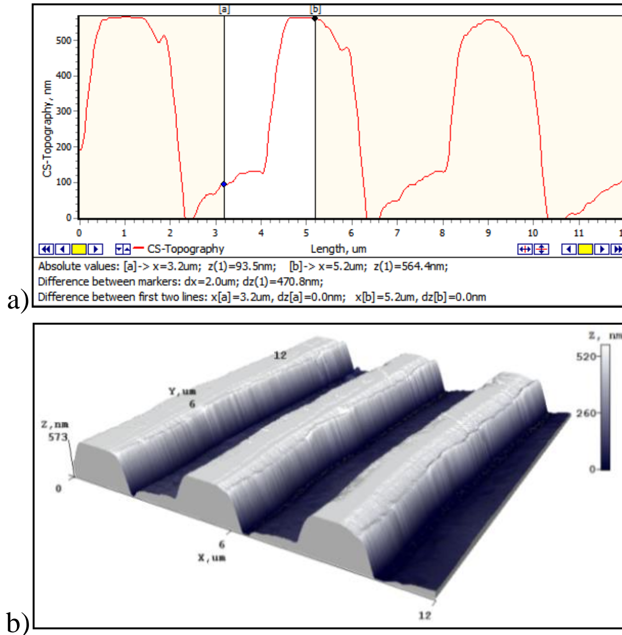

The profile (a) and 3D (b) views of the microstructure replicated by using VAP-1 with ramp waveform excitation, under the temperature of 148 ˚C

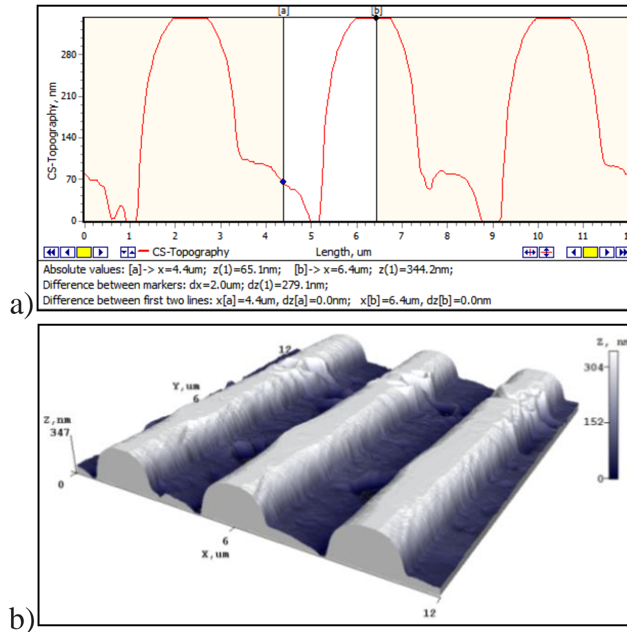

The profile (a) and 3D (b) views of the microstructure replicated by using VAP-1 with ramp waveform excitation, under the temperature of 152 ˚C

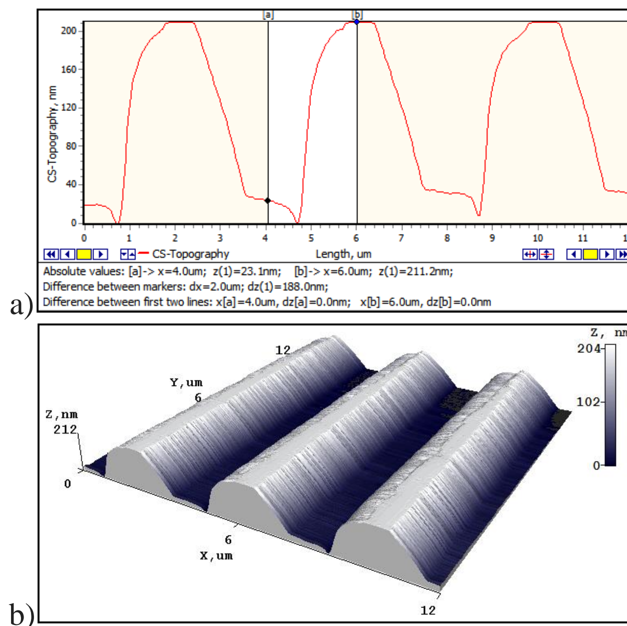

The profile (a) and 3D (b) views of the microstructure replicated by using VAP-2 with ramp waveform excitation, under the temperature of 148 ˚C

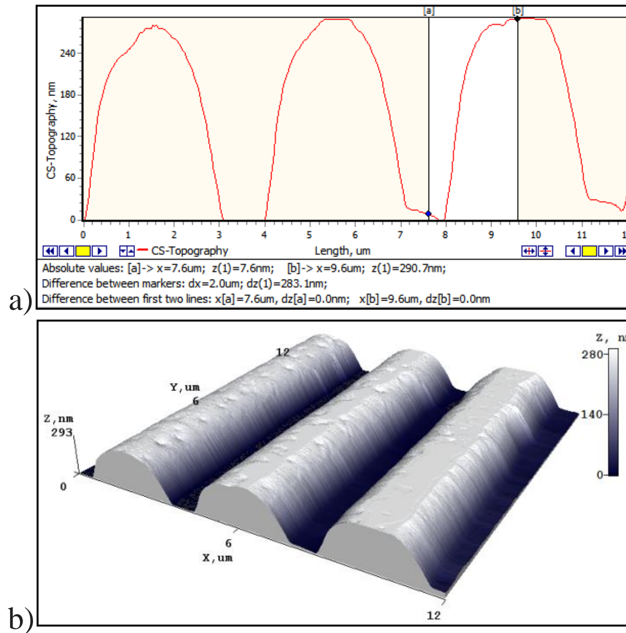

The profile (a) and 3D (b) views of the microstructure replicated by using VAP-2 with ramp waveform excitation, under the temperature of 152 ˚C